



Università degli Studi di Ferrara

DOTTORATO DI RICERCA IN
FISICA

CICLO XXVI

COORDINATORE Prof. Vincenzo Guidi

**High Level Trigger software
performance profiling and χ_b
production study at the LHCb
experiment**

Settore Scientifico Disciplinare FIS/01

Dottorando

Dott. Alexander Mazurov

Tutore

Prof. Concezio Bozzi

Anni 2011/2013

Abstract

Trigger is a crucial item in experiments at hadron colliders. In this thesis, a software profiling tool has been developed, which helps to analyze and improve the performance of the High Level Trigger software of the LHCb experiment. This tool is able to identify spots where the execution time of the trigger application is slow, thereby allowing the optimization of the trigger decision speed and minimizing dead times during data taking.

The highly efficient LHCb trigger allows precision studies of decays of heavy flavoured particles in final states with muons. In this thesis, a study of χ_b production at LHCb is performed on a proton-proton collisions data set, corresponding to 3 fb^{-1} integrated luminosity, collected at center-of-mass energies of $\sqrt{s} = 7$ and 8 TeV . Radiative χ_b transitions to $\Upsilon(1S)$, $\Upsilon(2S)$ and $\Upsilon(3S)$ are reconstructed, where the Υ decays in two muons. The fraction of Υ originating from χ_b decays are measured as a function of Υ transverse momentum in the LHCb rapidity range $2.0 < y^\Upsilon < 4.5$. The analyzed transverse momentum ranges for decays to $\Upsilon(1S)$, $\Upsilon(2S)$ and $\Upsilon(3S)$ are $6 < p_T^{\Upsilon(1S)} < 40 \text{ GeV}$, $18 < p_T^{\Upsilon(2S)} < 40 \text{ GeV}$ and $27 < p_T^{\Upsilon(3S)} < 40 \text{ GeV}$, respectively. The measurement of $\Upsilon(3S)$ fractions in radiative $\chi_b(3P)$ decay is performed for the first time. The obtained $\Upsilon(3S)$ fractions are $42 \pm 12 \text{ (stat)} \text{ }^{+8.9}_{-11.6} \text{ (syst)} \text{ }^{+2.7}_{-3.1} \text{ (syst.pol)}\%$ and $41 \pm 8 \text{ (stat)} \text{ }^{+1.3}_{-8.6} \text{ (syst)} \text{ }^{+2.6}_{-3.1} \text{ (syst.pol)}\%$ for $\sqrt{s} = 7$ and 8 TeV , respectively. The measured $\chi_{b1}(3P)$ mass is $10,508 \pm 2 \text{ (stat)} \pm 8 \text{ (syst)} \text{ MeV}/c^2$.

Contents

1	Introduction	1
2	Production of Quarkonia at the LHC	4
2.1	The quarkonium mass spectrum	7
2.2	Quarkonium production	9
2.2.1	Colour Singlet Model	9
2.2.2	Colour Octet Model	10
2.3	Production of χ_b mesons at LHC	11
3	The LHCb experiment	15
3.1	The LHC	15
3.2	The LHCb experiment	17
3.3	Tracking system	19
3.3.1	Vertex Locator	19
3.3.2	Magnet	22
3.3.3	Inner tracker	22
3.3.4	Outer tracker	24
3.3.5	Tracker Turicensis	25
3.4	Particle identification	26
3.4.1	RICH system	26
3.4.2	Muon system	28
3.4.3	Calorimeter system	28
3.5	Trigger	31
3.6	LHCb 2010–2012 operation	32
4	LHCb software performance profiling	34
4.1	Introduction	34
4.2	VTune Amplifier	36

4.2.1	Overview	36
4.2.2	Sampling interval	37
4.2.3	Tools	37
4.2.4	Profiling reports	38
4.2.5	Detecting code dependency	40
4.3	Profiling Auditor	41
4.3.1	Gaudi	41
4.3.2	Profiling Auditor	43
4.4	HLT Profiling Examples	47
4.4.1	Memory Allocation Functions	47
4.4.2	Measuring Profiling Accuracy	48
4.4.3	Custom reports	50
4.5	Results	50
5	Study of χ_b production	52
5.1	Introduction	52
5.2	Datasets	53
5.3	Υ signal extraction	54
5.3.1	Selection	54
5.3.2	Fit model	56
5.3.3	Fit results	57
5.4	χ_b signal extraction	61
5.4.1	Selection	62
5.4.2	Fit model	63
5.4.3	χ_b yields in $\chi_b \rightarrow \Upsilon(1S)\gamma$ decays	65
5.4.4	χ_b yields in $\chi_b \rightarrow \Upsilon(2S)\gamma$ decays	70
5.4.5	χ_b yields in $\chi_b \rightarrow \Upsilon(3S)\gamma$ decays	74
5.5	χ_{b1} and χ_{b2} yields ratio	77
5.6	Simulation	78

5.6.1	Data - simulation comparison	78
5.6.2	Selection efficiencies	81
5.7	Υ fractions	83
5.8	Systematic	86
5.8.1	Uncertainties related to the fit model	86
5.8.2	Photon reconstruction efficiency	95
5.8.3	χ_b polarization	96
5.8.4	Summary of systematic uncertainties on the Υ production fractions	101
5.9	Results	102
6	Conclusion	107
	Appendices	109
A	Data fits for $\Upsilon \rightarrow \mu^+\mu^-$ decays	110
B	Data fits for $\chi_b \rightarrow \Upsilon(1S)\gamma$ decays	114
C	Data fits for $\chi_b \rightarrow \Upsilon(2S)\gamma$ decays	118
D	Data fits for $\chi_b \rightarrow \Upsilon(3S)\gamma$ decays	120
E	Simulation	122
	Bibliography	131
	Acknowledgements	136

Chapter 1

Introduction

In 1977 a new family of heavy particles was discovered experimentally by the Fermilab E288 experiment headed by Leon Lederman [1]. These particles, named Υ mesons, consist of a pair of b - and \bar{b} quarks in a bound state. Their discovery was the first evidence of a type of quarks, predicted in 1973 by Makoto Kobayashi and Toshihide Maskawa when they tried to explain CP violation in the Standard Model [2]. Later the evidence of b -quarks was confirmed by observation of B-mesons at ARGUS [3] and CLEO [4] experiments. In the past, particles containing the b quark were largely studied at LEP, Tevatron and, more recently, in the B factories (BaBar, Belle). Nowadays, the LHCb experiment dominates this field by performing precise measurements of B hadrons spectroscopy, decays and CP violation.

Bottomonium states are $b\bar{b}$ bound states. They are usually included in the *heavy quarkonia* family together with *charmonium* $c\bar{c}$ bound states, such as *e.g.* the J/ψ particle. Being composed of a quark and an anti-quark, these states are mesons. The study of quarkonia is very important because it provides a unique way to understand and test the Quantum ChromoDynamics (QCD) theory. Meson properties, such as their masses, can be computed non-pertubatively using lengthy Lattice QCD (LQCD) techniques, which solve the exact QCD equations by using numerical methods. However, the masses of quarkonia are large with respect to the typical hadronic energy scale. Therefore, the speed of heavy quarks inside their own quarkonia is non-relativistic and computations can be

performed by using effective techniques, such as the Non-Relativistic QCD (NRQCD, [5, 6]). Besides assuming that heavy quarks in quarkonia are non-relativistic, these effective models suppose that they move in a static potential [7–9]. In this sense, quarkonia in QCD are analogous to the hydrogen atom or the positronium in QED.

The production mechanism of bottomonium states is not yet well understood. Several models exist, such as the Colour Singlet Model (CSM, NLO CSM), non-relativistic QCD expansion (NRQCD) with contributions from Colour Singlet and Colour Octet, and Colour Evaporation Model (CEM). None of these models succeeded in explaining all experimental results on cross-section and polarization measurements. More experimental inputs will be useful in resolving the theoretical models.

In this thesis a study of χ_b production is performed on data from proton-proton collisions, collected by the LHCb experiment at the LHC at centre-of-mass energies $\sqrt{s} = 7$ and 8 TeV. The analyzed data set corresponds to a total integrated luminosity of 3 fb^{-1} . The χ_b mesons were reconstructed by using $\chi_b(nP) \rightarrow \Upsilon(mS)\gamma$ decays. Single differential production cross sections, relative to the production cross-sections of Υ mesons, are measured as function of Υ transverse momentum. A measurement of the $\chi_b(3P)$ mass, which was recently observed by the ATLAS [10], D0 [11] and LHCb [12] collaborations, is also performed.

The analysis performed in this thesis extends the previous LHCb study [13], which reported a measurement of the χ_b production cross-section, and subsequent decay into $\Upsilon(1S)\gamma$, relative to the $\Upsilon(1S)$ production. That measurement was performed on 32 pb^{-1} data set, collected at a centre-of-mass energies $\sqrt{s} = 7$ TeV in 2010, in a region defined by transverse momentum $6 < p_T^{\Upsilon(1S)} < 15 \text{ GeV}/c$ and rapidity $2.0 < y^{\Upsilon(1S)} < 4.5$.

This analysis improves significantly the statistical precision of the previous work and adds more decays and transverse momentum regions. The LHCb detector design allows to perform measurements in Υ rapidity and transverse momentum regions, which are complementary to the ones exploited by other LHC experiments.

Muon triggering and offline muon identification are fundamental for this analysis, and for the physics program of LHCb, with the software High Level Trigger (HLT) being a

crucial player. In this thesis the author presents the tool, which helps to analyze and improve the performance of HLT software. A few spots poorly performing in the HLT code were identified and fixed by using this tool.

The performance tool was reported at the 19th International Conference on Computing in High Energy and Nuclear Physics (New-York, 2012) and the corresponding proceeding was published [14]. The results on χ_b production were regularly presented at the LHCb bottomonium working group, an internal document was prepared by the author, is currently under review and will form the basis of a future LHCb publication.

This thesis is organized as follows. Chapter 2 briefly reviews the quarkonium production mechanisms. Chapter 3 outlines the LHCb experiment design. In Chapter 4 the software performance tool is presented, and Chapter 5 shows the χ_b analysis procedure and results of cross-section and $\chi_b(3P)$ mass measurements. The thesis results are summarized in the Conclusion.

Chapter 2

Production of Quarkonia at the LHC

The Standard Model (SM) is the theory which describes the electromagnetic, weak and strong interactions between elementary particles. The model describes a wide variety of subatomic phenomena involving known elementary particles and has been confirmed with high precision measurements. Quantum Chromodynamics (QCD), the part of the SM describing strong interactions, originated from the quark model started of the 1960s [15,16], few years before the experimental confirmation of the existence of quarks. Quarks are the only elementary particles which are subject to the strong interaction. Because of a phenomenon called color confinement, they are never been directly observed, but can be found within composite particles called hadrons. There are two types of hadrons named as baryons (qqq), made of three quarks or anti-quarks, and mesons ($q\bar{q}$), made of a quark anti-quark pair. There are 6 types of quarks, each with a different *flavour*: up (u), down (d), strange (s), charm (c), bottom or beauty (b), top or truth (t).

Quarkonia, i.e. bound states of heavy quark-antiquark pairs, are particularly interesting in this context, since they provide a testing ground of QCD in a relatively simple and calculable environment. Also, production of quarkonia at LHC represents an interesting check of production mechanisms and models. Toponia ($t\bar{t}$) states are expected to decay very quickly, due to the heavy top quark mass, and have never been observed. The experimentally established quarkonia consist therefore of charmonium ($c\bar{c}$) and bottomonium ($b\bar{b}$) states.

The J/ψ meson, made up of $c\bar{c}$, was the first observed quarkonium state [17], with a mass around 3.1 GeV and narrow width. The analogous bound state in the b sector was established with the observation of the $\Upsilon(1S)$ meson in 1977 [1]. There is a wide variety of quarkonium states, each differing from other by quantum numbers: the principal quantum number (n), the relative angular momentum between the quarks (L), the spin combination of the two quarks (S) and the total angular momentum (J) with $J = L + S$. In particle physics, the notation J^{PC} is often used, where P and C are parity and charge conjugation values, respectively. For the quarkonium states, they are defined as $P = (-1)^{L+1}$ and $C = (-1)^{L+S}$. Table 2.1 shows the properties of some quarkonium states.

Table 2.1: Properties of quarkonium states relevant in this thesis.

Meson	$n^{2S+1}L_J$	J^{PC}	Mass (MeV)
$\eta_c(1S)$	1^1S_0	0^{-+}	2980.4 ± 1.2
$J/\psi(1S)$	1^3S_1	1^{--}	3096.916 ± 0.011
$\chi_{c0}(1P)$	1^3P_0	0^{++}	3414.75 ± 0.31
$\chi_{c1}(1P)$	1^3P_1	1^{++}	3510.66 ± 0.07
$h_c(1P)$	1^3P_1	1^{++}	3525.93 ± 0.27
$\chi_{c2}(1P)$	1^3P_2	2^{++}	3556.20 ± 0.09
$\eta_c(2S)$	2^1S_0	0^{-+}	3637 ± 4
$\psi(2S)$	2^3S_1	1^{--}	3686.09 ± 0.04
η_b	1^1S_0	0^{-+}	$9388.9 \pm 2.5 \pm 2.7$
$\Upsilon(1S)$	1^3S_1	1^{--}	9460.30 ± 0.26
$\chi_{b0}(1P)$	1^3P_0	0^{++}	$9859.44 \pm 0.42 \pm 0.31$
$\chi_{b1}(1P)$	1^3P_1	1^{++}	$9892.78 \pm 0.26 \pm 0.31$
$\chi_{b2}(1P)$	1^3P_2	2^{++}	$9912.21 \pm 0.26 \pm 0.31$
$\Upsilon(2S)$	2^3S_1	1^{--}	10023.26 ± 0.31
$\chi_{b0}(2P)$	2^3P_0	0^{++}	$10232.5 \pm 0.4 \pm 0.5$
$\chi_{b1}(2P)$	2^3P_1	1^{++}	$10255.46 \pm 0.22 \pm 0.5$
$\chi_{b2}(2P)$	2^3P_2	2^{++}	$10268.65 \pm 0.22 \pm 0.5$
$\Upsilon(3S)$	2^3S_1	1^{--}	10355.2 ± 0.5

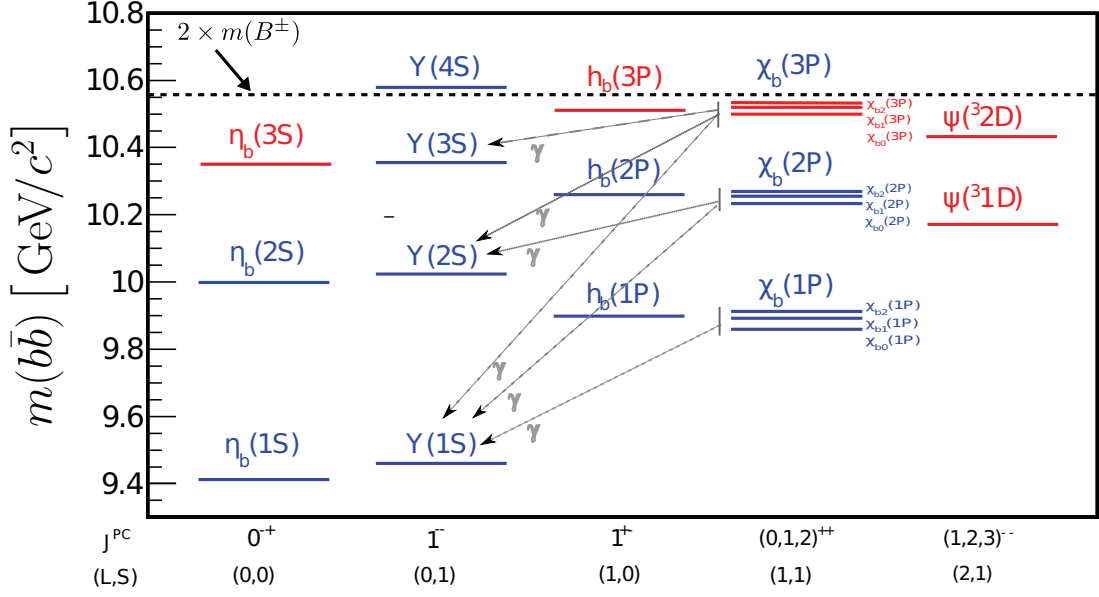


Figure 2.1: Observed (blue) and theoretically predicted (red) bottomonium states

Bottomonium states and their quantum numbers are shown in Figure 2.1. The $L = 0$ and $L = 1$ states are respectively called S-wave and P-wave. For example, the $Y(1S)$ and the $\chi_{b1}(1P)$ are S-wave and P-wave mesons, respectively. The principal quantum number n orders states from lowest to highest masses, such as for $Y(nS)$, where n equals to 1, 2, 3 and 4. When the conditions $L = 1$ and $S = 1$ are satisfied, J takes the value 0, 1 or 2, with the spin-orbit coupling causing mass level splitting. Thus, each χ_b states has three sub-states indexed by the value of the quantum number J . For example, the $\chi_b(1P)$ state has three sub-states $\chi_{bJ}(1P)$, where J is equal to 0, 1 and 2.

Radiative transitions from one bottomonium state to another with the emission of a photon have been observed, with selection rules being the same as for the hydrogen atom energy states. The electric dipole is the leading order transition, which changes the relative angular momentum $\Delta L = \pm 1$ but not the spin $\Delta S = 0$. The magnetic dipole transition is next-to-leading order and is therefore suppressed. This transition changes the spin $\Delta S = \pm 1$ but not the relative angular momentum $\Delta L = 0$. For this reason, the radiative decays exploited in this thesis involve the leading order transitions $\chi_b \rightarrow Y\gamma$.

2.1 The quarkonium mass spectrum

Many theoretical models have been developed to describe quarkonium systems. These models can be roughly split in two classes, based respectively on Lattice QCD calculations and phenomenological approaches. The simplest and most frequently used phenomenological approach is the *non-relativistic potential model*, an effective theory in which the quark move non-relativistically inside hadrons. Similarly to the positronium case, the system is characterized by a typical velocity v given by the strong coupling constant α_s , evaluated at a scale corresponding to the typical size of the bound state

$$v \sim \alpha_s(1/r^2), r \sim 1/mv \quad (2.1)$$

Being v larger than $\alpha_s(m^2)$, higher-order corrections to the non-relativistic approximation are potentially more important than higher-order perturbative corrections. So far the theoretical calculations of charmonium and bottomonium and their spectra measured by many experiments suggest that the potential of quarkonium possesses a radial dependence of an approximately Coulomb form at small distances due to gluon exchange

$$V(r) \sim -\frac{4}{3} \frac{\alpha_s(1/r^2)}{r} \quad (r \rightarrow 0) \quad (2.2)$$

and is confining at large distances due to the increasing strength of the coupling

$$V(r) \sim kr \quad (r \rightarrow \infty) \quad (2.3)$$

where k is the string tension and the factor of $4/3$ arises from the $SU(3)$ colour factors. Several models have been widely used for explaining the quarkonium spectroscopy. Although these potentials have different asymptotic behaviours at small and large distances, they coincide with each other in the region $0.1fm < r < 1fm$, where r is the average distance between heavy quarks in the bound systems. Experimental measurements can be used as inputs to understand the exact shape of the strong potential. For instance, the Cornell model

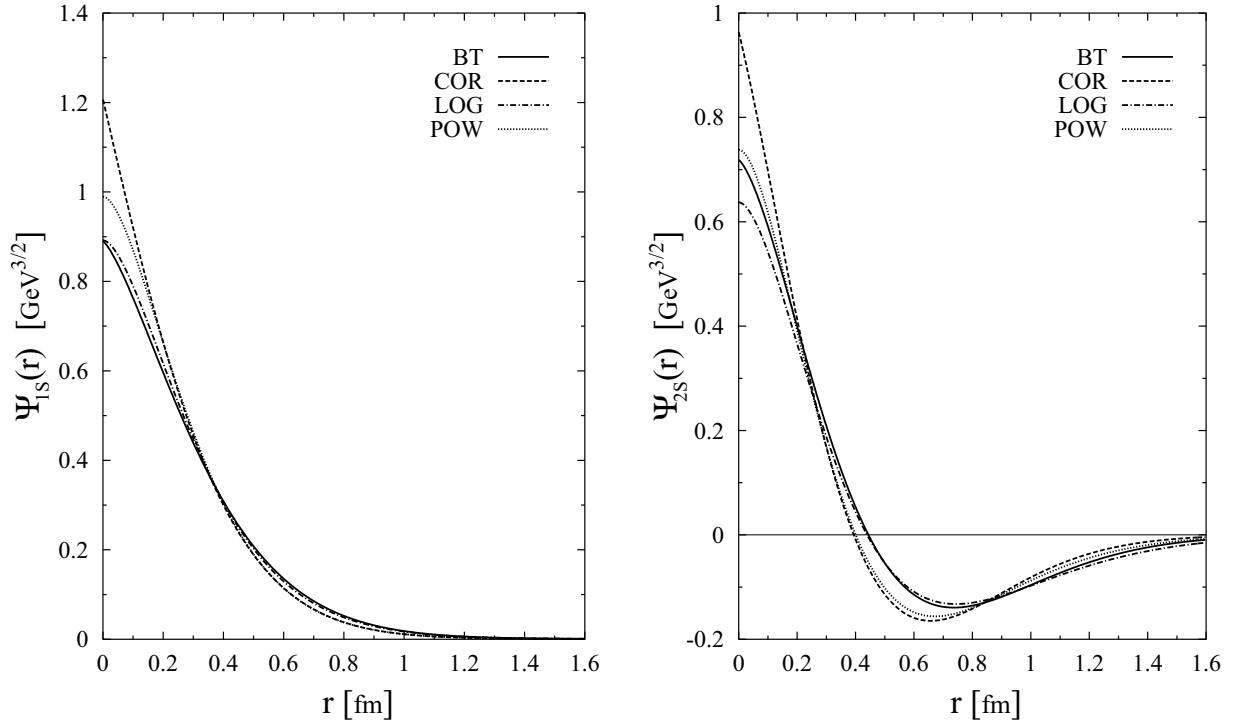


Figure 2.2: Radial Wave functions for the J/ψ (left) and $\psi(2S)$ (right) for different potential models: Buchmüller and Tye (BT), Cornell (COR), Logarithmic (LOG) and Power (POW).

$$V_C(r) = -\frac{4}{3} \frac{\alpha_s}{r} + \frac{r}{a^2} + c_0 \quad (2.4)$$

describes the fine and hyperfine structures of charmonium levels in the leading non-relativistic treatment. By using charmonium data, the coefficients are determined to be $\alpha_s = 0.36$, $a = 2.34 \text{ GeV}^{-1}$, $c_0 = -0.25 \text{ GeV}$, $m_c = 1.84 \text{ GeV}$.

Energy levels and wave functions of the quarkonium system are obtained by solving the non-relativistic Schrödinger equation in terms of the constituent masses and the potential function. The wavefunction, $\Psi(r) = \Psi_{nL}(r)Y_{Lm}(\theta, \phi)$, with $\Psi_{nL}(r)$ and $Y_{Lm}(\theta, \phi)$ being the radial and orbital parts of the wavefunction, gives predictions of quarkonium properties. The radial wavefunctions of the J/ψ and $\psi(2S)$ systems from various potential models are shown in Figure 2.2. Up to 30% differences can be noticed at small values of r .

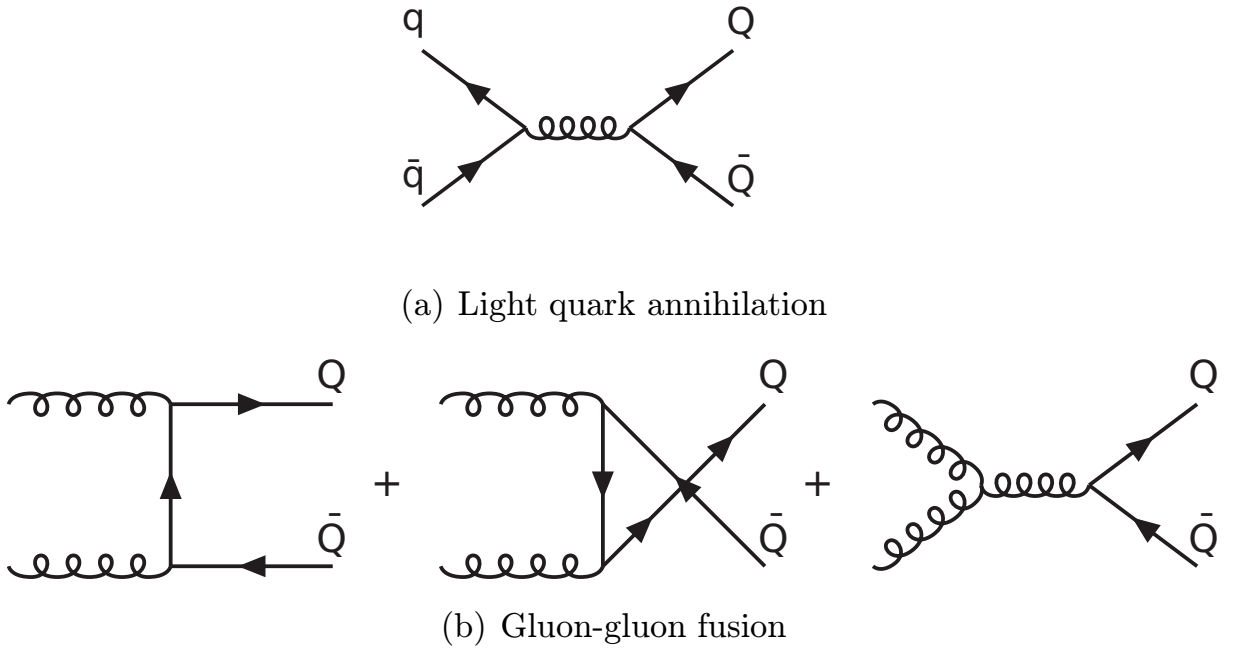


Figure 2.3: Leading-order Feynman diagrams for heavy quark production [18]

2.2 Quarkonium production

The production of quarkonium states can be split in two parts: the production of a heavy quark-antiquark pair in the regime of perturbative QCD, and the formation of a bound state, which is driven by non-perturbative QCD. Many theoretical models have been proposed to interpret the quarkonium production rates measured by experiments.

2.2.1 Colour Singlet Model

The leading order diagrams for the production of a $Q\bar{Q}$ pair are shown in Figure 2.3. Quark-antiquark annihilation produces a pair in an octet state, while gluon-gluon fusion can give a pair in either a singlet or an octet state, mainly the latter. The Colour Singlet Model (CSM) [19] assumes that a given quarkonium state can only be produced from a heavy quark pair with the same quantum numbers. In particular, the quark pair must have the same spin and colour state as the final quarkonium state, i.e. colour neutral. The formation of a quarkonium bound state is parameterised by non-perturbative theory in

the CSM into one single term, assuming the constituent quarks are at rest in the meson frame (*static approximation*). The short-distance cross section for the whole process can be written as

$$d\hat{\sigma}(ij \rightarrow H + X) = d\hat{\sigma}(ij \rightarrow Q\bar{Q} [n^{2S+1}L_J] + X) |\Psi_{nL}^{(k)}(0)|^2 \quad (2.5)$$

where the radial wave functions at the origin can be extracted from the non-relativistic potential models. The wave function $\Psi_{nL}(0)$ is zero for P-wave states (e.g. χ states). For these states, the next term in the amplitude expansion $\Psi'_{nL}(0)$, is used. At order α_s^2 there is only one diagram that contributes for the production of η and χ states. Due to C-parity conservation, the production of J/ψ and Υ states from gluon fusion at leading order is forbidden, and it is described by an α_s^3 term in the CSM. Therefore, this model predicts that the J/ψ production cross section is lower than the χ_c one, which is in disagreement with data.

2.2.2 Colour Octet Model

The Colour Octet Model (COM) [20, 21] extends the CSM calculation and mitigates its shortcomings when compared to data. The COM allows the heavy quark pair produced in the hard process to have different quantum numbers and evolve into a given quarkonium state through radiation of soft gluons during hadronisation. The perturbative hard process is separated from the non-perturbative dynamics, in which the heavy bound states are inherently non-relativistic. The latter process can be described in the formalism of NRQCD (non-relativistic QCD) where a production cross section of a heavy quarkonium state H can be expressed as

$$d\sigma(ij \rightarrow H + X) = \sum_{\mathcal{Q}} d\hat{\sigma}(Q\bar{Q}[\mathcal{Q}] + X') \langle O^H(\mathcal{Q}) \rangle \quad (2.6)$$

where $d\hat{\sigma}(Q\bar{Q}[\mathcal{Q}] + X')$ describes the short-distance production of a $Q\bar{Q}$ pair, $Q\bar{Q}[\mathcal{Q}]$ is the Fock state component of the quarkonium wave function in the colour, spin, and angular

momentum state $\mathcal{Q} = {}^{2S+1}L_J^{[1,8]}$, and $\langle O^H(\mathcal{Q}) \rangle$ is the vacuum expectation value of the operator describing the hadronisation into the final state H. Using NRQCD velocity scaling rules, the quarkonium state can be expanded in terms of the heavy quark velocity v , for example, the S-wave vector meson can schematically be written as:

$$|\psi_Q\rangle = O(1)|Q\bar{Q}[{}^3S_1^{(1)}]\rangle + O(v)|Q\bar{Q}[{}^3P_J^{(8)}]g\rangle + O(v^2)|Q\bar{Q}[{}^1S_0^{(8)}]g\rangle + O(v^2)|Q\bar{Q}[{}^3S_1^{(1,8)}]gg\rangle + O(v^2)|Q\bar{Q}[{}^3D_J^{(1,8)}]\rangle + \dots \quad (2.7)$$

where the lowest order in v corresponds to the CSM case. For P-wave quarkonia, contributions from colour-octet S-wave states are at the same order in v as those from the leading colour-singlet P-wave states. Although the parameters of the non-perturbative matrix elements in NRQCD are free, they are independent of the hard process, therefore they can be extracted from multiple experiments. The application of NRQCD in the COM model provides an acceptable description of the differential J/ψ production cross section to CDF data. For the Υ production, corrections at low p_T are required.

2.3 Production of χ_b mesons at LHC

Recently ATLAS [10], D0 [11] and LHCb [12] observed radial excitations of the P-wave χ_b states in radiative transitions to the S-wave Υ states. Also, the $\chi_b(3P)$ states were observed for the first time, even though the invariant mass resolution was not adequate to separate the different spin sub-states.

The main contribution to the production processes at the TeV scale is due to gluon fusion. As seen before, the production of quarkonia can be factorized into two parts, namely the determination of the transverse momentum of the final state using the initial parton distribution function, and the hadronization process. Vanishing production cross-sections in gluon fusion for $[{}^3S_1](1^{--})$ states, due to charge parity conservation, can be avoided by additional gluon emission in the final state. However, the predicted high p_T spectrum is in contradiction with experimental data. For P-wave mesons, it is difficult to obtain the

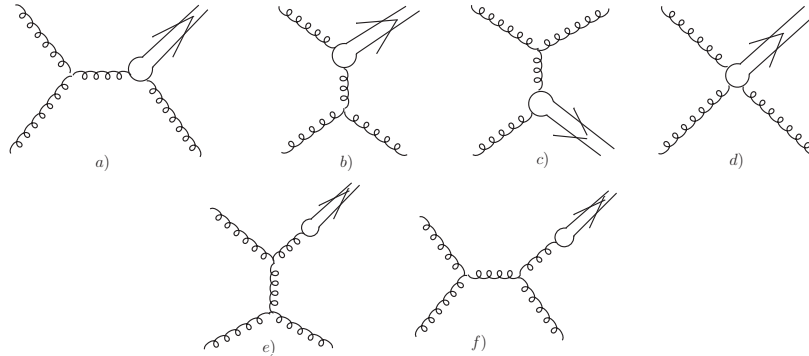


Figure 2.4: From Ref. [22]: Feynman diagrams of the $gg \rightarrow \chi_b g$ NLO process. The diagrams in the top row give both CS and CO contributions, the ones in the bottom row result only in CO contributions.

transverse momentum distribution of final states. In addition, the Landau-Yang theorem forbids the production of axial mesons such as the $|^3P_1\rangle$ state, from two massless gluons.

The authors of Ref. [22] showed that these problems can be overcome by considering next to leading order terms, namely the emission of a single hard gluon, see Fig. 2.4. In this way, all three P-wave states can be produced. The observed p_T dependence of the production cross-section is well reproduced by the color singlet contribution. However, the absolute normalization is several times smaller than measured. This discrepancy can be solved for the χ_c spectrum (see Figure 2.5) by considering color-octet contributions.

The predicted production cross sections of χ_b states are given in Figure 2.6. The ratio of production cross-sections for $J=2$ and $J=1$ states as a function of transverse momentum gives a good description of χ_c data, see Figure 2.7. From that Figure, it is also interesting to notice that the corresponding ratio for χ_b mesons, after rescaling the p_T variable $p_T \rightarrow M_{\chi_c}/M_{\chi_b} p_T \approx 1/3 p_T$, nicely matches the χ_c curve. Unfortunately, as we will see in the following, the invariant mass resolution achieved in this thesis is not adequate to distinguish the different χ_b spin states. An approach based on converted photons might be able to do so in the future, so that these theoretical predictions can be checked.

Finally, the production cross sections for different radial excitations of χ_b states, summed

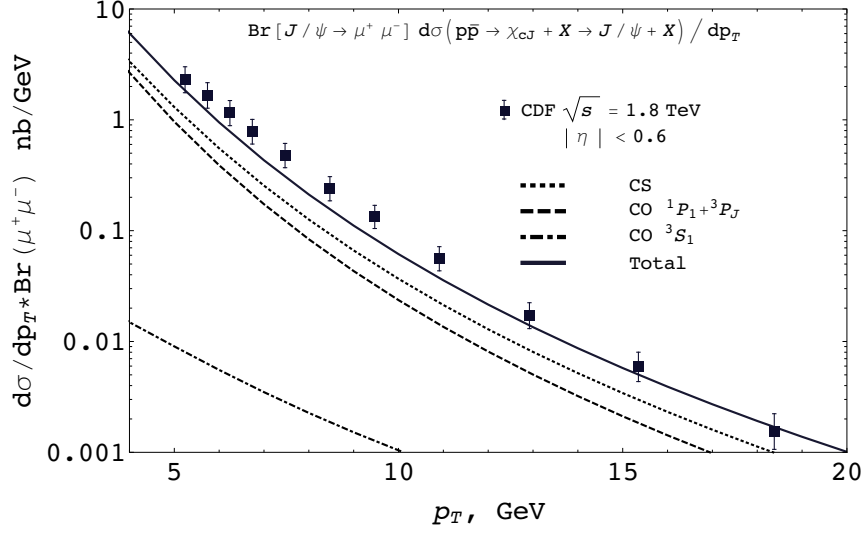


Figure 2.5: From [22]: Differential production cross section for χ_c mesons, as a function of p_T . The different lines correspond to CS (dotted), two different CO contributions (dashed and dot-dashed), total (solid). Experimental points are taken from a CDF report [23].

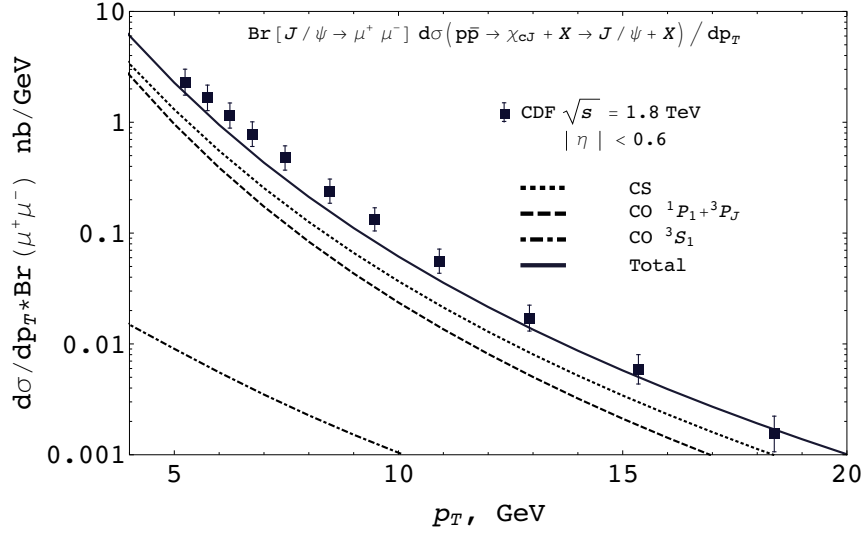


Figure 2.6: From Ref. [22]: Transverse momentum distribution for χ_b states at $\sqrt{s} = 8$ TeV.

over spin states, are predicted and can be compared with experimental measurements. As an example, the following prediction is given for $2 < y < 4.5$ and $6 < p_T < (s - M^2)/2\sqrt{s}$ GeV:

$$\frac{\sigma^{th}[2P, 1S]}{\sigma^{th}[1P, 1S]} = (0.29 \pm 0.01^{th} \pm 0.1^{br}) \left| \frac{R'_{2P}}{R'_{1P}} \right|^2, \quad (2.8)$$

where $\sigma^{th}[nP, mS]$ is the sum over the possible $\chi_b(nP)$ spin states of the production cross section for that state multiplied by its branching fraction for the $\Upsilon(mS)$ decay, $R'_{nP} \sim 1$ is the derivative of the $\chi_b(nP)$ state wave function at the origin, the first uncertainty is due to the theoretical model and the second is due to the experimental values of the branching fractions. Predictions for this ratio in the range between 0.14 and 0.4 have been obtained by using different potential models.

A measurement of the ratio of the $\chi_b(3P)$ and $\chi_b(1P)$ production cross sections can be used, with additional assumption, to infer the $\chi_b(3P)$ radiative branching fractions into $\Upsilon(1S)$.

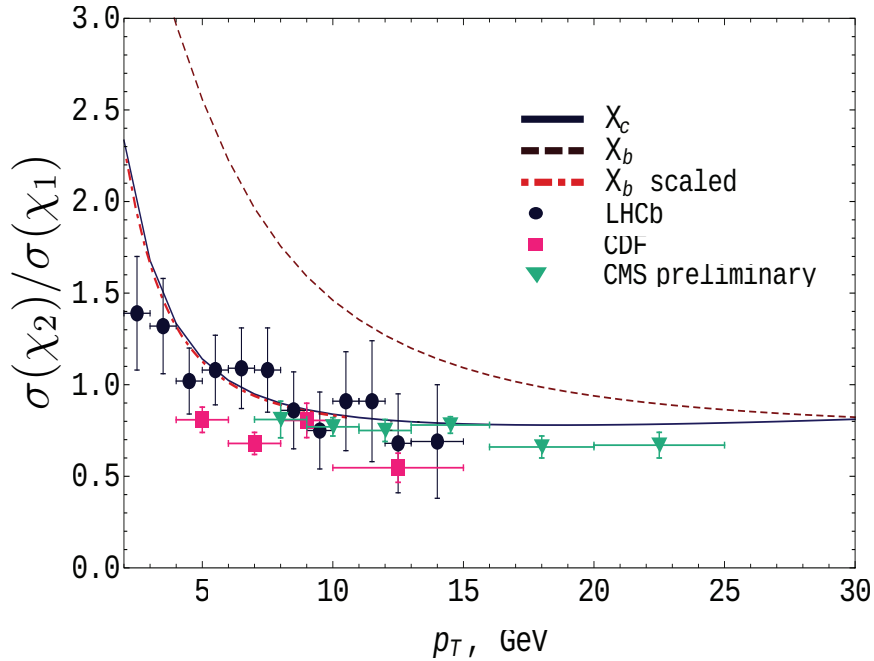


Figure 2.7: This figure is taken from [22] and shows transverse momentum distributions of the $d\sigma[\chi_2]/d\sigma[\chi_1]$ ratio. Solid and dashed lines stand for charmonium and bottomonium mesons. The dot-dashed line corresponds to the rescaled bottomonium ratio: $\sigma_{b2}/\sigma_{b1}(M_{\chi_c}/M_{\chi_b}p_T)$. The experimental results for charmonium from LHCb [24] are shown with dots, CDF [23] — with rectangles, and CMS [25] — with triangles.

Chapter 3

The LHCb experiment

LHCb is a dedicated heavy flavor physics experiment situated at the LHC collider. The primary purpose of this experiment is searching for new physics in CP violation and the rare decays of hadrons containing beauty and charm quarks.

This chapter gives a brief overview of the LHCb detector, describes its sub-detectors and their performance. More detailed information and references on LHCb design and operation can be found in [26].

Firstly the properties of the LHC accelerator are presented, followed by an overview of the LHCb detector. Then the outline of sub-detectors used for tracking and particle identification is given, followed by the description of trigger system that is an important part for selecting the most interesting events while reducing the event rate.

3.1 The LHC

The Large Hadron Collider (LHC) is a circular proton-proton collider located at the European Organization for Nuclear Research (CERN), on the French-Swiss border, near Geneva. Before the injection of the proton bunches into the main LHC ring protons pass through a series of low-energy pre-accelerators, as shown in Figure 3.1.

The initial linear accelerator (LINAC2) accelerates protons to 50 MeV and feeds them through the Proton Synchrotron Booster (BOOSTER), which accelerates them to 26 GeV.

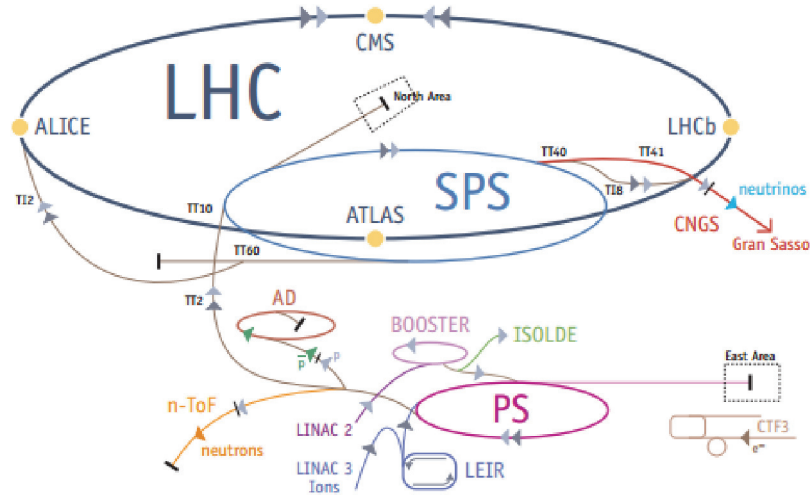


Figure 3.1: The LHC Accelerator System

Finally, protons are injected into the LHC complex at an energy of 450 GeV.

The four main LHC experiments situated at the beam crossing points shown in figure 3.1: ATLAS, ALICE, CMS, LHCb. ALICE dedicated to heavy ion physics. ATLAS and CMS are general purpose detectors, which primary goal is to discover new particles. More details on the LHCb experiment, which collected the data set used in this thesis, are given in the next section.

The new particles are expected to have large masses and their production processes have small cross sections, so the LHC machine is designed with both a center-of-mass energy and a luminosity as large as possible.

The operation of the LHC can be shown as follows: bunches of protons move in opposite direction and are kept in orbit around the 27 km circumference of the accelerator by the magnetic field generated by superconducting dipoles. A temperature of 2K is preserved for magnets' coils to generate a maximum magnetic field of 8 T. This field allows to produce the design center-of-mass energy of $\sqrt{s} = 14$ TeV. Finally the bunches are designed to collide with a frequency of 40 MHz at the interaction points to achieve a design luminosity of $10^{34} \text{ cm}^{-2}\text{s}^{-1}$.

The main LHC design parameters are shown in Table 3.1.

Table 3.1: The main LHC design parameters

Circumference	27 km
Center-of-mass energy	14 TeV
Injection energy	450 GeV
Field at 2×450 GeV	0.535 T
Field at 2×7 TeV	8 T
Helium temperature	2K
Luminosity	$10^{34} \text{ cm}^{-2} \text{ s}^{-1}$
Bunch spacing	25 ns
Luminosity lifetime	10 hr
Time between 2 fills	7 hr

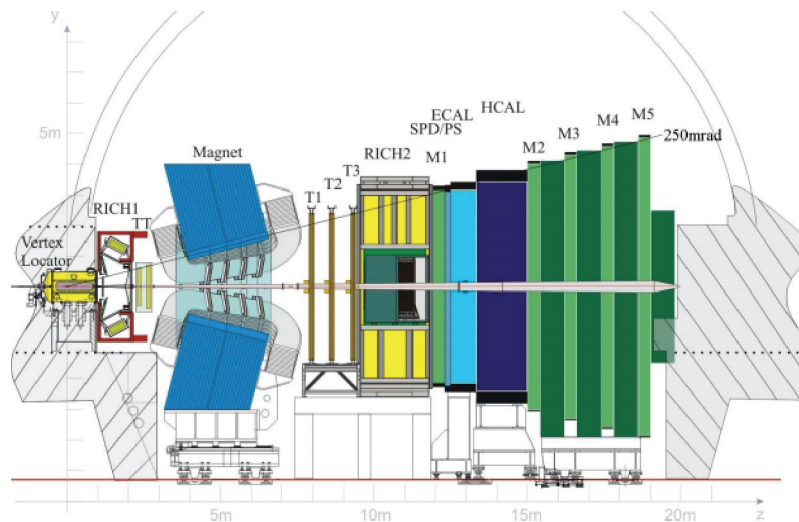


Figure 3.2: Schematic layout of the LHCb detector [26]. The interaction point where the protons collide is on the left of the figure, and sub-detectors are labeled.

3.2 The LHCb experiment

The LHCb detector is a forward single-arm spectrometer with forward angular momentum coverage from 10 mrad to 300 mrad in the bending plane and 10 mrad to 250 mrad in the non-bending plane. These planes are defined by the direction of the field generated by a dipole magnet. The choice of the unique LHCb geometry is justified by the fact, that b-hadrons are predominantly produced in a narrow angular cone in the same forward and backward directions.

LHCb allows the full reconstruction of exclusive decays of the b- and c-hadrons in a variety of leptonic, semi-leptonic and purely hadronic final states. In order to achieve this goal and extract the physics of interest, specialized sub-detectors involved within the LHCb detector to perform the following major tasks:

- **Precision vertexing:** a sufficient separation between primary and secondary vertices is required to efficiently select b-hadron candidates and allow time dependent analyses to be performed. Such measurements are performed by the VERTex LOcator (VELO).
- **Invariant mass determination:** a very good invariant mass resolution is required in order to maximize the significance of signal with respect to background. Therefore, precision energy and momentum estimates of reconstructed tracks must be performed. This is achieved by LHCb's tracking and calorimetry systems.
- **Particle identification:** hadronic decays of b- and c-hadrons, having identical topology but different flavour content in the final state, may peak at a common invariant mass; additional information is required to distinguish them from one another. Discrimination between charged hadrons (particularly pions and kaons) is achieved with a high performance Ring Imaging CHerenkov (RICH) system, whilst electrons, photons and muons are identified via the Calorimeter and Muon systems, respectively.
- **Flexible and robust trigger and data acquisition:** this is required in order to cope with rapid changes in running conditions and physics interests. A dedicated multi-stage trigger, capable of selecting many different final states in an hadronic environment, reduces the data rate from the initial 40 MHz of "visible interactions" to 5 kHz which is suitable for offline storage and analysis.

Figure 3.2 presents the layout of the detector sub-systems within the LHCb detector. More details on each sub-detector will be given in the next sections.

3.3 Tracking system

The tracking system is an important part of the LHCb detector that collects such information about charged particles as vertexing (determining the distance between the production and the decay vertex of the b hadrons) and momentum reconstruction. These two together are used for reconstruction of the mass, the angular and the proper time resolution, that are important for signal selection and background suppression during the offline analysis of $\chi_b \rightarrow \Upsilon\gamma$. Besides this, momentum and decay distance information about momentum and decay distance are used in the trigger.

The LHCb tracking system is composed of a dipole magnet, the VELO and four planar tracking systems: the Tracker Turicensis (TT) upstream of the dipole magnet and three tracking stations T1, T2 and T3 downstream of the magnet. The latter three stations cover the entire geometrical acceptance of the spectrometer. To achieve the excellent tracking performance and also due to track multiplicity considerations, these three stations are composed of two distinct parts called the Inner Tracker (IT) and Outer Tracker (OT). The VELO, TT and IT use silicon strip technology while straw tubes are employed in the OT. In fact, the TT and IT share a common technology, and they are called collectively the Silicon Tracker (ST). They have a very similar layout sharing the same silicon microstrip technology with a strip pitch of 200 μm . Each of the four ST stations is composed of four detector layers with the strip directions arranged in a so called x-u-v-x layout: the first and fourth layers have vertical readout strips, while second (u) and third (v) layers have the strips rotated by a stereo angle of $+5^\circ$ and -5° respectively. This layout is designed to have the best hit resolution in the x direction (in the bending plane), without losing the stereo measurement of the tracks.

3.3.1 Vertex Locator

To provide precise measurements of track coordinates close to the interaction region, the Vertex Locator (VELO), consisting of a series of silicon modules, is arranged along the beam direction. It is used to identify the detached secondary vertices typical for b-hadron

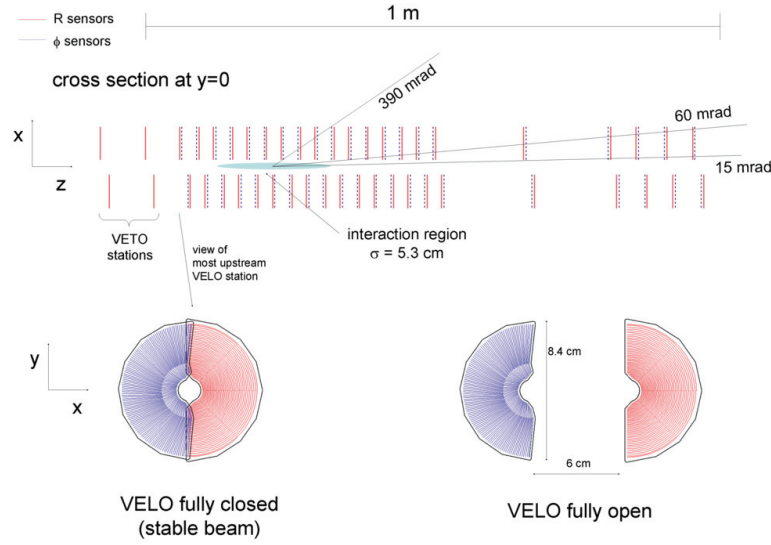


Figure 3.3: The setup of the VELO silicon modules along the beam direction. The left two pairs form the pile-up system. Indicated are the average crossing angle for minimum bias events (60 mrad), and the minimal (15 mrad) and maximal (390 mrad) angle for which at least 3 VELO stations are crossed. 390 mrad is the opening angle of a circle that encloses a rectangular opening angle of 250×300 mrad

decays and makes it possible to meet the requirement to reconstruct B decays with a proper time resolution good enough to resolve the fast time-dependent oscillations or CP asymmetries.

To provide accurate measurements of the position of the vertices, the silicon modules of the VELO are placed close to the beam axis, namely at 8 mm. In order to detect the majority of the tracks originating from the beam spot ($\sigma = 5.3$ cm along the beam direction), the detector is designed such that tracks emerging up to $z = 10.6$ cm downstream from the nominal interaction point cross at least 3 VELO stations, for a polar angular window between 15 and 300 mrad, as shown in Figure 3.3.

To enable fast reconstruction of tracks and vertices in the LHCb trigger, a cylindrical geometry with silicon strips measuring $r\phi$ coordinates is chosen for the modules.

The strips of the r sensor are concentric semi-circles, the ϕ sensors measure a coordinate almost orthogonal to the r-sensor. The geometry is shown in Figure 3.4. A 2D

reconstruction in the r - z plane alone allows to detect tracks originating from close to the beam line in the high-level trigger. These measurements are used to compute the impact parameter of tracks with respect to the production vertex, which is used in the trigger to discriminate between signal and background. The level-0 trigger uses information from the pile-up veto system, two stations located upstream, which make it possible to reject events with multiple pp interactions in one beam crossing.

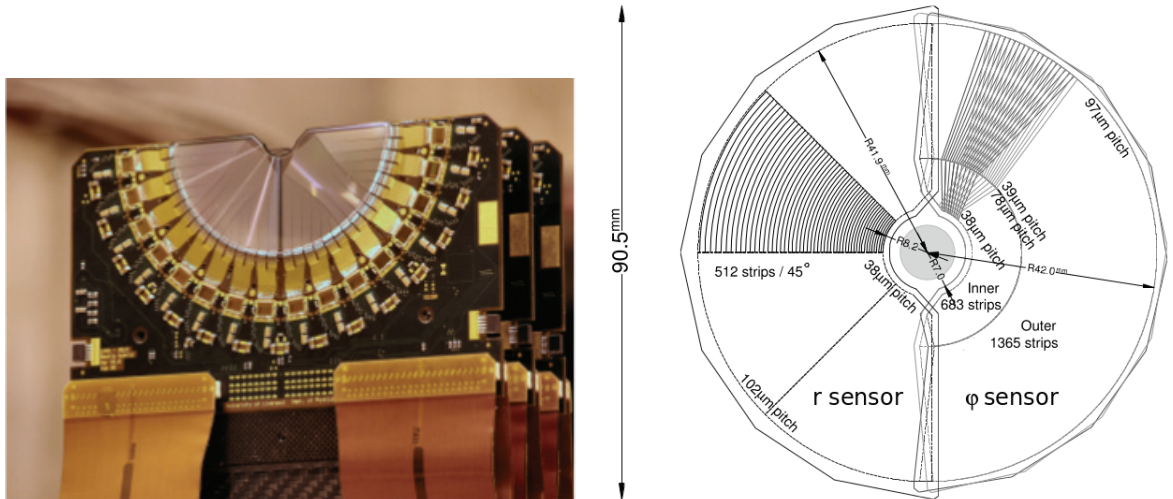


Figure 3.4: The VELO r -sensors (left) and ϕ -sensors (right).

The setup of the VELO is as follows. The half disc sensors are arranged in pairs of r and ϕ sensors and are mounted back-to-back. The sensors are $300 \mu\text{m}$ thick, radiation tolerant, n -implants in n -bulk technology. The minimal pitch of both the r and the ϕ sensors is $32 \mu\text{m}$, linearly increasing towards the outer radius at 41.9 mm . To reduce the strip occupancy and pitch at the outer edge of the ϕ -sensors, the ϕ -sensor is divided in two parts. The outer region starts at a radius of 17.25 mm and has approximately twice the number of strips as the inner region. The strips in both regions make a 5° stereo angle with respect to the radial to improve pattern recognition, and adjacent stations are placed with opposite angles with respect to the radial. In order to fully cover the azimuthal angle

with respect to the beam axis, the two detector halves overlap, as is shown in Figure 3.4.

To minimize the amount of material traversed by particles before reaching the active detector layers, the detector is placed inside vacuum. To separate the primary beam vacuum from the secondary vessel vacuum and shield the detector from RF pickup from the beam, the sensors are separated from the beam vacuum by a thin aluminum foil. Both the sensors and this commonly named RF-foil are contained inside a vacuum vessel. During beam injection the two halves of the VELO are retracted 3 cm away from the nominal beam position. The RF-foil is designed to minimize particle interactions.

3.3.2 Magnet

To provide a good momentum resolution, the LHCb experiment utilizes a (dipole) magnet (see Figure 3.5), which bends the tracks of charged particles. The non-superconducting magnet consists of two saddle-shaped coils. These are placed mirror symmetrically, such that the gap left open by the magnet is slightly larger than the LHCb acceptance, and the principal field component is vertical throughout the detector acceptance.

The quantity important for momentum resolution, and hence for the analysis of channels such as $\chi_b \rightarrow \Upsilon\gamma$, is the integrated magnetic field the magnet delivers. For tracks passing through the entire tracking system this is [26]:

$$\int Bdl = 4Tm$$

making it possible to measure charged particles' momenta up to 200 GeV within 0.5% uncertainty.

3.3.3 Inner tracker

To perform accurate momentum estimates, important for mass, angular and proper time resolutions in the reconstruction of the interesting physics channels, hit information downstream of the magnet is required, which is provided by three tracking stations. Since the magnet bends particles in the horizontal direction perpendicular to the beam pipe,

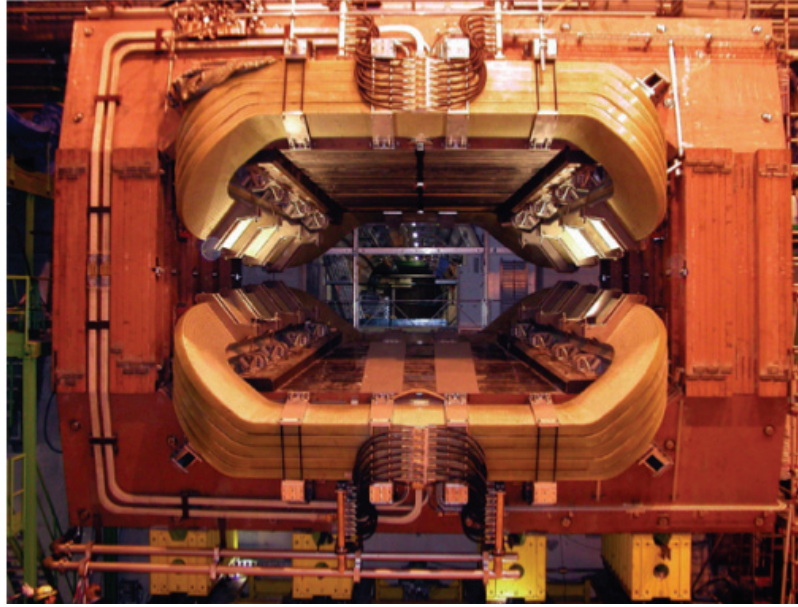


Figure 3.5: The LHCb dipole magnet. The proton-proton interaction region lies behind the magnet.

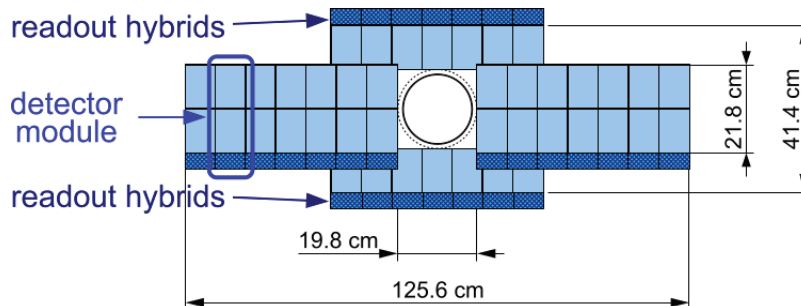


Figure 3.6: Layout of the IT.

the track density is largest in an elliptically shaped region around the beam pipe. In order to have similar occupancies over the plane, a detector with finer detector granularity is required in this region. Therefore, the Inner Tracker (IT), 120 cm wide and 40 cm high, as shown in Figure 3.6, is located in the center of the three tracking stations.

Due to the high track density near the beam pipe, silicon strip detectors are used. The total active detector area covers 4.0 m^2 , consisting of 129024 readout strips of either 11 cm or 22 cm in length. To improve track reconstruction, the four detector layers are arranged

in an x-u-v-x geometry, in which the strips are vertical in the first and in the last layer, whereas the other two (u, v) layers are rotated by stereo angles of $\pm 5^\circ$, providing the sensitivity in the vertical direction.

The pitch of the single-sided p^+ -on-n strips is $198\ \mu\text{m}$. In order to have similar performance in terms of signal-to-noise, the thickness of the sensors is $320\ \mu\text{m}$ for the single-sensor ladders below and above the beam pipe, and $410\ \mu\text{m}$ for the double sensors at the sides of the beam pipe. The four layers are housed in 4 boxes, which are placed such that they overlap. These overlaps avoid gaps in the detector and, more importantly, make it possible to perform alignment using reconstructed tracks.

3.3.4 Outer tracker

Similar to the IT, the Outer Tracker (OT) performs track measurements downstream of the magnet, allowing to determine the momenta of charged particles. The OT covers the outer region of the three tracking stations T1–T3.

Since the track density further away from the beam pipe is lower, straw tubes are used. The total active area of one station is $5971 \times 4850\ \text{mm}^2$, and the OT and the IT together cover the full acceptance of the experiment. As is the case for the IT, these layers are also arranged in an x-u-v-x geometry, as shown in Figure 3.7.

The OT is designed as an array of individual, gas-tight straw-tube modules. Each module contains two layers of drift-tubes with an inner diameter of 4.9 mm. The front-end (FE) electronics measures the drift time of the ionization clusters produced by charged particles traversing the straw tubes, digitizing it with respect to every bunch crossing. Given the bunch crossing rate of 25 ns and the diameter of the tube, and in order to guarantee a fast drift time (below 50 ns) and a sufficient drift-coordinate resolution ($200\ \mu\text{m}$), a mixture of Argon (70%) and CO₂ (30%) is used as counting gas.

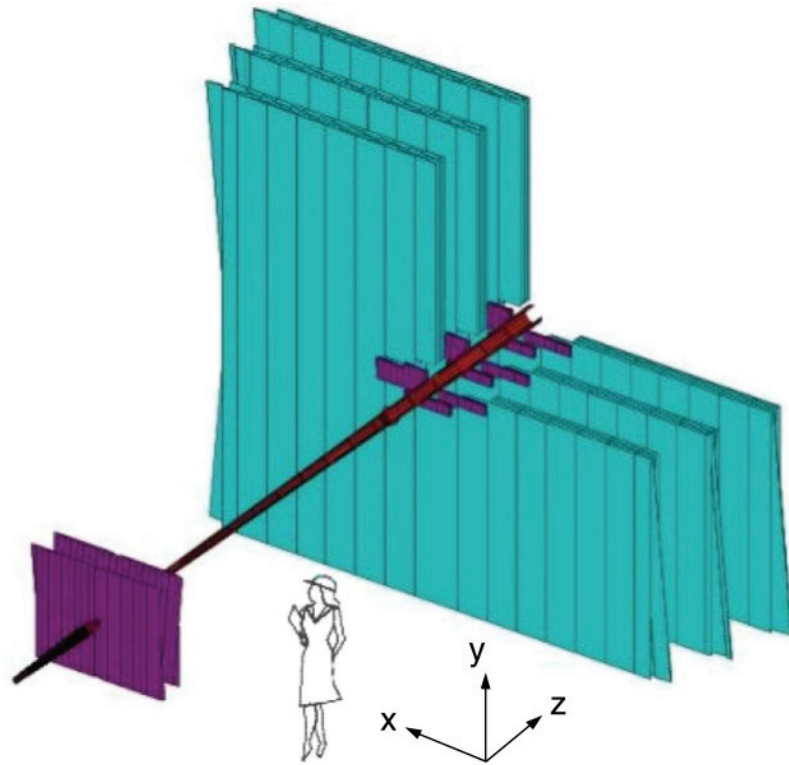


Figure 3.7: Layout of the OT.

3.3.5 Tracker Turicensis

To improve the momentum estimate of charged particles, track measurements are performed before these enter the magnet. Therefore, the Tracker Turicensis (TT), a planar tracking station, is located between the VELO and the LHCb dipole magnet. It is also used to perform the track measurements of long lived neutral particles which decay after the VELO. In addition, by using the weak magnetic field inside the tracker, track information from the TT is used by the High Level Trigger to confirm candidates between the VELO and the tracking stations.

In order to cover the full acceptance of the experiment, the TT is constructed 150 cm wide and 130 cm high. It consists of four detector layers, with a total active area of 8.4 m^2 , with 143360 readout channels, up to 38 cm in length. To improve track reconstruction, the four detector layers are arranged in two pairs that are separated by approximately 27 cm

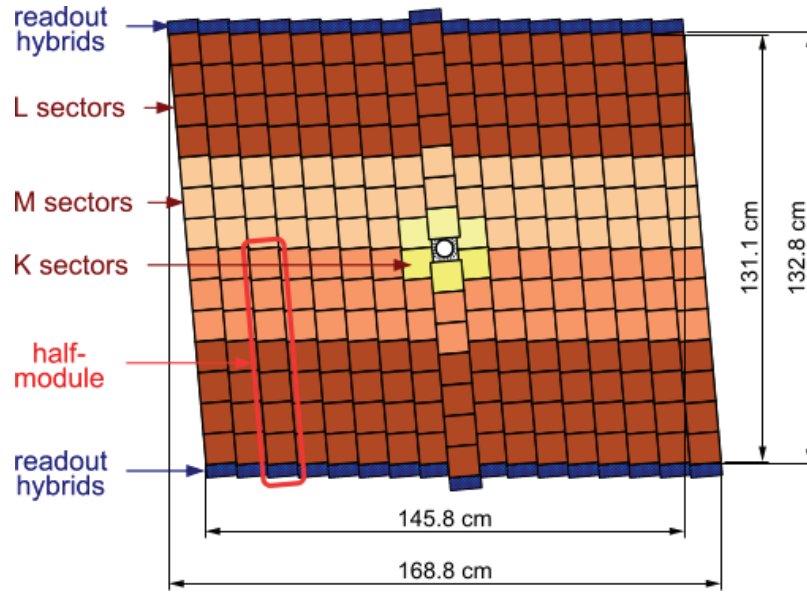


Figure 3.8: Layout of one of the stereo plane detector layers of the TT

along the LHCb beam axis. And again, like the IT and the OT, the TT detection layers are in an x-u-v-x arrangement.

The layout of one of the detector layers is illustrated in Figure 3.8. Its basic building block is a half module that covers half the height of the LHCb acceptance. It consists of a row of seven silicon sensors, named a ladder. The silicon sensors for the TT are $500\ \mu\text{m}$ thick, single sided p^+ -on-n sensors, as for the IT. They are $9.64\ \text{cm} \times 9.44\ \text{cm}$ long and carry 512 readout strips with a strip pitch of $183\ \mu\text{m}$.

3.4 Particle identification

Particle identification (PID) is a fundamental requirement for LHCb. It is essential for the goals of the experiment to separate pions from kaons in selected B hadron decays.

3.4.1 RICH system

There are two RICH detectors in LHCb. RICH1 is located before the magnet (between the VELO and TT) and are used for identification of low momentum particles. RICH2

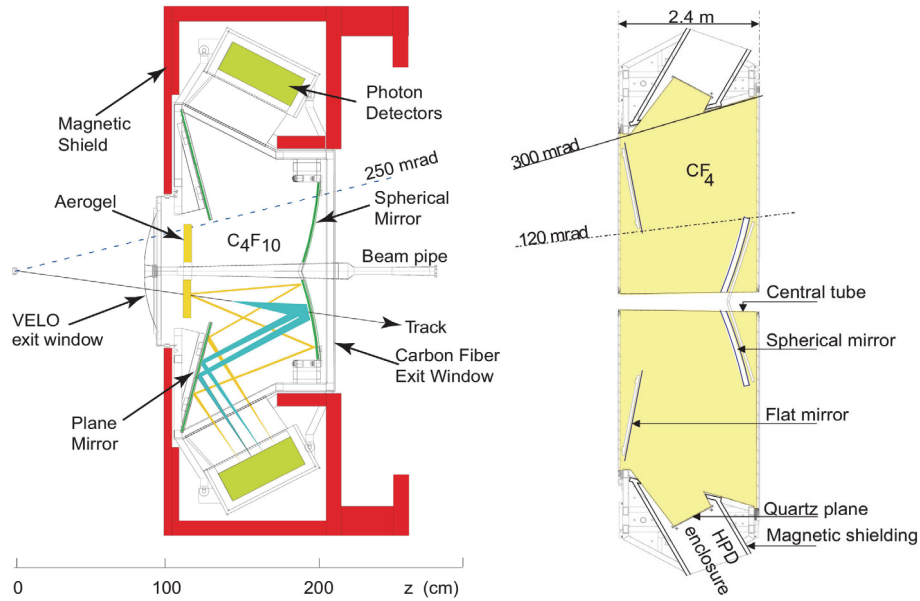


Figure 3.9: Layout of the RICH1 (left) and RICH2 (right) detectors.

is located behind the magnet (between OT and M1) and is used for the identification of high momentum particles. The combination of both detectors allows for kaon and pion separation in the momentum range $2 < p < 100 \text{ GeV}/c$.

The RICH detectors measure the opening angle of the Cherenkov emission cone produced by a charged particle that traverses the medium. The photon emission is focused on the detector surface using a combination of spherical and flat mirrors. The mirrors are tilted to allow the photo detectors to be positioned outside the active area of the detector.

The Cherenkov emission angle θ is given by:

$$\cos \theta = \frac{1}{n\beta}$$

where n is the refractive index of the radiator medium and $\beta = v/c$ is the velocity of the particle. Given the momentum p of a particle and the emission angle θ , the particle mass and therefore the type can be determined.

The RICH1 and RICH2 detectors have different effective momentum ranges, which are determined by the corresponding radiator emission threshold velocity $\beta_{thr} = 1/n$. The

RICH1 detector uses a combination of aerogel and C_4F_{10} gas radiators and covers the low momentum range $1 < p < 60 \text{ GeV}/c$. The RICH2 detector uses a CF_4 radiator and covers the high momentum range $15 < p < 100 \text{ GeV}/c$.

3.4.2 Muon system

The LHCb muon system is designed for muon identification and tracking. It provides information on the transverse energy of the muon to the first level trigger (L0) and muon-ID for the second level trigger (HLT) and offline analysis.

The muon system is composed of five stations (M1–M5) placed along the beam axis (Figure 3.10). Stations M2 to M5 are placed downstream of the calorimeters and are interleaved with iron absorbers. The M1 station is located in front of the SPD/PS and is used to improve the transverse momentum estimate in the trigger. Each station is divided into four regions, R1 to R4, with increasing distance from the beam axis. The granularity of each region is made according to the particle flux, keeping the channel occupancy roughly constant over the four detector regions. For more precise momentum measurement the granularity is higher in the horizontal plane. Muon chambers are the building blocks of the muon system. They are composed of two types of detectors: Multi Wire Proportional Chambers (MWPC), and triple GEM detectors. The latter are used in the inner region of M1, where the expected particle rate exceeds the safe MWPC ageing limit. Twelve GEMs are placed in the higher track density region, while the total system comprises 1392 chambers of various sizes. The MWPCs are subdivided in four tungsten gaps 5mm thick and filled with a gas mixture of Ar (50%), CO_2 (40%) and CF_4 (10%). Inside the gaps, wires with a diameter of $30\mu\text{m}$ are placed at a distance of 2mm from each other.

3.4.3 Calorimeter system

The calorimeter system is designed to measure the energy and position of hadrons, electrons and photons. This information is used in the first level trigger (L0) as well as in the offline

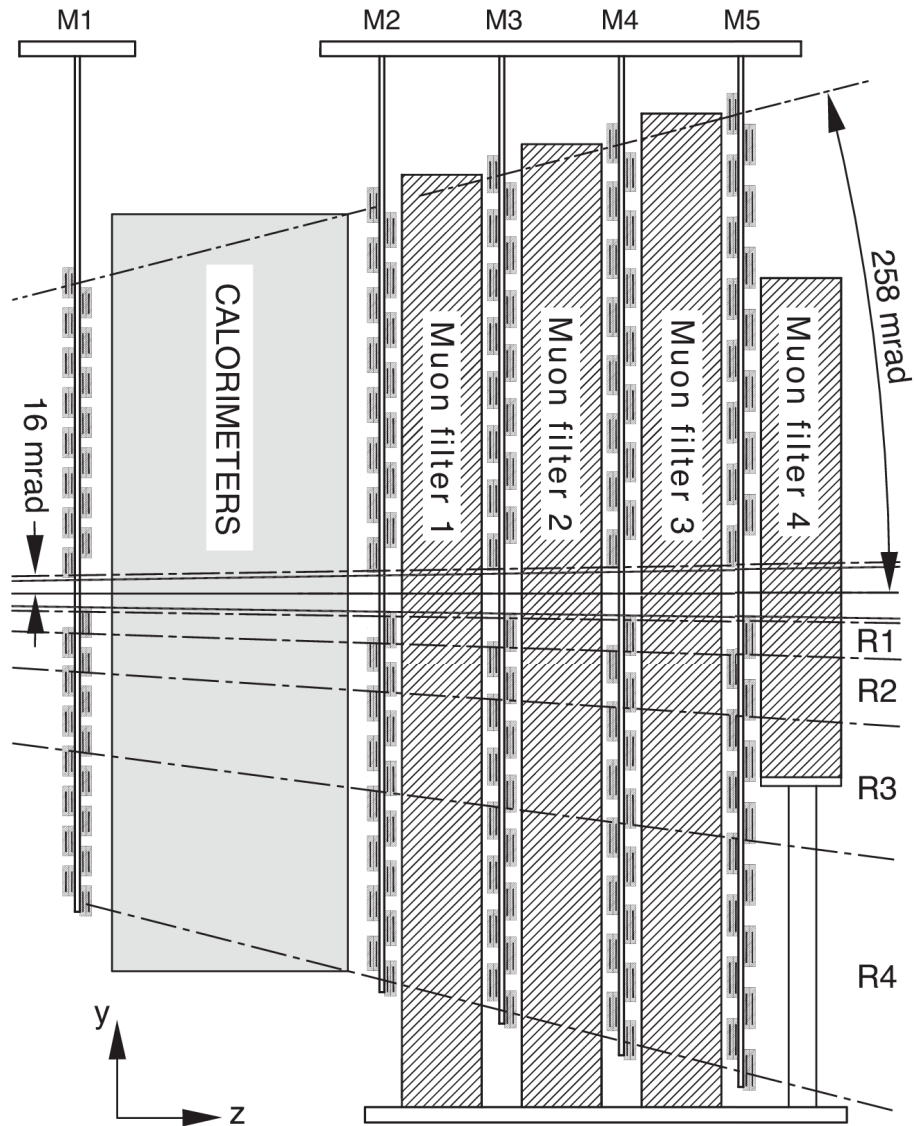


Figure 3.10: Layout of the muon system.

analysis.

The calorimeter system is located between the RICH2 and muon detectors and consists of a scintillator pad detector (SPD), a pre-shower detector (PS), an electromagnetic calorimeter (ECAL) and a hadronic calorimeter (HCAL). The SPD and PS are located in front of the ECAL and provide information on the evolution of the electromagnetic shower. The ECAL serves to measure the energy of electrons and photons, whereas the

HCAL measures the energy of hadrons.

When a particle hits the calorimeter, it produces a cascade of secondary particles. These secondary particles excite the scintillator material, which in turn emits the scintillation light. The light is transmitted through wavelength-shifting fibers to the photomultiplier tubes. The total amount of light collected by photomultipliers is proportional to the energy of the incident particle.

The SPD and PS consist of scintillator pads, separated by a 15 mm thick lead converter. The SPD is used for identification of charged particles before the start of the shower. The lead converter initiates the shower that subsequently is detected by the PS. The SPD allows to separate electrons from photons, whereas the PS is used for separation of electrons and photons from hadrons.

The ECAL consists of lead-scintillator modules and covers the acceptance of $25 < \theta_x < 300$ mrad and $25 < \theta_y < 250$ mrad in the horizontal and vertical planes, respectively. Each module is 42 mm thick and consists of alternating layers of 4 mm scintillator material and 2 mm lead absorber. The modules vary in size from 4×4 cm² in the inner part of the detector, to 6×6 cm² in the middle and 12×12 cm² in the outer part of the detector. The energy resolution of ECAL for electrons and photons is:

$$\left(\frac{\sigma_E}{E}\right)_{ECAL} = \frac{10\%}{\sqrt{E [\text{GeV}]}} \oplus 1\% \quad (3.1)$$

The HCAL is located behind the ECAL. The modules of the HCAL have dimensions of 13×13 cm² and 26×26 cm² in the inner and outer part of the detector, respectively, and consist of alternating layers of 1 cm thick iron and scintillators. The energy resolution of HCAL for hadrons is:

$$\left(\frac{\sigma_E}{E}\right)_{HCAL} = \frac{80\%}{\sqrt{E [\text{GeV}]}} \oplus 10\% \quad (3.2)$$

3.5 Trigger

The LHCb trigger system is used for the selection and storage of events for LHCb physics studies. The general layout of the trigger is shown in Fig. 2.12. The first level trigger Level-0 (L0) is implemented in hardware. The L0 trigger decision is based on the information of the calorimeter and muon systems. Both systems provide information on the multiplicity, and transverse energy E_T or transverse momentum p_T of individual particles. The High Level Trigger (HLT) is the second level trigger of LHCb. The HLT is a software trigger that runs on about 15000 processors of the Event Filter Farm. The HLT, with its two stages HLT1 and HLT2, reduces the 1 MHz L0 rate to about 5 kHz which is permanently stored.

HLT1 reduces the rate from 1 MHz to 50 kHz. HLT1 performs the reconstruction of particles in the VELO and determines the location of primary vertexes and impact parameters (IP) of the particles. The events are selected based on the presence of particles which pass the requirements on the minimum track quality, IP, momentum, and transverse momentum. These selections are based on the decay kinematics of charm and beauty hadrons, such as:

- high average momentum and transverse momentum of charm and beauty hadrons, and consequently their decay products;
- the decay vertex is well displaced from the collision (primary) vertex, and consequently the reconstructed final state particles on average do not point to the primary vertex.

HLT2 reduces the rate from 50 kHz to 5 kHz and is mainly based on inclusive trigger lines that cover most of the B decays with displaced vertexes. In addition, HLT2 contains trigger lines based on the presence of muons and lines aiming at selecting exclusive B decays. HLT2 uses similar requirements on the particles as HLT1, in addition to which the requirements on distance between primary and secondary vertexes, vertex quality, mass and lifetime are used. Figure 3.11 shows HLT schematic overview.

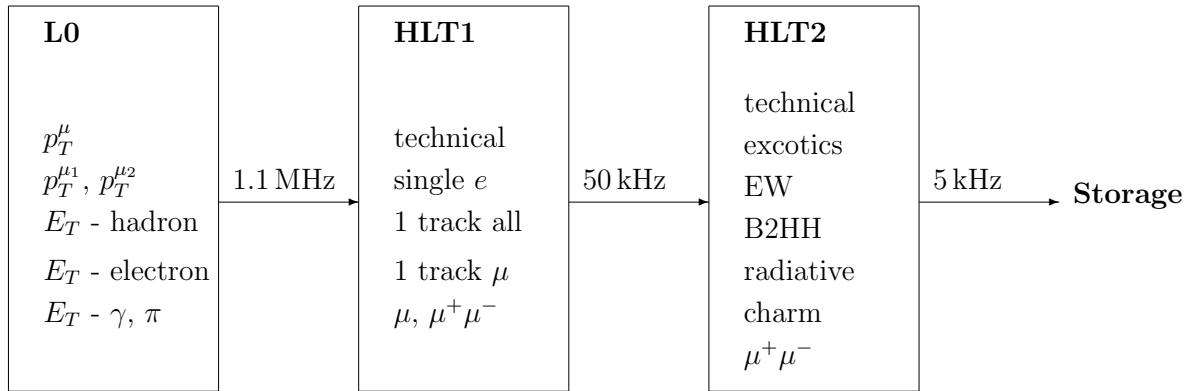


Figure 3.11: Schematic overview of the LHCb trigger.

3.6 LHCb 2010–2012 operation

LHCb operated at center-of-mass energies of $\sqrt{s} = 7$ TeV in 2010–2011 and $\sqrt{s} = 8$ TeV in 2012. Figure 3.12 shows the integrated luminosity delivered and recorded by LHCb in these data-taking periods. In 2011 and 2012, the operation conditions and luminosity were relatively stable and the total recorded luminosity amounts to 1.107 fb^{-1} and 2.082 fb^{-1} in 2011 and 2012 respectively.

The data used in the analysis of χ_b production presented in this thesis correspond to the full datasets collected in 2011 and 2012.

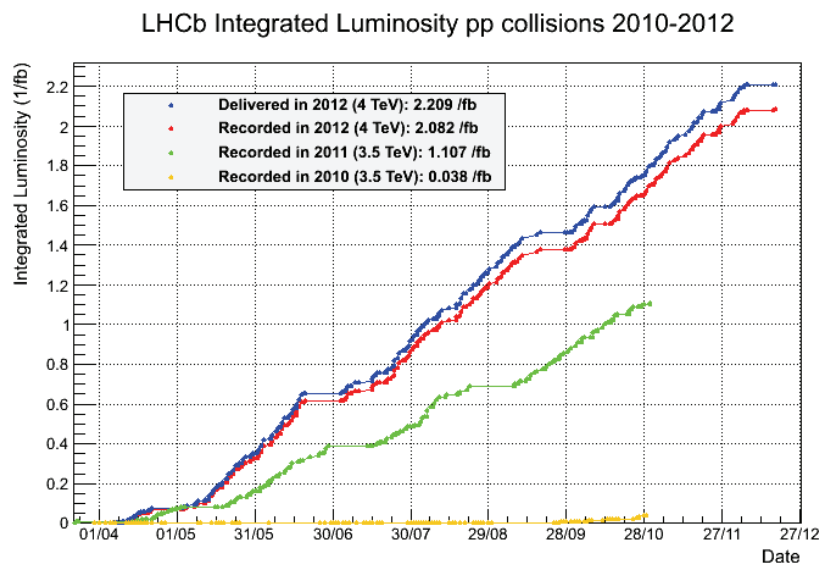


Figure 3.12: LHCb integrated luminosity pp collisions 2010–2012.

Chapter 4

LHCb software performance profiling

4.1 Introduction

In LHCb, as in all High Energy Physics (HEP) experiments, complex software is used to process the data recorded by the detectors. Performance is an essential characteristic of this software, especially when dealing with HLT: its role is to filter events coming from the hardware based trigger in order to identify those with interesting physics, and to write them to disk in real-time. The number of events processed per second (event rate) is therefore one of the crucial characteristics of the HLT, as it has to keep up with the data rate delivered by the hardware triggers (10^6 events per second) in order to avoid data loss. To reach such high throughput, the processing is performed on many nodes in parallel by highly optimized algorithms. In order to optimize the algorithms, and to keep track of the evolution of the event rate when changes are applied to the HLT, it is necessary to measure the overall performance of the code but also to understand which algorithms are costly in term of Central Processing Unit (CPU) and computer memory.

In this chapter our focus is on the analysis of frequency and duration of function calls in algorithms. This type of analysis is commonly named CPU profiling. Profiling helps to identify parts of the code that take a long time to execute. In performance analysis, those places often are referenced as hotspots. Obviously, hotspots affect the event rate of event

processing software. So, one of the main goals of profiling HEP software is to point out to application developers the places in the code that need to be tuned to increase the event rate.

The first study on CPU profiling at LHCb was carried out by Daniele Francesco Kruse and Karol Kruzelecki in their work “Modular Software Performance Monitoring” [27]. They conclude that instead of profiling the application as a whole it would be better to divide it into modules and profile those modules separately. In general terms, a module can be defined as an application’s structural component that is used to group logically related functions. Grouping performance results by module allows a better insight into where the performance issues are coming from. Since each module is under the responsibility of a specific developer, the provided reports can be delivered to the right person. For example, in the GAUDI [28] core framework at LHCb each algorithm used for event processing is such a module which can be profiled independently. More details on GAUDI will be given in Section 4.3.1.

This design principle was first implemented in a set of profiling tools based on `perfmon2` [29] library. These tools have several drawbacks. First, the produced analysis reports used the hardware event counters metrics. Only developers with a good knowledge of the hardware architecture could read and interpret those reports. Since the major part of developers in HEP are physicists, the number of users of those tools are very low. Second, since the current tools do not use the counters multiplexing feature of `perfmon2` library, the target program should be run several times to collect all required hardware counters. As a result, the profiling time is significantly increasing.

To fill some of the the gaps of the previous tools the Gaudi Intel Profiling Auditor was created. This profiling tool uses the same module principle that was described in [27], but is based on Intel[®] VTune[™] Amplifier XE [30]. VTune[™] Amplifier XE is the newer performance profiling tool, that provides better functionality than `perfmon2` library.

In the next section Intel[®] VTune[™] Amplifier XE is briefly reviewed. Then it is discussed how the Gaudi Intel Profiling Auditor can integrate VTune[™] Amplifier XE to the GAUDI framework, and examples of using those tools to profile LHCb’s HLT are

shown.

4.2 Intel[®] VTune[™] Amplifier XE

This section gives an overview of Intel[®] VTune[™] Amplifier XE profiling tool and describes its basic features and analysis reports.

4.2.1 Overview

Intel[®] VTune[™] Amplifier XE is a commercial application for software performance analysis that is available for both Linux and Windows operating systems. VTune[™] Amplifier XE belongs to the runtime instrumentation class of profiling tools. This means that the code is instrumented before execution and the program is fully supervised by the tool. A target application can be profiled without any modification of the codebase.

Intel[®] VTune[™] Amplifier XE has various kinds of code analysis including hotspot analysis, concurrency analysis, locks and waits analysis. In Profiling Auditor a hotspot analysis based on the user-mode sampling feature of VTune[™] Amplifier XE is used. User-mode sampling allows to profile a program by exploring a call stack of a running program and produce one simple metric — the amount of time spent in the function.

The amount of time spent in a function (CPU time) is calculated by interrupting a process and collecting samples of call stacks from all active threads. The CPU time value is calculated by counting the number of a function's appearances at the top of a call stack. This means that stack sampling is a statistical method and does not provide a 100% accurate measurement. However, for a large number of samples the sampling error does not have a serious impact on the accuracy of analysis. More details about sampling accuracy will be provided in Section [4.4.2](#).

VTune[™] Amplifier XE also supports the hardware event-based sampling and provides advanced metrics based on event counters inside a processor. Reports that use those metrics require knowledge of hardware architecture, unlike the user-mode sampling reports that can be understood by any application developers. Furthermore, while the user-mode

sampling can be performed on any 32 and 64-bit x86 based machine, the hardware event-based sampling is targeted only for a specific Intel[®] microarchitecture and requires a special driver to be installed on the operating system. The advantage of the hardware event-based sampling is that it can be used for fine tuning of algorithms in places where the user-mode sampling could not point out the reasons for the hotspot.

The goal of our profiling tool is to provide analysis reports to a wider audience of software developers and, therefore, for implementation we chose the user-mode sampling method over hardware-mode sampling.

4.2.2 Sampling interval

The sampling interval is an important parameter of the user-mode sampling method. It can impact on results accuracy and on total profiling time. Intel[®] recommends to use a 10 ms interval. Using this value the average overhead of the sampling is about 5% in the most applications. The minimum sampling interval value depends on the operating system. For example, a 10 ms interval is the minimum value for the old Linux kernel 2.4, whereas 1 ms is the minimum value for the modern Linux ≥ 2.6 kernels.

To determine an appropriate sampling interval, one should consider the duration of the collection, the speed of your processors, and the amount of software activity. For example, if the duration of sampling time is more than 10 minutes, consider increasing the sampling interval to 50 milliseconds. This reduces the number of interrupts and the number of samples collected and written to disk. The smaller the sampling interval, the larger the number of samples.

4.2.3 Tools

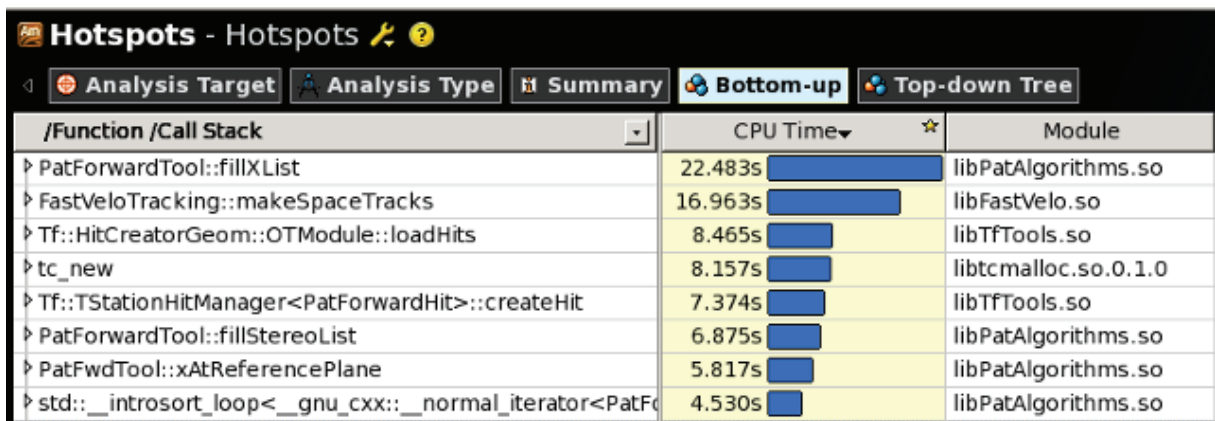
VTune[™] Amplifier XE has two major interfaces — a command-line tool *amplxe-cl* and a Graphical User Interface tool *amplxe-gui*. *Amplxe-gui* generally plays a role of analysis results presenter, but can also be used as a wrapper to the command-line tool. *Amplxe-cl* is used to execute the profiling supervisor with appropriate parameters. The second

important function of *amplxe-cl* is to export CPU usage reports to CSV text format. This feature allows to use collected data not only inside VTune™ Amplifier XE , but also in external user applications.

4.2.4 Profiling reports

In this section we review essential profiling reports that are available in VTune™ Amplifier XE . These reports can be obtained either from *amplxe-gui* or *amplxe-cl tool*, but for short we present only GUI screenshots.

An ordered function’s CPU time usage report is a basic report of almost at all performance profilers (Figure 4.1).



/Function /Call Stack	CPU Time	Module
PatForwardTool::fillXList	22.483s	libPatAlgorithms.so
FastVeloTracking::makeSpaceTracks	16.963s	libFastVelo.so
Tf::HitCreatorGeom::OTModule::loadHits	8.465s	libTfTools.so
tc_new	8.157s	libtcmalloc.so.0.1.0
Tf::TStationHitManager<PatForwardHit>::createHit	7.374s	libTfTools.so
PatForwardTool::fillStereoList	6.875s	libPatAlgorithms.so
PatFwdTool::xAtReferencePlane	5.817s	libPatAlgorithms.so
std::_introsort_loop<__gnu_cxx::_normal_iterator<PatF	4.530s	libPatAlgorithms.so

Figure 4.1: Function’s CPU Time report. The first column contains function names. The second column is a CPU time usage and the last column contains the names of the shared libraries where the functions are defined.

VTune™ Amplifier XE provides many grouping options:

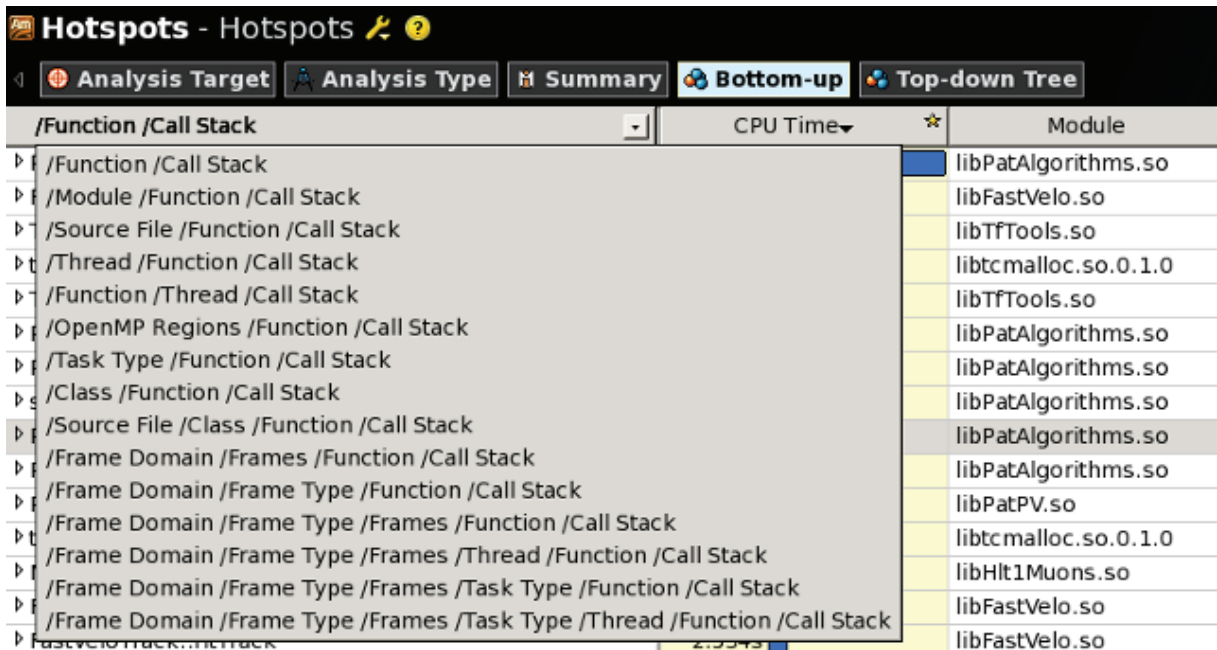


Figure 4.2: Various grouping options.

Example of grouping by shared library:

The screenshot shows the 'Hotspots - Hotspots' application window with the 'Analysis Target' dropdown set to '/Module /Function /Call Stack'. The table displays a CPU time report for various shared libraries, sorted by CPU time. The first column contains the name of the shared library, the second column shows the CPU time in seconds, and the third column shows a horizontal bar representing the time.

/Module /Function /Call Stack	CPU Time
libPatAlgorithms.so	56.804s
libFastVelo.so	38.316s
libTfTools.so	22.738s
libPatPV.so	11.689s
libtcmalloc.so.0.1.0	11.553s
libTrackFitEvent.so	9.607s
libHlt1Muons.so	7.725s
libGaudiKernel.so	7.087s

Figure 4.3: Shared libraries CPU time report. First column contains a name of shared library.

The striking feature of VTune™ Amplifier XE is an ability to filter data based on a selection in the timeline. This feature does not exist in other popular profilers:

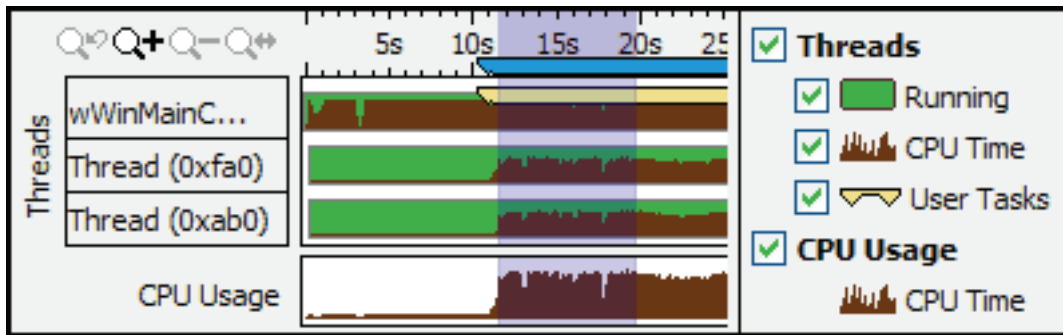


Figure 4.4: Filter data on a selection in timeline.

CPU usage by code line can be created if a target application was compiled with debug symbols:

line	Source	CPU Time
970	info() << format("%7.3f %7.3f %7.3f %7.3f dSin%7.3f, MC: %7.3f %7.3f %7.3f	
971	x, y, sqrt(x*x + y*y), dSin,	
972	xMc, yMc, rMc, (*itH)->distance(xMc, yMc);	
973	printCoord(*itH, ":");	
974	}	
975	if (fabs(dSin) > maxDSin) continue;	0.050s
976		
977	(*itH)->setZ(sensor->z(x, y));	0.100s
978	(*itH)->setPhiWeight(rPred);	0.059s
979	if (0 > firstSensorWithHit) firstSensorWithHit = sensor->number();	0.020s
980	goodPhiHits[module].push_back(*itH);	1.651s
981	}	

Figure 4.5: CPU time usage by code source line.

4.2.5 Detecting code dependency

Besides finding hotspots, another useful function of the profiling tool is to reveal the code dependencies. Usually HEP applications have a lot of lines of code and were developed by many people during a long period of time. Therefore, determining relations between parts of code is very difficult. Since VTune™ Amplifier XE has a top-down tree report of functions calls (Figure 4.6.), we can determine the code dependency in the application and see CPU usage in the call chain.













Call Stack	CPU Time:Total	Module
▽ Selection::Line::Stage::execute	96.3% 	libSelectionLine.so
Algorithm::isEnabled	0.0% 	libGaudiKernel.so
StatusCode::~~StatusCode	0.0% 	libGaudiKernel.so
▽ GaudiAlgorithm::sysExecute	96.3% 	libGaudiAlgLib.so
▽ Algorithm::sysExecute	96.3% 	libGaudiKernel.so
▸ Gaudi::Guards::AuditorGuard::AuditorGuard	0.4% 	libGaudiKernel.so
▽ GaudiSequencer::execute	95.4% 	libGaudiAlgLib.so
▽ GaudiAlgorithm::sysExecute	95.4% 	libGaudiAlgLib.so
▽ Algorithm::sysExecute	95.4% 	libGaudiKernel.so
▸ LODUFromRawAlg::execute	3.0% 	libLODU.so
▸ LoKi::HltUnit::execute	90.6% 	libLoKiTrigger.so
▸ LoKi::LOFilter::execute	0.4% 	libLoKiHlt.so

Figure 4.6: Top-down tree report.

4.3 Gaudi Intel Profiling Auditor

In the previous section we show that Intel[®] VTune[™] Amplifier XE is a powerful performance profiling tool. This section shows how this tool is used at LHCb for software optimization.

First, the GAUDI framework is described and then it is shown how the GAUDI Intel Profiling Auditor can enhance VTune[™] Amplifier XE reports.

4.3.1 Gaudi

GAUDI is a C++ software framework used to build data processing applications using a set of standard components. GAUDI is a core framework used by several HEP experiments, in particular LHCb and ATLAS at LHC. All event processing applications, including simulation, reconstruction, high-level trigger and analysis are based on this framework. By design, the framework decouples the objects describing the data and those implementing the algorithms. Due to this design, developers can concentrate only on physics related tasks in algorithms and usually do not care about other parts of the framework.

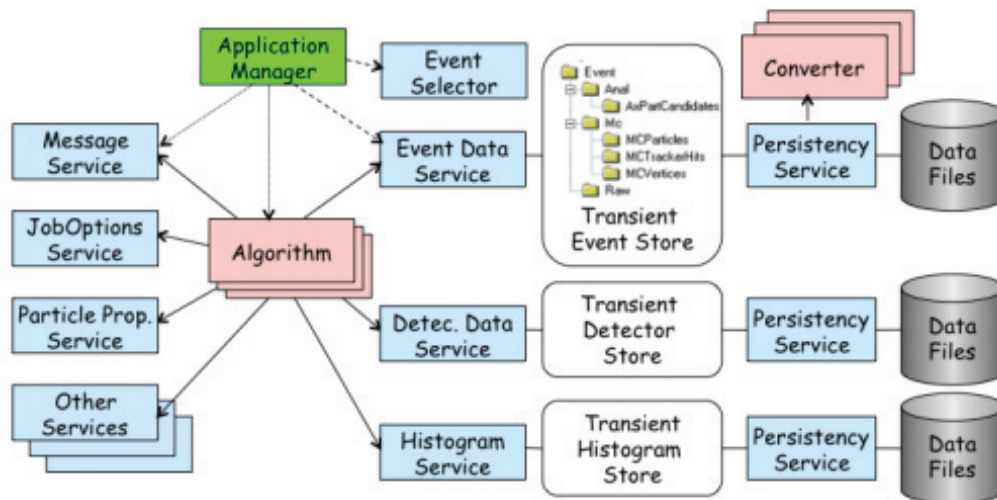


Figure 4.7: Gaudi Architecture (as described in [28]). Applications are made by composing sequences of Algorithms and adding specific Services and Tools.

The GAUDI framework is a highly customizable framework. Any component of the system can be configured by user options.

Gaudi Auditors

The Application Manager is one of the major components of GAUDI. It takes care of instantiating and calling algorithms. A supplement to this component is the Auditor Service that enable to add auditors to a GAUDI application. The auditor is a set of user functions that are called on some workflow events in the Manager. For example, we could add a custom action that is called when the Manager wants to execute some algorithm or when an algorithm is finished. There are many different events types and we can add as many auditors as needed. In other frameworks and programming languages, this type of functions are often referenced as callback functions.

In the following section we show how we can use an auditor to build a profiling tool.

4.3.2 Profiling Auditor

Objectives.

A GAUDI application can be profiled by VTune™ Amplifier XE without any modifications of the codebase. This tool can collect any data about CPU consumption in code lines, functions, classes, shared libraries, threads, but it has one disadvantage. VTune™ Amplifier XE knows nothing about GAUDI framework's algorithms. However, algorithms are the central point of any framework application, since all major event processing occurs there. In principle, a general task for framework users is just to write algorithms that solve a problem and usually nothing more. So, if the profiler could generate a report that can group function's CPU usage by algorithm, then application developers could look to the profiling result from a new point of view. This point of view can help to reveal previously invisible hotspots. In order to provide such report the Gaudi Intel Profiler Auditor was developed.

User API of Intel® VTune™ Amplifier XE .

Each GAUDI algorithm has a name that is assigned to an algorithm at run-time. VTune™ Amplifier XE , in turn, is supplied with a C library that allows to import those names to the target report. In order to use the library from user applications, the public User API is provided in VTune™ Amplifier XE . The API enables to control the data collection process and set marks during the execution of the code. The possibility to mark code regions at runtime is the crucial feature of our new profiling tool, because the CPU usage in the region between algorithm's start and finish points is exactly what is needed for the report that group functions by algorithm. Event API is a part of the User API that is in charge of marking.

```
__itt_event __itt_event_create(const __itt_char name, int namelen );
```

Create a user event type with the specified name. This API returns a handle to the user event type that should be passed into the following APIs as a parameter. The namelen parameter refers to the number of characters, not the number of bytes.


```
int __itt_event_start( __itt_event event );
```

Call this API with an already created user event handle to register an instance of that event. This event appears in the Timeline panel display as a tick mark.

```
int __itt_event_end( __itt_event event );
```

Call this API following a call to `__itt_event_start()` to show the user event as a tick mark with a duration line from start to end. If this API is not called, the user event appears in the Timeline pane as a single tick mark.

Implementation

An auditor is a good component for implementing the required profiling tool. In this case, we do not need to modify the algorithm's code and need only to write two callback functions: at algorithm start and finish. In order to generate the target report those functions need to call Event API functions of VTune™ Amplifier XE .

An appropriate auditor was created and named GAUDI Intel Profiling Auditor. It was deployed to the GaudiProfiling package of GAUDI framework as a shared library. Below we show how this profiling tool marks regions and what reports can be generated.

GAUDI has a special type of algorithms — Sequence. Each instance of Sequence can execute other algorithms or sequences. So, an application's event loop could have not only a flat but also a tree structure. Moreover, the same algorithm instance can occur in different sequences. Therefore, it was decided that an algorithm's region between its start and finish should be marked by the branch identifier. In this case, we get more detailed information about usage of the algorithm in the application. A branch identifier is constructed from an algorithm name and its parents in the sequence tree. For example, let's profile an application that has the following sequence tree:

```
Hlt
```

```
  HltDecisionSequence
```

```
    Hlt1
```

```
      Hlt1DiMuonHighMass
```

```

Hlt1DiMuonHighMassFilterSequence
  Hlt1DiMuonHighMassStreamer
    FastVeloHlt
    MuonRec
    Velo2CandidatesDiMuonHighMass
  GECLooseUnit
    createITLiteClusters
    createVeloLiteClusters
Hlt1DiMuonHighMassLODUFILTERSequence
  LODUFromRaw
  Hlt1DiMuonHighMassLODUFilter

```

In VTune™ Amplifier XE the report that use information on marked regions can be obtained by choosing the “Task Type / Function / Call Stack” grouping options as seen on Figure 4.8.

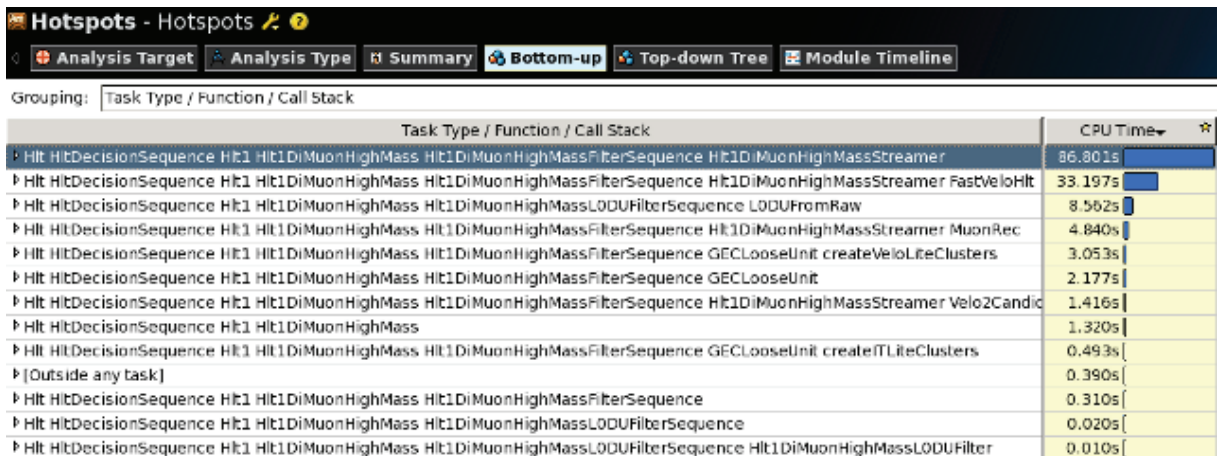


Figure 4.8: Group and order CPU usage by branch identifier.

For example, the selected branch identifier “*Hlt HltDecisionSequence Hlt1 Hlt1DiMuonHighMass Hlt1DiMuonHighMassFilterSequence Hlt1DiMuonHighMassStreamer*” in the report on Figure 4.8 is constructed from the names of algorithms that were executing when the VTune™ Amplifier XE supervisor

sampled a call stack. Each algorithm name in the branch is separated by the space.

For each branch we could see a CPU usage by function (Figure 4.9):

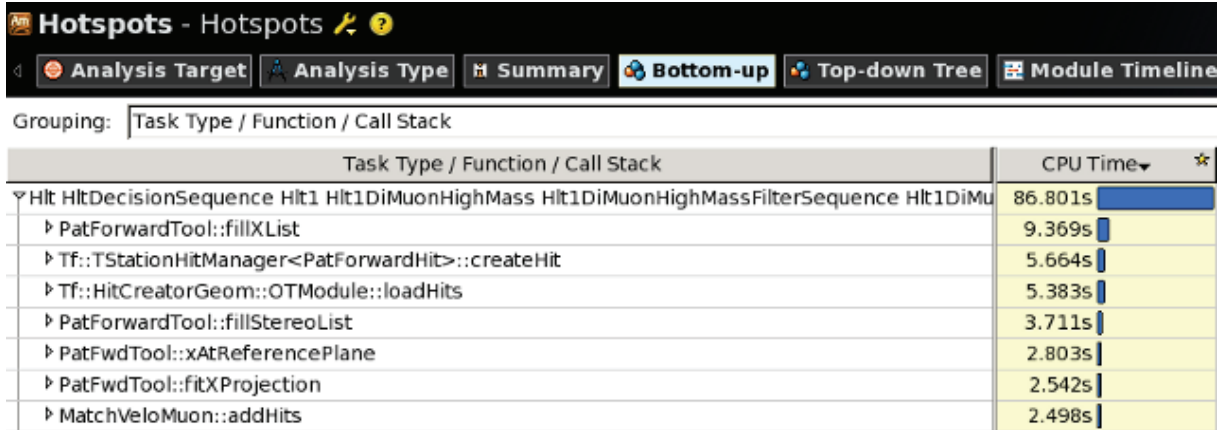


Figure 4.9: Group and order CPU usage by branch identifier.

On Figure 4.9 we see the functions’s CPU usage in the algorithm *Hlt1DiMuonHighMassStreamer* in the branch “*Hlt HltDecisionSequence Hlt1 Hlt1DiMuonHighMass Hlt1DiMuonHighMassFilterSequence*”. As can be observed the main goal was achieved — we get the report that groups function CPU usage by algorithm. So, the next step is only to interpret profiling results by application developers and, if needed, to tune algorithms.

In addition to reports on algorithms, options were added in the GAUDI Intel Profiling Auditor, that allow to skip unimportant regions of the code during profiling. Information about functions in those regions is not collected and, as a result, we get clearer reports and a decrease of total profiling time. For example, usually time critical processes happen in the event loop. Thus, initialization and finalization phases are not interesting for developers. Due to this, the auditor has options that trigger the start of profiling on the first event in the event loop and stop it after the last event.

4.4 HLT Profiling Examples

In the previous section we demonstrated how GAUDI Intel Profiler Auditor can assist in profiling GAUDI applications. The original motivation for creating this auditor was a profiling of HLT applications of the LHCb experiment. As stated in the introduction, trigger programs are most sensitive to the event processing time. Therefore, a performance profiling is an essential tool for the developers of trigger applications. In this section we show three examples of using VTune™ Amplifier XE and GAUDI Intel Profiling Auditor to profile MOORE, the GAUDI based HLT application at LHCb.

4.4.1 Memory Allocation Functions

In the first example we profile a MOORE program twice. The first time a program was executed with the standard memory allocation function *operator new* from *libstdc++* library:

Grouping:

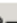

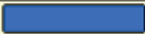




Function / Call Stack	CPU Time  	Module
▶ PatForwardTool::fillXList	23.460s 	libPatAlgorithms.so
▶ FastVeloTracking::makeSpaceTracks	19.788s 	libFastVelo.so
▶ operatornew	18.696s 	libstdc++.so.6
▶ Tf::HitCreatorGeom::OTModule::loadHits	10.870s 	libTfTools.so
▶ Tf::TStationHitManager<PatForwardHit>::createHit	7.981s 	libTfTools.so

Figure 4.10: Hotspot functions in the MOORE application with the standard memory allocation function.

and the second time it was executed with the memory allocation function *tc_new* from *tcmalloc* library [31]:

Grouping:

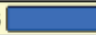
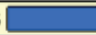




Function / Call Stack	CPU Time  *	Module
▸ PatForwardTool::fillXList	22.483s 	libPatAlgorithms.so
▸ FastVeloTracking::makeSpaceTracks	16.963s 	libFastVelo.so
▸ Tf::HitCreatorGeom::OTModule::loadHits	8.465s 	libTfTools.so
▸ tc_new	8.157s 	libtcmalloc.so.0.1.0
▸ Tf::TStationHitManager<PatForwardHit>::createHit	7.374s 	libTfTools.so

Figure 4.11: Hotspot function in the MOORE application with the memory allocation functions from tcmalloc library.

The figures indicates that *tc_new* function is twice faster than *operator new*. Moreover, a total application time reduction of 5% was observed if we replace standard allocation functions with function from tcmalloc library.

4.4.2 Measuring Profiling Accuracy

To check the CPU time measurement accuracy we compared the results obtained by the GAUDI Intel Profiler Auditor and by the GAUDI Timer Auditor. The Timer Auditor proceeds in the same way as the Profiler Auditor — it calculates the difference between the algorithm’s finish time and the time at the start of the algorithm. Unlike the GAUDI Intel Profiler Auditor, the Timer Auditor calculates the exact time spent in the algorithm. So, we can assume a CPU time observed by the Timer Auditor as a reference value. The limitation of the Timer is that it creates reports only for algorithms times and could not provide results for a low level of granularity (for functions or code instructions). Therefore, only the algorithm’s CPU times were compared.

Since the VTune Amplifier XE instruments the code before execution, the absolute CPU time measured by the Profiler can differ from the time measured by the Timer auditor. But the time distribution of all algorithms should stay the same in both auditors. So, for the test we took a real HLT application and run it twice, by using the Timer auditor the first time and the GAUDI Timer Auditor the second time. We then selected five hotspot algorithms and calculated their time distribution relative to the top hotspot algorithm. The process was repeated three times with different numbers of events: 10

(Table 4.1), 100 (Table 4.2) and 1000 events (Table 4.3):

Table 4.1: 10 events

Algorithm name	Timer (%)	Profiler (%)	Difference
L0Muon	100	100	-
Hlt1TrackAllL0Unit	63.71	63.571	0.139
FastVeloHlt	33.065	7.143	25.922
L0Calo	8.065	0	8.065
HltPVsPV3D	4.032	0	4.032

Table 4.2: 100 events

Algorithm name	Timer (%)	Profiler (%)	Difference
L0Muon	100	100	—
Hlt1TrackAllL0Unit	36.985	42.353	-5.368
FastVeloHlt	29.648	28.235	1.413
L0Calo	7.94	15.294	-7.354
HltPVsPV3D	2.613	4	-1.387

Table 4.3: 1000 events

Algorithm name	Timer (%)	Profiler (%)	Difference
L0Muon	100	100	-
Hlt1TrackAllL0Unit	35.872	35.147	0.725
FastVeloHlt	29.648	28.235	1.413
L0Calo	30.478	29.736	0.742
HltPVsPV3D	2.491	2.25	0.241

As expected, our test shows that the hotspot algorithms are the same in both auditors and the accuracy of the CPU time distribution measured by the Profiler is increasing while

increasing the number of events. As a result, we can be confident that the Profiler can identify the hotspots with high precision.

4.4.3 Custom reports

The second example demonstrates how custom reports can be created. Basic profiling reports can be picked up in VTune™ Amplifier XE , but if a custom report is required then a user tool needs to be created . This application can get the CPU usage data from Intel® VTune™ Amplifier XE XE by using its export function. For example, if we export CPU Time data that is shown on Figure 4.8 then the following pie chart report can be created.

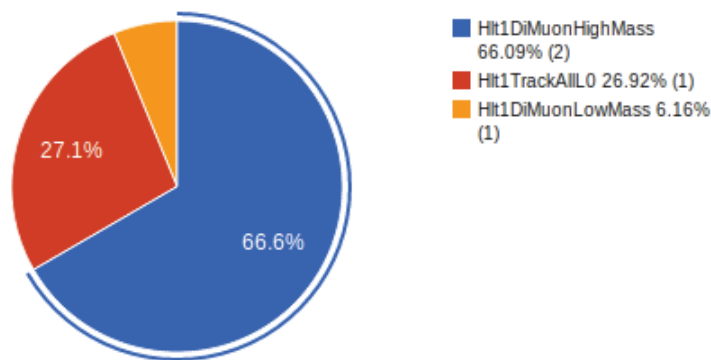


Figure 4.12: CPU Time percentage of top-level algorithms in the GAUDI sequence tree.

The report on Figure 4.12 was produced by a user application that took an exported comma-separated-values (CSV) data and compiled it to javascript code that can be inserted to any dynamic web page.

4.5 Results

In this chapter we presented the GAUDI Intel Performance Auditor — a CPU profiling tool that is used in LHCb experiment at CERN. This tool integrates the functionality of Intel® VTune™ Amplifier XE performance profiler to the LHCb core framework GAUDI.

The key advantage of the auditor is an ability to produce reports that use the framework's modules to present performance analysis results. Those reports help developers to identify hotspots in the code and improve the application performance. Besides the reports, the GAUDI Intel Performance Auditor provides the options that allow to control the Intel® VTune™ Amplifier XE supervisor's process from the GAUDI applications.

The results have further strengthened our confidence in the profiling sampling technique. This technique gives us a reasonable overhead of total profiling time (5% at Intel® VTune™ Amplifier XE) in comparison to the tools that count the functions calls. For example, the popular profiling tool Valgrind [32] counts every code instruction and programs running under this tool usually run from five to twenty times slower than running outside Valgrind. Though Valgrind provides precise measurements, using the sampling technique we can get accurate results by tuning the sampling interval or increasing the number of processing events.

Software optimization has received much attention in the last two years at LHCb. To obtain precise information of the general performance, to make profiling results comparable and to verify the influences of improvements in the framework or of specific algorithms, it is important to rely on standardized profiling and regression tests. Software metrics can be created from the profiling results to monitor the changes in performance and to create reports on a regular basis if modifications lead to significant performance degradations. Therefore, for this purpose a system for systematic profiling is developing at LHCb, where the GAUDI Intel Profiling Auditor is one of the main parts.

Chapter 5

Study of χ_b production

5.1 Introduction

A significant fraction of the production cross-section of J/ψ and Υ states in hadron collisions is due to feed-down from heavier quarkonium states. A study of this effect is important for the interpretation of onia production cross-section and polarization measurements in hadron collisions. For P-wave quarkonia, measurements of χ_c have been reported by CDF [23], HERA-B [33] and LHCb [34], whereas CDF [35] and ATLAS [10] have performed measurements involving χ_b states. LHCb has reported [13] a measurement of the $\chi_b(1P)$ production cross-section, and subsequent decay into $\Upsilon(1S)\gamma$, relative to the $\Upsilon(1S)$ production. This measurement was performed on 2010 data in a region defined by $6 \text{ GeV}/c < p_T^{\Upsilon(1S)} < 15 \text{ GeV}/c$ and $2.0 < y^{\Upsilon(1S)} < 4.5$. The corresponding integrated luminosity was 32.4 pb^{-1} .

A substantial update of the previous LHCb study is presented in this part of the thesis. Data collected in 2012 were also analyzed, allowing for cross-section measurements at $\sqrt{s} = 8 \text{ TeV}$. Using the full integrated luminosity also allows differential measurements in p_T bins of the $\Upsilon(1, 2, 3S)$ mesons, and to study the production of radial excitations such as the $\chi_b(2P)$ and $\chi_b(3P)$ mesons. A measurement of the $\chi_b(3P)$ mass, which was recently observed at ATLAS [10], D0 [11] and LHCb [12] collaborations, is also performed in this

study by combining data collected in 2011 and 2012.

The analysis proceeds through the reconstruction of $\Upsilon(nS)$ candidates via their dimuon decays, and their subsequent pairing with a photon to look for $\chi_b(mP) \rightarrow \Upsilon(nS)\gamma$ decays. The fraction of $\Upsilon(nS)$ originating from $\chi_b(mP)$ decays can generically be written as:

$$\frac{\sigma(pp \rightarrow \chi_b(mP)X) \times Br(\chi_b(mP) \rightarrow \Upsilon(nS)\gamma)}{\sigma(pp \rightarrow \Upsilon(nS)X)} = \frac{N_{\chi_b(mP) \rightarrow \Upsilon(nS)\gamma}}{N_{\Upsilon(nS)}} \times \frac{\epsilon_{\Upsilon(nS)}}{\epsilon_{\chi_b(mP) \rightarrow \Upsilon(nS)\gamma}} = \frac{N_{\chi_b(mP) \rightarrow \Upsilon(nS)\gamma}}{N_{\Upsilon(nS)}} \times \frac{1}{\epsilon_{\gamma}^{reco}} \quad (5.1)$$

where $N_{\Upsilon(nS)}$ and $N_{\chi_b(mP) \rightarrow \Upsilon(nS)\gamma}$ are the $\Upsilon(nS)$ and $\chi_b(mP)$ yields, $\epsilon_{\Upsilon(nS)}$ and $\epsilon_{\chi_b(mP) \rightarrow \Upsilon(nS)\gamma}$ are their corresponding selection efficiencies. The latter are the product of geometric acceptance, trigger efficiency and reconstruction efficiency. Since the selection criteria for the two samples differ only in the reconstruction of a photon, the efficiency ratio can be replaced by $1/\epsilon_{\gamma}^{reco}$, the reconstruction efficiency for the photon from the χ_b decay. The differential production ratios in Υ p_T bins can be computed by using a similar formula.

5.2 Datasets

The measurement of the Υ production cross section is based on proton- proton collision data collected with the LHCb detector at 7 and 8 TeV center-of-mass energies in 2011 and 2012, with corresponding integrated luminosities of 1 fb^{-1} and 2 fb^{-1} .

Signal MonteCarlo

A full event and detector simulation is used for signal studies, and to estimate the photon reconstruction efficiency. The event samples were generated with the LHCb tune of Pythia [36], followed by a full Geant [37] event simulation and LHCb reconstruction.

All χ_b mesons are produced unpolarized. The effect of the initial unknown polarization will be taken into account by event reweighting and a systematic uncertainty will be assigned. During the event simulation the products of χ_b decays are required to have their

momentum pointing into the angular acceptance of LHCb. This requirement is referred to as the generator cut. Only events that have passed this requirement were saved and subsequently reconstructed.

The simulation was performed for both 7 and 8 TeV operating conditions. In total 6.2×10^7 events for all signal modes (χ_b decaying to $\Upsilon\gamma$) and magnet polarities were simulated and stored for subsequent analysis. Table 5.1 shows the number of simulated events for each decay mode.

Table 5.1: Total number of simulated signal events. In each decay mode half of the events were simulated with the LHCb magnetic field pointing upwards, and half with a downwards-pointing magnetic field.

Decay mode	$N_{7\text{ TeV}}, \times 10^6$	$N_{8\text{ TeV}}, \times 10^6$
$\chi_{b1}(1P) \rightarrow \Upsilon(1, 2, 3S)\gamma$	3	4
$\chi_{b2}(1P) \rightarrow \Upsilon(1, 2, 3S)\gamma$	3	4
$\chi_{b1}(2P) \rightarrow \Upsilon(2, 3S)\gamma$	5	5
$\chi_{b2}(2P) \rightarrow \Upsilon(2, 3S)\gamma$	7	7
$\chi_{b1}(3P) \rightarrow \Upsilon(3S)\gamma$	5	5
$\chi_{b2}(3P) \rightarrow \Upsilon(3S)\gamma$	7	7

The procedure to estimate the reconstruction efficiency is described in detail in Section 5.6.2.

5.3 Υ signal extraction

5.3.1 Selection

Pre-selection

The pre-selected event candidates were taken from datasets dedicated to quarkonia studies in LHCb. The selection starts by forming candidates from pairs of oppositely-charged tracks identified as muons and originated from a common vertex. Good track quality is ensured by requiring a χ^2 per number of degrees of freedom (χ^2/ndf) to be less than

4 for the track fit and primary vertex probability greater than 0.5 %. The muons were required to have a transverse momentum higher than 1 GeV/ c . To suppress duplicate tracks a cut on the Kullback-Leibler [38] (KL) distance was used: only tracks with symmetrized KL distance less than 5000 were selected¹. The primary vertex of the dimuon candidate is required to be within the luminous region, defined as $|z_{PV}| < 0.5m$ and $x_{PV}^2 + y_{PV}^2 < 100mm^2$, where z is the beam axis, x and y are the horizontal and vertical directions in the plane perpendicular to the beam axis.

Trigger

For Υ studies the event candidates should pass three trigger levels, with the specific requirement that the muon pair fires the trigger ('Trigger-on-Signal', or 'TOS' requirement). The first level ('L0DiMuon') requires the product of the p_T of the two muon candidates to be greater than 1.68 GeV²/ c^2 , and a loose requirement on the number of hits in the SPD for the whole event (less than 9000 hits).

The second level is the HLT1 trigger, where the event candidates were required to pass the Hlt1DiMuonHighMass line. This line triggers events with two well reconstructed tracks which have hits in the muon system that have a transverse momentum greater than 500 MeV/ c , a momentum greater than 6 GeV/ c , which are originating from a common vertex with an invariant mass greater than 2.7 GeV/ c^2 .

At the last HLT2 level the event needs to be accepted by the HLT2DiMuonB line. This line confirms the HLT1 decision by using better reconstructed tracks, and requires the invariant mass of the dimuon pair to be larger than 4.7 GeV/ c^2 .

Selection criteria specific for this study

To improve the muon identification purity two additional criteria are used. The first one is applied on the difference in logarithm of the likelihood of the muon and hadron hypotheses [39] provided by the muon detection system. This difference ($\Delta \log \mathcal{L}^{\mu-h}$) should

¹The KL distance measures the difference between PDFs that describe track parameters. If the distance is small then two tracks are likely to be clones.

be greater than 0. The second requires a cut on the muon probability value obtained from a Neural Network algorithm (ProbNN). This algorithm takes into account various information such as the RICH particle identification criteria, the muon reconstruction quality and its compatibility with a minimum ionising particle in the calorimeters. In this study a cut on ProbNN value greater than 0.5 is applied.

The criteria for Υ selection are summarized in Table 5.2.

Table 5.2: Summary of Υ selection criteria

Description	Requirement
Track fit quality	$\chi^2/\text{ndf} < 4$
Track transverse momentum	$> 1 \text{ GeV}/c$
$\mu^+\mu^-$ transverse momentum	$6 < p_T(\mu^+\mu^-) < 40 \text{ GeV}/c$
Primary vertex probability	$> 0.5\%$
Luminous region	$ z_{PV} < 0.5m$ and $x_{PV}^2 + y_{PV}^2 < 100mm^2$
Kullback-Leibler distance	> 5000
Muon and hadron hypotheses	$\Delta \log \mathcal{L}^{\mu-h} > 0$
Muon probability	ProbNN > 0.5
Trigger lines:	
L0	L0DiMuon
HLT1	Hlt1DiMuonHighMass
HLT2	HLT2DiMuonB

5.3.2 Fit model

All fits in this study are performed with the RooFit package [40]. To determine the yields of Υ mesons, an unbinned maximum likelihood fit to the dimuon mass distribution has been performed. The signals have been modeled with the sum of three double-sided CrystalBall (DSCB) functions and the combinatorial background by an exponential function with floating τ parameter. Each DSCB function corresponds to the $\Upsilon(1S)$, $\Upsilon(2S)$ and $\Upsilon(3S)$ signals and can be written in the following form:

$$DSCB(x) = N \times \begin{cases} \frac{1}{\sqrt{2\pi\sigma}} \left(\frac{n_L}{|\alpha_L|}\right)^{n_L} \exp\left(-\frac{|\alpha_L|^2}{2}\right) \left(\frac{n_L}{|\alpha_L|} - |\alpha_L| - \frac{x-\mu}{\sigma}\right)^{-n_L} & , \text{ if } \frac{x-\mu}{\sigma} < -\alpha_L \\ \frac{1}{\sqrt{2\pi\sigma}} \left(\frac{n_R}{|\alpha_R|}\right)^{n_R} \exp\left(-\frac{|\alpha_R|^2}{2}\right) \left(\frac{n_R}{|\alpha_R|} - |\alpha_R| + \frac{x-\mu}{\sigma}\right)^{-n_R} & , \text{ if } \frac{x-\mu}{\sigma} > \alpha_R \\ \frac{1}{\sqrt{2\pi\sigma}} \exp\left(-\frac{(x-\mu)^2}{2\sigma^2}\right) & , \text{ otherwise} \end{cases} \quad (5.2)$$

The double-sided CrystalBall is similar to a gaussian distribution, but has asymmetric tails. This function has seven parameters: the number of events N , μ , σ , α_L , n_L , α_R , n_R where parameters μ and σ have the same meaning as for gaussian. Parameters α_L (α_R) and n_L (n_R) describe the left (right) tail behavior: $\alpha_{L,R}$ controls the tail start and $n_{L,R}$ corresponds to the decreasing power of the tail.

In all DSCB functions, the $\alpha_{L,R}$ and $n_{L,R}$ parameters are fixed to the values extracted from fits to the simulated $\Upsilon \rightarrow \mu^+ \mu^-$ decays. The α_L and α_R values are fixed to 1.6, while values of n_L and n_R are fixed to 2 and 11 respectively. All other parameters are allowed to vary in the fit model.

5.3.3 Fit results

Figure 5.1 presents the result of the fit described in the previous section. The fit was performed in the dimuon transverse momentum interval $6 < p_T^{\mu^+ \mu^-} < 40$ GeV/ c . Table 5.3 shows the obtained parameters values.

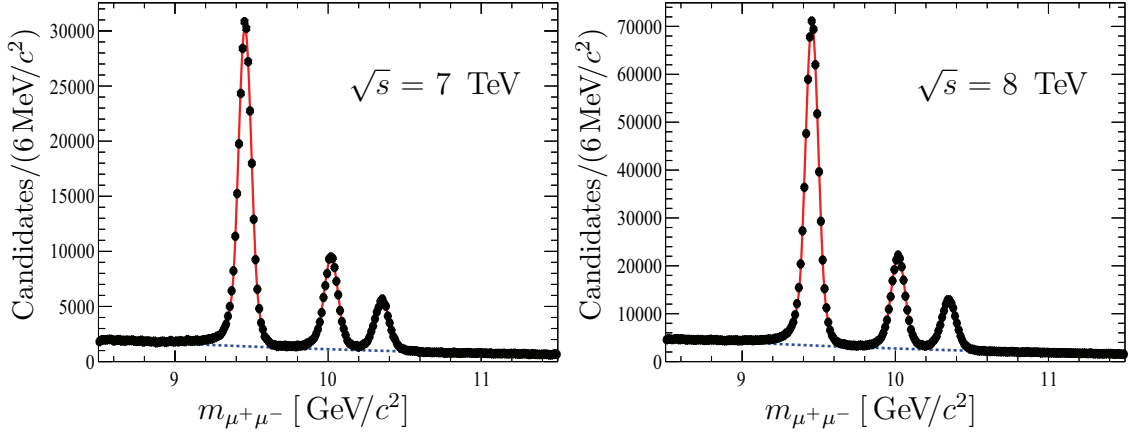


Figure 5.1: Invariant mass distribution of the selected $\Upsilon \rightarrow \mu^+\mu^-$ candidates in the range $6 < p_T^{\mu^+\mu^-} < 40$ GeV/c and $2 < y^{\mu^+\mu^-} < 4.5$. Three peaks correspond to the $\Upsilon(1S)$, $\Upsilon(2S)$ and $\Upsilon(3S)$ signals (from left to right). Curves are the result of the fit described in the previous section 5.3.2.

Table 5.3: $\mu^+\mu^-$ invariant mass data fit parameters

	$\mu^+\mu^-$ transverse momentum intervals, GeV/c 6 – 40	
	$\sqrt{s} = 7$ TeV	$\sqrt{s} = 8$ TeV
$N_{\Upsilon(1S)}$	$283,300 \pm 600$	$659,600 \pm 900$
$N_{\Upsilon(2S)}$	$87,500 \pm 400$	$203,300 \pm 600$
$N_{\Upsilon(3S)}$	$50,420 \pm 290$	$115,300 \pm 400$
Background	$296,400 \pm 700$	$721,300 \pm 1100$
$\mu_{\Upsilon(1S)}$, MeV/c ²	9457.02 ± 0.10	9455.58 ± 0.07
$\sigma_{\Upsilon(1S)}$, MeV/c ²	42.86 ± 0.10	43.04 ± 0.06
$\mu_{\Upsilon(2S)}$, MeV/c ²	$10,019.03 \pm 0.21$	$10,018.05 \pm 0.14$
$\sigma_{\Upsilon(2S)}$, MeV/c ²	46.38 ± 0.20	46.45 ± 0.14
$\mu_{\Upsilon(3S)}$, MeV/c ²	$10,351.16 \pm 0.32$	$10,349.41 \pm 0.16$
$\sigma_{\Upsilon(3S)}$, MeV/c ²	48.63 ± 0.31	48.24 ± 0.11
τ	-0.3887 ± 0.0023	-0.3819 ± 0.0015

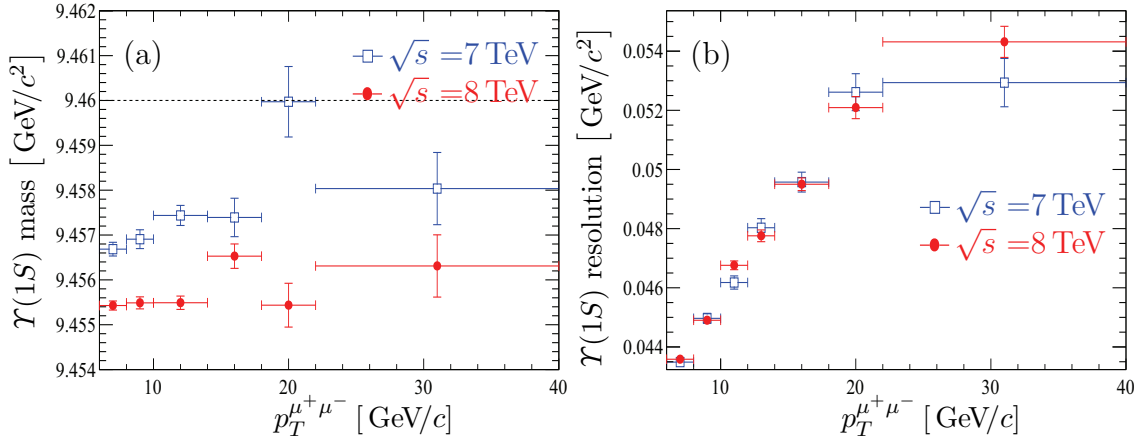
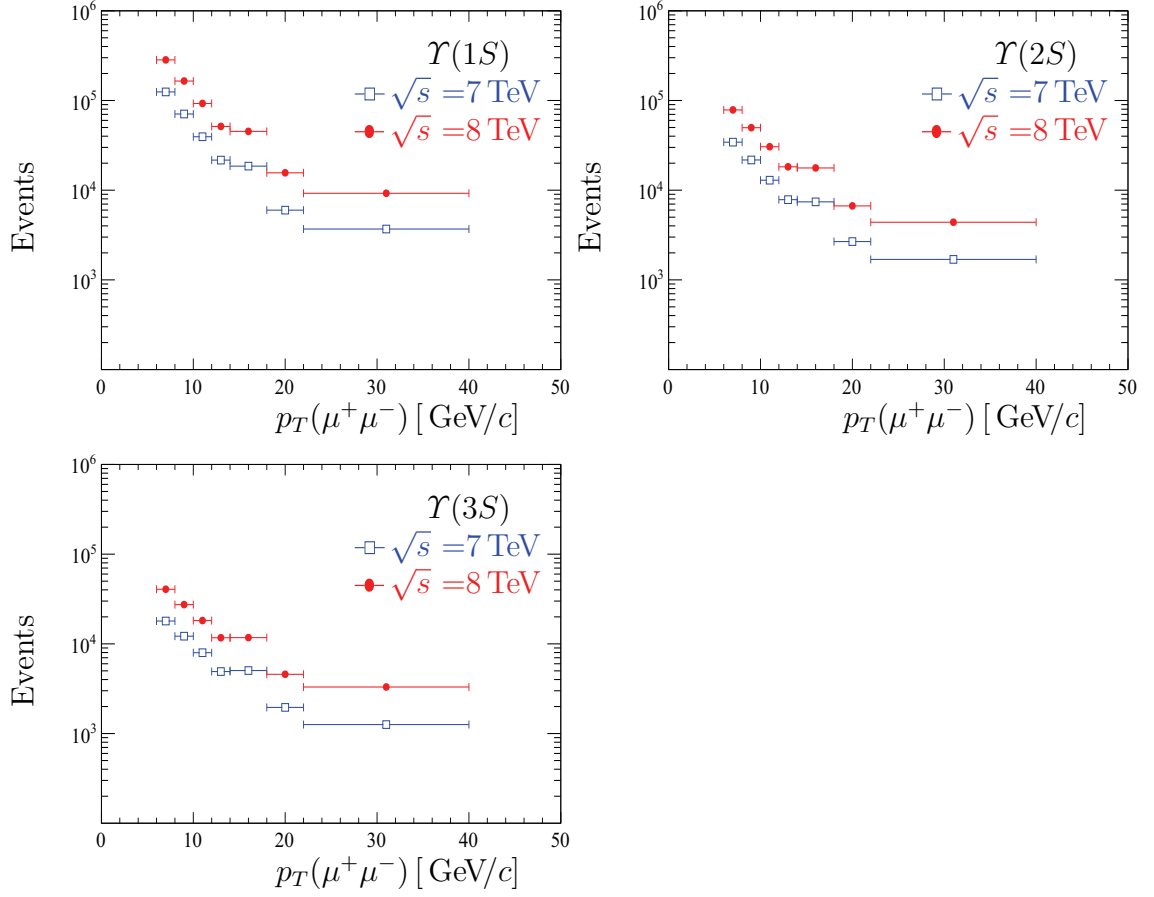


Figure 5.2: Distribution of $\Upsilon(1S)$ mass (a) and peak resolution (b) in $\Upsilon(1S) \rightarrow \mu^+\mu^-$ decay as function of $\mu^+\mu^-$ transverse momentum.

Figure 5.2 shows the fitted $\Upsilon(1S)$ mass differs by 3 ± 2 MeV/c^2 from the PDG value 9460.30 ± 0.26 MeV/c^2 and varies as a function of transverse momentum, as also observed in other studies [41]. A systematic uncertainty is assigned due to this effect. To obtain the final numbers for Υ yields the fit was repeated independently for each $p_T^{\mu^+\mu^-}$ bin with the $\Upsilon(1S)$ mass fixed to 9.456 GeV/c^2 that was measured in the fit of the joined 2011 and 2012 datasets.

Figure 5.3 shows the number of signal events as function of dimuon transverse momentum. Table A.1 in Appendix summarizes the obtained results. Figure 5.4 shows the $\Upsilon(nS)$ yields as a function of transverse momentum, normalized by bin size and luminosity. The small difference between 7 and 8 TeV data is due to the production cross section, which is expected to rise by about 10% for the latter case.

Figure 5.3: Distribution of Υ yields in $\Upsilon \rightarrow \mu^+\mu^-$ decay as function of transverse momentum.

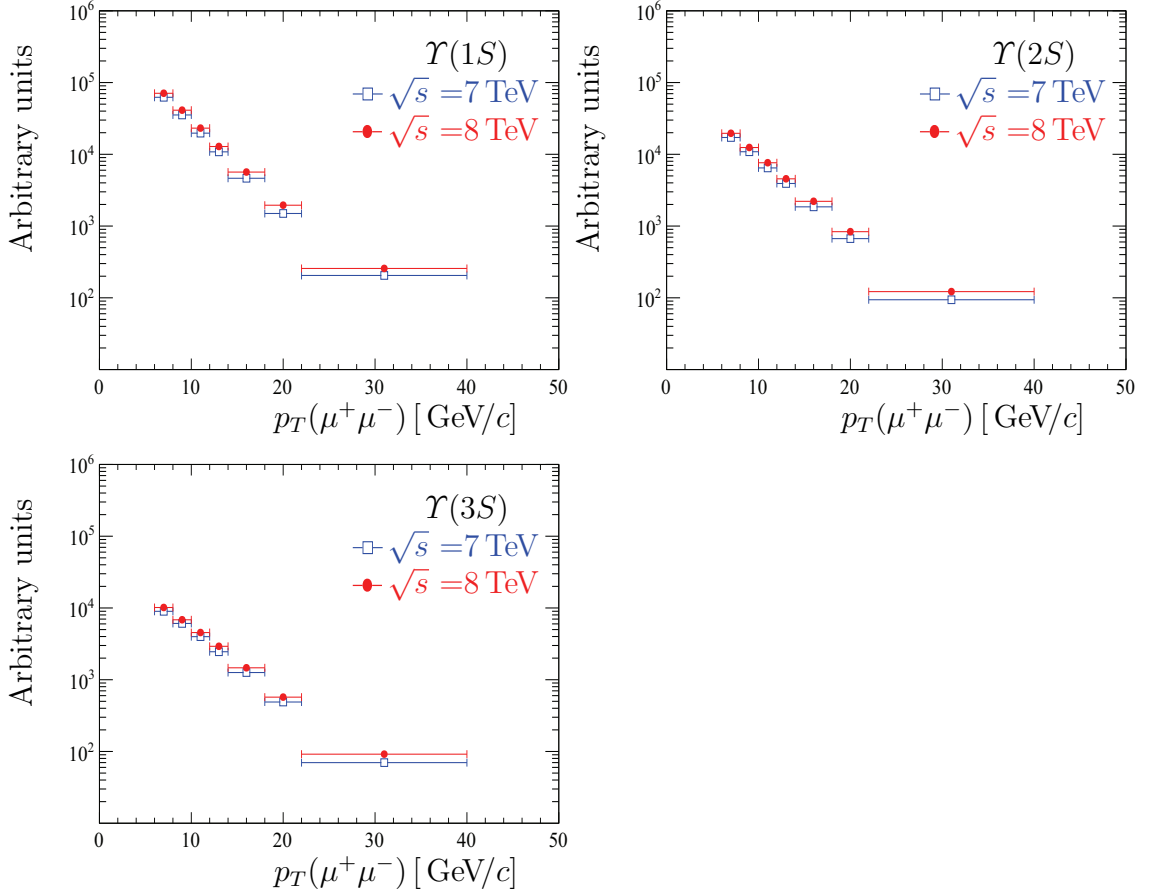


Figure 5.4: Distribution of Υ yields in $\Upsilon \rightarrow \mu^+\mu^-$ decay in specified $\mu^+\mu^-$ transverse momentum ranges. The distribution normalized by bin size and luminosity.

5.4 χ_b signal extraction

In this study, the photon in χ_b decay is measured by the calorimeter system. Another approach is to look at photons that convert to an electron-positron (e^+e^-) pair. Converted photons provide a better invariant mass resolution and would allow to separate mass peaks due to close resonances, since the e^\pm momentum resolution obtained from the tracking stations is better than the photon energy resolution obtained by the calorimeter system. However, conversions should be required to happen before the magnet in order to reconstruct the charged tracks. Furthermore, if the photon converts too early, the e^\pm has more chance to radiate energy, which leads to worse track reconstruction and worse energy

resolution. Therefore, only photons converting before the magnet and after the VELO should be used, which severely limits the size of the available sample and the decays which can be analyzed. In this study unconverted photons are used, in order to obtain a much larger data sample and analyze more decays in a wide range of Υ transverse momentum.

5.4.1 Selection

The selected Υ candidates are combined with photon candidates to form χ_b candidates. Well reconstructed photons are selected by requiring their transverse momentum to be greater than 600 MeV/ c . To further suppress background, the cosine of the angle of the photon direction in the center-of-mass of the $\mu^+\mu^-\gamma$ system with respect to the momentum of this system, is required to be greater than zero. An additional loose cut on the photon confidence level is required to be greater than 0.01. This confidence level is computed starting from the distributions of calorimetric variables which are sensitive to photons, by computing likelihoods under different particle hypotheses, and taking the ratio of the likelihood for a photon hypothesis divided by the sum of likelihoods for all hypotheses.

The criteria for event selection with a reconstructed photon is summarized in Table 5.4:

Table 5.4: The γ selection criteria in $\chi_b \rightarrow \Upsilon\gamma$ decays.

Transverse momentum of γ	$p_T(\gamma) > 600 \text{ MeV}/c$
Polar angle of γ in the $\mu^+\mu^-\gamma$ rest frame	$\cos \theta_\gamma > 0$
Confidence level of γ	$cl(\gamma) > 0.01$

To separate decays into different Υ channels, cuts on dimuon invariant mass are applied as shown in Table 5.5:

Table 5.5: The cuts on dimuon mass window.

Decay	Cut
$\chi_b(1, 2, 3P) \rightarrow \Upsilon(1S)\gamma$	$9310 < \mu^+\mu^- < 9600 \text{ MeV}/c$
$\chi_b(2, 3P) \rightarrow \Upsilon(2S)\gamma$	$9870 < \mu^+\mu^- < 10090 \text{ MeV}/c$
$\chi_b(3P) \rightarrow \Upsilon(3S)\gamma$	$10300 < \mu^+\mu^- < 10526 \text{ MeV}/c$

To avoid $\Upsilon(2S)$ and $\Upsilon(3S)$ contamination, the mass ranges of the $\Upsilon(2S)$ and $\Upsilon(3S)$ are asymmetric with respect to the nominal masses.

The Υ selection cuts (Table 5.2), the cuts on γ (Table 5.4) and dimuon mass (Table 5.5) are used to obtain χ_b yields using a fit model which is described in the next section.

5.4.2 Fit model

This section describes the common properties of the fit model that is used for obtaining yields in each of the χ_b decays. The results of the fits are given in the following sections.

The χ_b signal yields are obtained by fitting event candidates in the distribution of invariant mass difference $m(\mu^+\mu^-\gamma) - m(\mu^+\mu^-)$. In this case any biases and resolution effects from the Υ reconstruction are cancelled at first order. For clearness, the PDG mass of the corresponding Υ particle is added to the mass difference value in each plot.

The $\chi_b(jP)$ (j=1,2,3) signals are the sum of three contributions, due to $\chi_{b0}(jP)$, $\chi_{b1}(jP)$, $\chi_{b2}(jP)$. The χ_{b0} meson is difficult to detect because it has a low radiative branching ratio in comparison with the other two mesons. So the χ_{b0} states were excluded from this study and the fit model.

To determine the χ_b signal yields, an unbinned maximum likelihood fit to $m(\mu^+\mu^-\gamma) - m(\mu^+\mu^-)$ has been performed. The signal has been modeled with a sum of single-sided Crystal Ball (CB) functions. The background is parameterized with a product of an exponential function and a linear combination of basic Bernstein polynomials [42] with non-negative coefficients c_i^2 :

$$\mathcal{B}_n(x) = e^{-\tau x} \times \sum_{i=0}^n c_i^2 \mathcal{B}_n^i(x) \quad (5.3)$$

Such combination results in a smooth and non-negative function that can be used as a PDF.

The CrystalBall function can be written in the following form:

$$CB(x) = N \times \begin{cases} \frac{1}{\sqrt{2\pi\sigma}} \exp\left(-\frac{(x-\mu)^2}{2\sigma^2}\right) & , \text{ if } \frac{x-\mu}{\sigma} > -\alpha \\ \frac{1}{\sqrt{2\pi\sigma}} \left(\frac{n}{|\alpha|}\right)^n \exp\left(-\frac{|\alpha|^2}{2}\right) \left(\frac{n}{|\alpha|} - |\alpha| - \frac{x-\mu}{\sigma}\right)^{-n} & , \text{ otherwise} \end{cases} \quad (5.4)$$

As already mentioned, the CB is similar to a gaussian distribution, but has an asymmetric tail. This function has five parameters: N , μ , σ , α and n , where parameters μ and σ have the same meaning as for gaussian. Parameters α and n describe the tail behavior: α controls the tail start and n corresponds to the decreasing power of the tail.

The number of CrystalBall functions and the order of the polynomial depend on the decay under study and are described in the section corresponding to that specific decay.

The α and n parameters of CB are fixed to the values obtained from simulation (Section 5.6) and are shown in Table 5.6:

Table 5.6: The α and n parameters of CB functions.

Signal	α	n
$\chi_{b1,2}(1, 2P)$	-1.1	5
$\chi_{b1,2}(3P)$	-1.25	5

Due to the small mass difference between $\chi_{b2}(jP)$ and $\chi_{b1}(jP)$ ($j=1,2,3$) states and the insufficient detector resolution, it is not possible to fit the χ_{b1} and χ_{b2} states by two independent CB functions. Thus, the mean, width and yield values of χ_{b1} and χ_{b2} signals are linked together by the following constraints:

$$\begin{aligned} \mu_{\chi_{b2}(jP)} &= \mu_{\chi_{b1}(jP)} + \Delta m_{\chi_{b1,2}(jP)}^{PDG}, \quad j = (1,2) \\ \mu_{\chi_{b2}(3P)} &= \mu_{\chi_{b1}(3P)} + \Delta m_{\chi_{b1,2}(3P)}^{theory} \\ \sigma_{\chi_{b2}} &= k\sigma_{\chi_{b1}} \\ N_{\chi_{b2}} &= \frac{(1-\lambda)}{\lambda} N_{\chi_{b1}} \end{aligned} \quad (5.5)$$

where $\Delta m_{\chi_{b1,2}(jP)}^{PDG}$ is the corresponding PDG mass difference which is fixed in the fit;

$\Delta m_{\chi_{b1,2}(3P)}^{theory}$ is fixed to the theoretical predicted mass difference in $12 \text{ MeV}/c^2$ [43]. The λ parameter depends on the $p_T(\Upsilon)$ range and is fixed to the value that is based on the theoretical prediction discussed in Section 5.5. The parameter k is the ratio between the resolution of χ_{b1} and χ_{b2} signals. This parameter is equal to 1.05 for $\chi_{b1,2}(1P)$ signals and equal to 1 for $\chi_{b1,2}(2, 3P)$ signals.

The width of each CB function (σ) is fixed to the value obtained from simulation (Section 5.6), in order to improve fit convergence and reduce uncertainties.

As already mentioned in the introduction (Section 5.1), the $\chi_b(3P)$ was recently observed, but the mass of this meson was not precisely measured. Section 5.4.5 presents a determination of the $\chi_b(3P)$ mass, which was consequently fixed to the measured value of $10.508 \text{ GeV}/c^2$ in these studies.

5.4.3 χ_b yields in $\chi_b \rightarrow \Upsilon(1S)\gamma$ decays

If χ_{b0} decays are neglected, the $\Upsilon(1S)$ can be produced in radiative decays of six χ_b particles: $\chi_{bi}(jP) \rightarrow \Upsilon(1S)\gamma$ ($i=1,2$; $j=1,2,3$). So the sum of six CB functions is used to determine χ_b signals in these decays. The mass of $\chi_{b1}(1P)$ ($\mu_{\chi_{b1}(1P)}$) is taken as free parameter in the fit, and other parameters are constrained by:

$$\begin{aligned}\mu_{\chi_{b1}(2P)} &= \mu_{\chi_{b1}(1P)} + \Delta m_{\chi_{b1}(2P)}^{PDG} \\ \mu_{\chi_{b1}(3P)} &= \mu_{\chi_{b1}(1P)} + \Delta m_{\chi_{b1}(3P)},\end{aligned}\tag{5.6}$$

where $\Delta m_{\chi_{b1}(2P)}^{PDG}$ is the difference between the PDG masses of $\chi_{b1}(2P)$ and $\chi_{b1}(1P)$. The $\Delta m_{\chi_{b1}(3P)}$ parameter is the difference between the masses of $\chi_{b1}(3P)$ and $\chi_{b1}(1P)$, where the mass of $\chi_{b1}(3P)$ was taken from the measurement performed in this thesis (Section 5.4.5). The parameters $\Delta m_{\chi_{b1}(2P)}^{PDG}$ and $\Delta m_{\chi_{b1}(3P)}$ are fixed in the fit.

The order of the background polynomial in Equation (5.3) depends on the $p_T^{\Upsilon(1S)}$ interval and is given in Table 5.7.

Table 5.7: The order of background polynomial for the $\chi_b \rightarrow \Upsilon(1S)$ fit model

$p_T^{\Upsilon(1S)}$ interval, GeV/ c	Polynomial order (n)
6 — 8	5
8 — 12	4
12 — 40	2

The fit was performed in the mass interval from 9.77 GeV/ c^2 to 10.89 GeV/ c^2 . Figure 5.5 shows the mass distribution along with the pull distribution in the transverse momentum range $14 < p_T^{\Upsilon(1S)} < 40$ GeV/ c . In this range the fit has the lowest relative error of signal yields. Table 5.8 details the corresponding fit parameters.

The pull is the residual divided by the error:

$$Pull = \frac{N_{data} - N_{model}}{\sqrt{N_{data}}}, \quad (5.7)$$

where N_{model} is the expected number of events in a bin from the fit function and $\sqrt{N_{data}}$ is the statistical uncertainty on the number of events in a bin. Pull values for good fits are normally distributed around zero, with a standard deviation of 1.

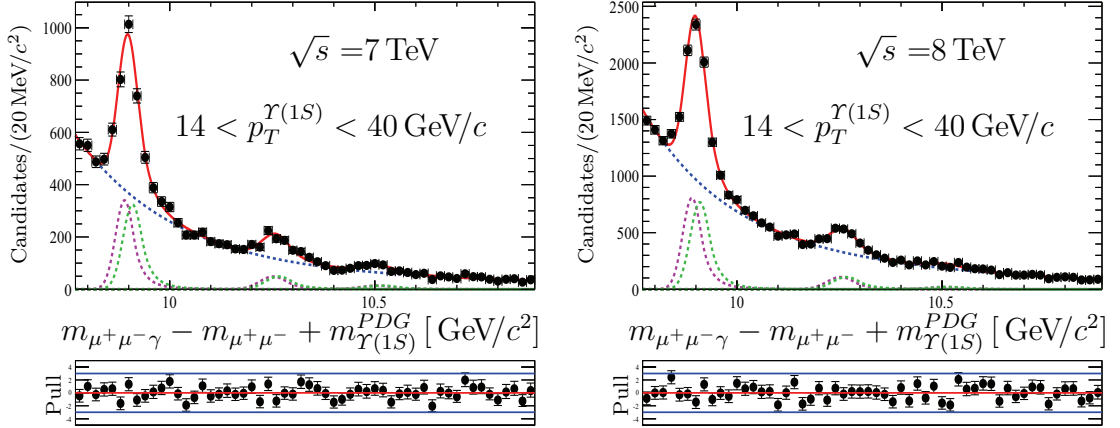


Figure 5.5: Distribution of the mass difference $m(\mu^+\mu^-\gamma) - m(\mu^+\mu^-)$ for selected χ_b (1,2,3P) candidates (black points) together with the result of the fit (solid red curve), including the background (dotted blue curve) and the signal (dashed green and magenta curves) contributions. Green dashed curve corresponds to χ_{b1} signal and magenta dashed curve to χ_{b2} signal. The bottom insert shows the pull distribution of the fit. The pull is defined as the difference between the data and fit value divided by the data error.

Table 5.8: Data fit parameters for $\chi_{b1,2}(1, 2, 3P) \rightarrow \Upsilon(1S)\gamma$ decays

	$\Upsilon(1S)$ transverse momentum intervals, GeV/c 14 – 40	
	$\sqrt{s} = 7$ TeV	$\sqrt{s} = 8$ TeV
$N_{\chi_b(1P)}$	2090 ± 80	5070 ± 130
$N_{\chi_b(2P)}$	450 ± 50	1010 ± 80
$N_{\chi_b(3P)}$	150 ± 40	220 ± 60
Background	8830 ± 130	$23,910 \pm 210$
$\mu_{\chi_{b1}(1P)}$, MeV/c ²	9889.7 ± 1.0	9890.3 ± 0.7
$\sigma_{\chi_{b1}(1P)}$, MeV/c ²	22.0	22.5
$\sigma_{\chi_{b1}(2P)}/\sigma_{\chi_{b1}(1P)}$	1.5	1.5
$\sigma_{\chi_{b1}(3P)}/\sigma_{\chi_{b1}(1P)}$	1.86	1.86
τ	-2.6 ± 0.5	-3.27 ± 0.30
c_0	-0.08 ± 0.12	0.07 ± 0.06
c_1	1.33 ± 0.04	0.29 ± 0.04
$\chi^2/n.d.f$	1.03	1.24

Table 5.8 shows that the measured $\chi_{b1}(1P)$ mass nicely agrees with the PDG value

$9892.78 \pm 0.26 \pm 0.31 \text{ MeV}/c^2$. In the following, this mass was fixed to $9.887 \text{ GeV}/c^2$ which is the value measured on the combined 2011 and 2012 datasets in the range $6 < p_T^{\Upsilon(1S)} < 40 \text{ GeV}/c$.

Figure 5.6 illustrates the number of signal events as a function of $\Upsilon(1S)$ transverse momentum. The yields normalized by bin size and luminosity are shown in Figure 5.7. The $\chi_b(1P)$ and $\chi_b(3P)$ yields are smoothly decreasing functions of $p_T^{\Upsilon(1S)}$, as expected. Differences between 7 and 8 TeV data, due to different production cross sections, can be seen for the $\chi_b(1P)$ state, while they are washed out by statistical fluctuations for the other states. Table B.1 in Appendix summarizes the obtained results.

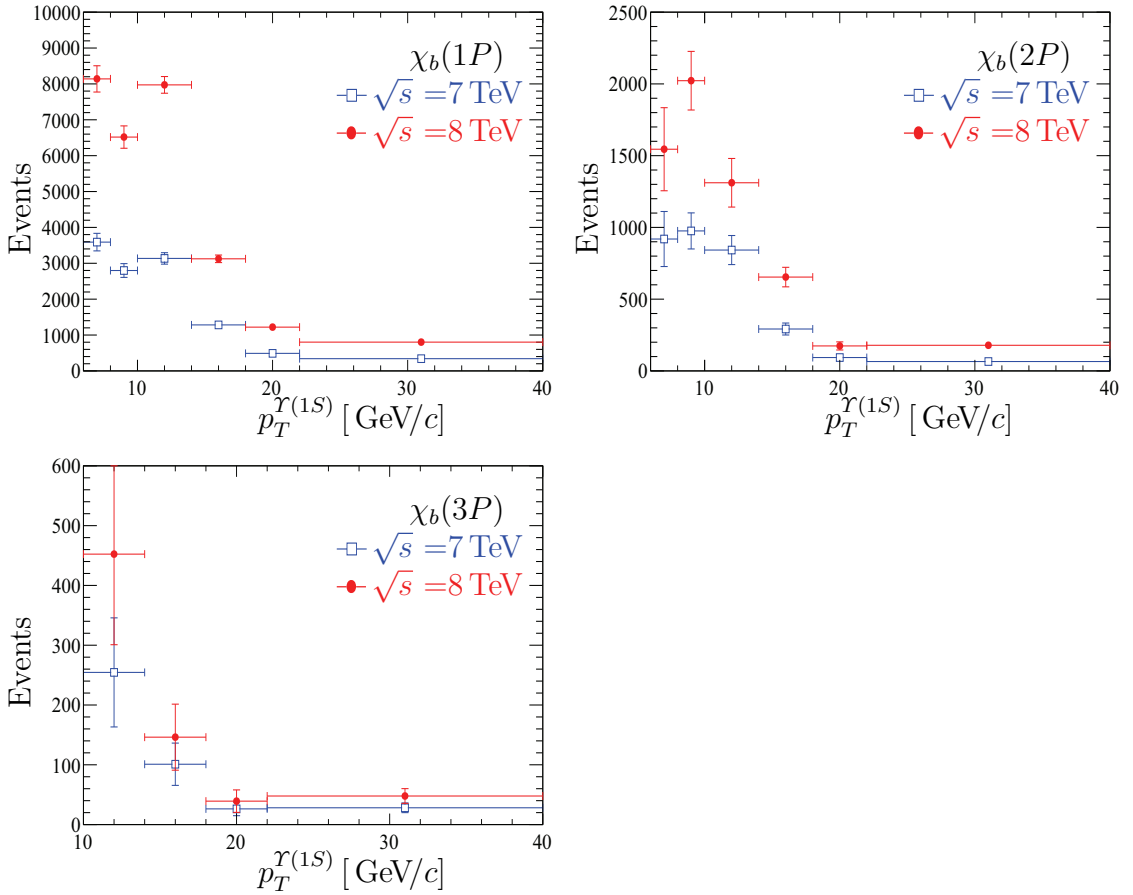


Figure 5.6: Distribution of χ_b yields in $\chi_b \rightarrow \Upsilon(1S)\gamma$ decay in specified $p_T^{\Upsilon(1S)}$ ranges.

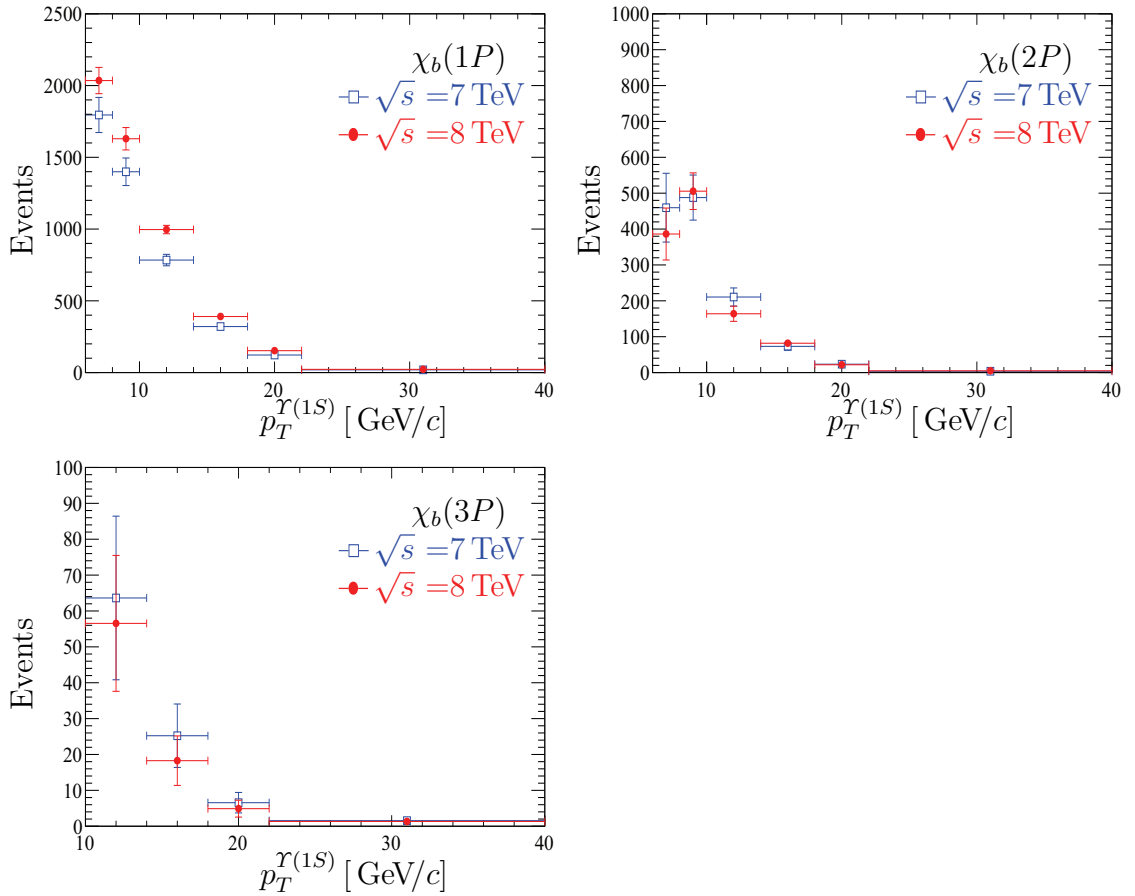


Figure 5.7: Distribution of χ_b yields in $\chi_b \rightarrow \Upsilon(1S)\gamma$ decay in specified $p_T^{\Upsilon(1S)}$ ranges. The distribution normalized by bin size and luminosity value.

Even though a correction on the momentum scale was applied on data, a smooth variation of the $\chi_{b1}(1P)$ mass is observed as a function of transverse momentum (see Figure 5.8). This effect can be explained by the unknown ratio between the number of $\chi_{b1}(1P)$ and $\chi_{b1}(2P)$ candidates. Figure 5.9 shows how the measured mass depends on this ratio (λ parameter). A systematic uncertainty is assigned to this effect.

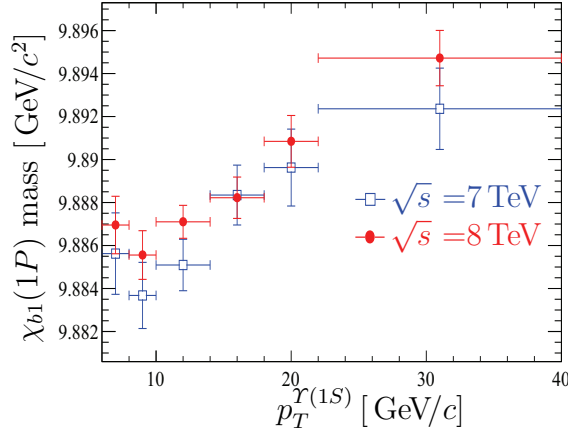


Figure 5.8: Distribution of the $\chi_{b1}(1P)$ mass in $\chi_b(1P) \rightarrow \Upsilon(1S)\gamma$ decay in specified $p_T^{\Upsilon(1S)}$ ranges.

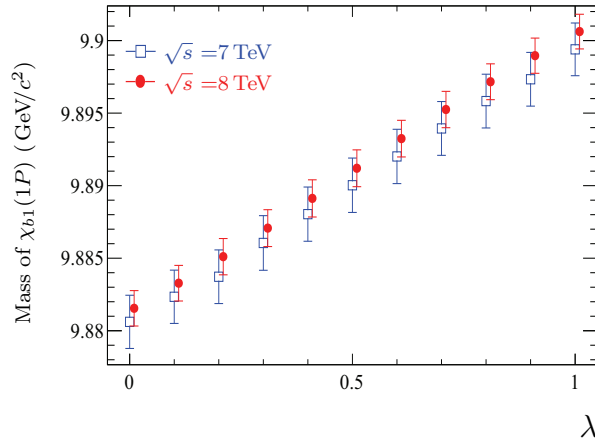


Figure 5.9: Distribution of the $\chi_{b1}(1P)$ mass in $\chi_b(1P) \rightarrow \Upsilon(1S)\gamma$ decay. The mass is measured with different ratios between $\chi_{b1}(1P)$ and $\chi_{b2}(1P)$ states (λ). The measurement is performed in $18 < p_T^{\Upsilon(1S)} < 22$ GeV/c range.

5.4.4 χ_b yields in $\chi_b \rightarrow \Upsilon(2S)\gamma$ decays

The fit was performed in the mass interval from 10.16 GeV/c² to 11.04 GeV/c². The $\chi_{b1}(2P)$ peak width depends on $p_T^{\Upsilon(2S)}$ interval and is fixed to the value obtained from simulation (Section 5.6) without any scaling. The $\chi_{b1}(3P)$ peak width is fixed to $\chi_{b1}(2P)$ peak width scaled by 1.65, as observed on simulation.

The order of the background polynomial in Equation (5.3) is 3 for all intervals of $\Upsilon(2S)$ transverse momentum.

Figure 5.10 shows the mass distribution in the transverse momentum range $18 < p_T^{\Upsilon(2S)} < 40$ GeV/c. Table 5.9 details the corresponding fit parameters.

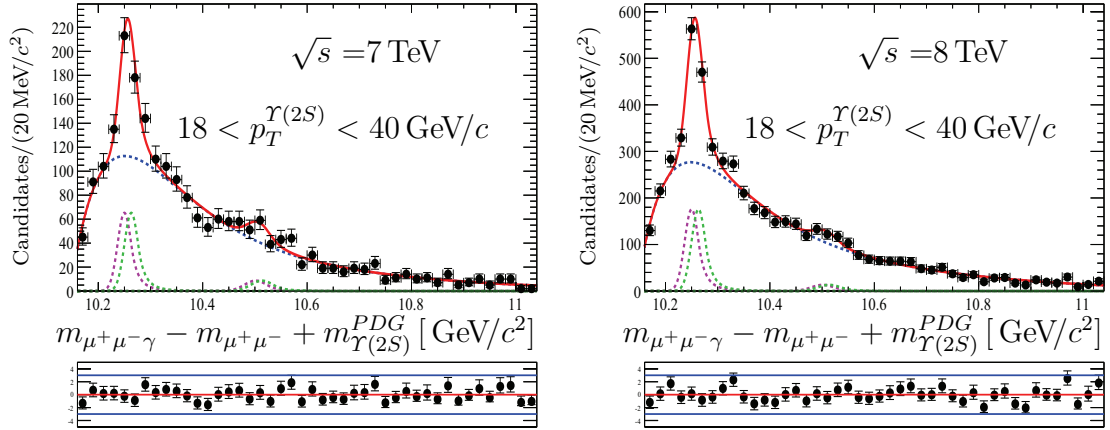


Figure 5.10: Distribution of the mass difference $m(\mu^+\mu^-\gamma) - m(\mu^+\mu^-)$ for selected χ_b (2,3P) candidates (black points) together with the result of the fit (solid red curve), including the background (dotted blue curve) and the signal (dashed green and magenta curves) contributions. Green dashed curve corresponds to χ_{b1} signal and magenta dashed curve to χ_{b2} signal. The bottom insert shows the pull distribution of the fit. The pull is defined as the difference between the data and fit value divided by the data error.

Table 5.9: Data fit parameters for $\chi_{b1,2}(2,3P) \rightarrow \Upsilon(2S)\gamma$ decays

	$\Upsilon(2S)$ transverse momentum intervals, GeV/c 18 – 40	
	$\sqrt{s} = 7$ TeV	$\sqrt{s} = 8$ TeV
$N_{\chi_b(2P)}$	237 ± 29	650 ± 50
$N_{\chi_b(3P)}$	50 ± 17	78 ± 26
Background	1830 ± 50	4600 ± 80
$\mu_{\chi_{b1}(2P)}$, MeV/c ²	$10,249.1 \pm 2.2$	$10,249.9 \pm 1.3$
$\sigma_{\chi_{b1}(2P)}$, MeV/c ²	13.0	13.3
$\sigma_{\chi_{b1}(3P)}/\sigma_{\chi_{b1}(2P)}$	1.65	1.65
τ	-7.5 ± 0.8	-7.7 ± 0.5
c_0	0.431 ± 0.027	0.435 ± 0.016
c_1	-2.07 ± 0.09	-2.12 ± 0.05
c_2	0.79 ± 0.36	0.79 ± 0.17
$\chi^2/n.d.f$	0.98	1.35

Table 5.9 shows that the measured $\chi_{b1}(2P)$ mass is about 5 MeV/c² less than the PDG value $10255.46 \pm 0.22 \pm 0.50$ MeV/c². The same difference is also observed in the smaller $p_T^{\Upsilon(2S)}$ ranges (Figure 5.11). In the following analysis this mass was fixed to 10.250 GeV/c², which was measured in the $18 < p_T^{\Upsilon(2S)} < 40$ GeV/c interval on the sum of 2011 and 2012 datasets, and the systematic uncertainty on the results due to this assumption has been determined.

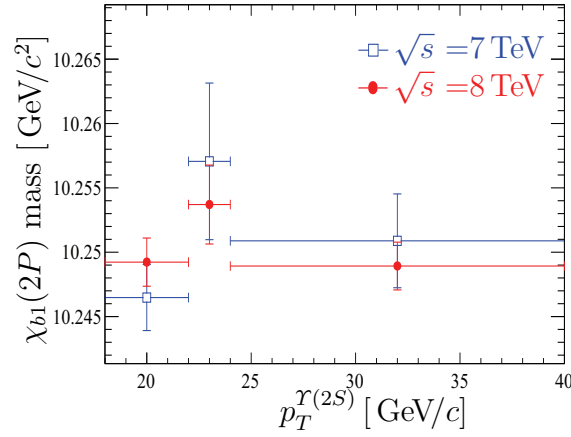


Figure 5.11: Distribution of the $\chi_{b1}(2P)$ mass in $\chi_b(2P) \rightarrow \Upsilon(2S)\gamma$ decay in specified $p_T^{\Upsilon(2S)}$ ranges.

Figure 5.12 shows the number of signal events as a function of $p_T^{\Upsilon(2S)}$. Table C.1 in Appendix summarizes the obtained results.

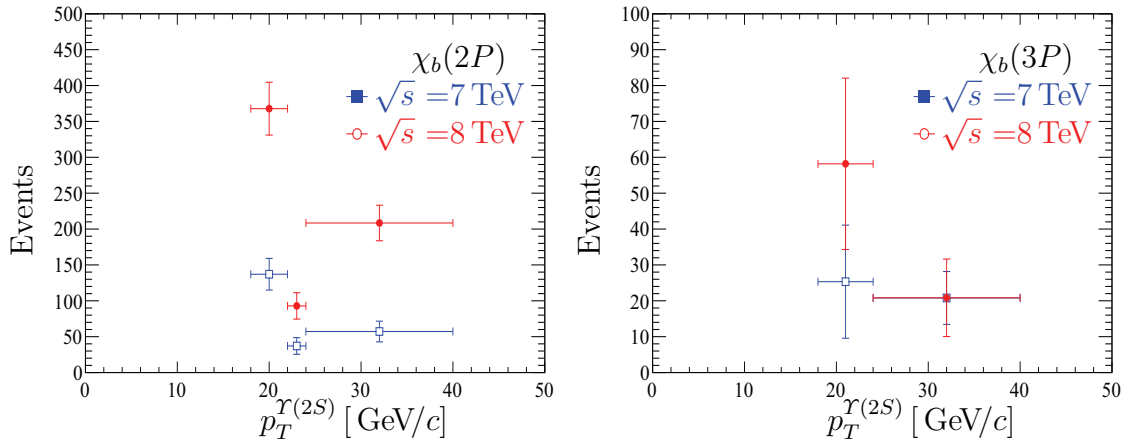


Figure 5.12: Distribution of χ_b yields in $\chi_b \rightarrow \Upsilon(2S)\gamma$ decay in specified $p_T^{\Upsilon(2S)}$ ranges.

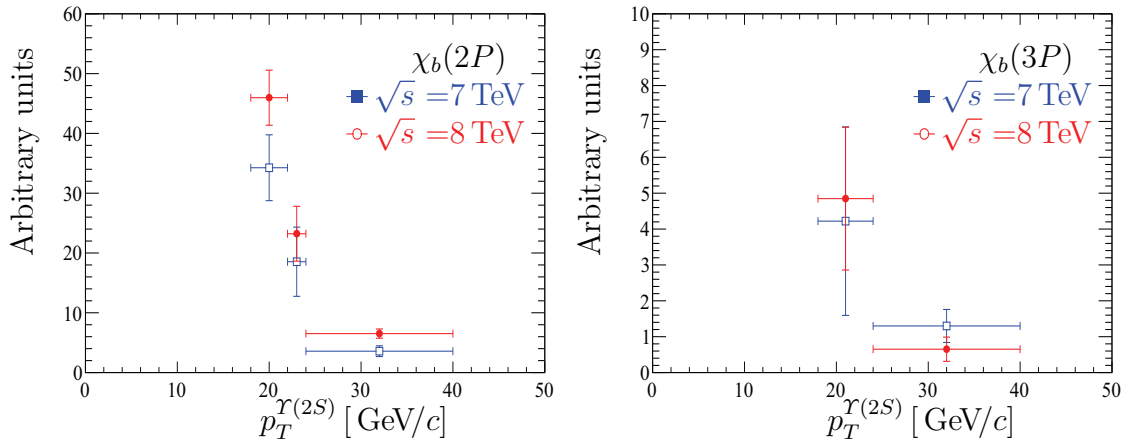


Figure 5.13: Distribution of χ_b yields in $\chi_b \rightarrow \Upsilon(2S)\gamma$ decay in specified $p_T^{\Upsilon(2S)}$ ranges. The distribution normalized by bin size and luminosity value.

Figure 5.13 shows the yields normalized by the bin size and the luminosity. Both $\chi_b(2P)$ and $\chi_b(3P)$ yields are smoothly decreasing functions of $p_T^{\Upsilon(2S)}$, as expected.

The dependence of the $\chi_{b1}(2P)$ fitted mass in bins of $p_T^{\Upsilon(2S)}$ is shown in Figure 5.11.

5.4.5 χ_b yields in $\chi_b \rightarrow \Upsilon(3S)\gamma$ decays

The fit was performed in the mass interval from 10.440 to 10.760 GeV/c^2 . The order of the background polynomial in Equation (5.3) is 2. Due to the large fluctuations in the background, the parameters of this component were fixed.

Figure 5.16 shows the mass distribution in the transverse momentum range $27 < p_T^{\Upsilon(3S)} < 40 \text{ GeV}/c$. Table 5.10 details the corresponding fit parameters.

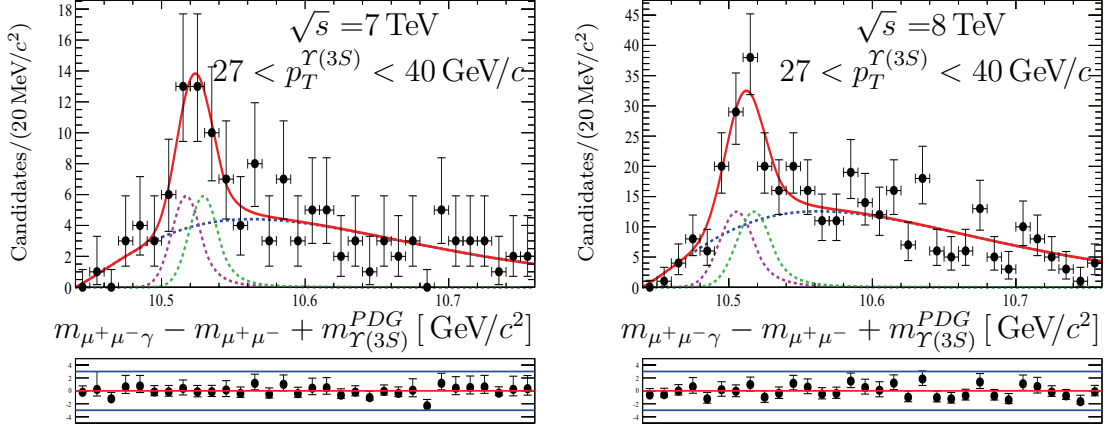


Figure 5.14: Distribution of the mass difference $m(\mu^+\mu^-\gamma) - m(\mu^+\mu^-)$ for selected χ_b ($3P$) candidates (black points) together with the result of the fit (solid red curve), including the background (dotted blue curve) and the signal (dashed green and magenta curves) contributions. Green dashed curve corresponds to χ_{b1} signal and magenta dashed curve to χ_{b2} signal. The bottom insert shows the pull distribution of the fit. The pull is defined as the difference between the data and fit value divided by the data error.

Table 5.10: Data fit parameters for $\chi_{b1,2}(3P) \rightarrow \Upsilon(3S)\gamma$ decays

	$\Upsilon(3S)$ transverse momentum intervals, GeV/ c	
	27 – 40	
	$\sqrt{s} = 7$ TeV	$\sqrt{s} = 8$ TeV
$N_{\chi_b(3P)}$	31 ± 12	72 ± 16
Background	97 ± 14	283 ± 21
$\mu_{\chi_{b1}(3P)}$, MeV/ c^2	$10,517 \pm 4$	$10,504.0 \pm 2.5$
$\sigma_{\chi_{b1}(3P)}$, MeV/ c^2	9 ± 6	8.3 ± 2.7
c_0	0.52 ± 0.18	0.52 ± 0.09
c_1	-0.42 ± 0.19	-0.36 ± 0.10
c_2	1.3 ± 0.8	-1.23 ± 0.18
$\chi^2/n.d.f$	0.38	1.09

A good resolution on the $\chi_{b1}(3P)$ mass is observed, so this decay can be used for $\chi_{b1}(3P)$ mass estimation. Figure 5.15 shows how the measured $\chi_{b1}(3P)$ mass depends on the $\chi_{b1}(3P)$ and $\chi_{b2}(3P)$ yields ratio (λ parameter), which is unknown (Section 5.5). The

$\chi_{b1}(3P)$ mass is measured to be $10,508 \pm 2$ (stat) ± 8 (syst) MeV/ c , where the combined 2011 and 2012 datasets are used, the central value has been obtained by setting $\lambda = 0.5$ in the fit and the systematic error takes into account the uncertainties on the λ parameter and the mass difference between $\chi_{b1}(3P)$ and $\chi_{b2}(3P)$. This result is in agreement with a recent unpublished LHCb study with converted photons, where the $\chi_{b1}(3P)$ mass is $10,510 \pm 3$ (stat) $_{-3.4}^{+4.4}$ (syst). This result is also compatible within $\sim 1.5\sigma$ with the $\chi_{b1,2}(3P)$ mass barycenter reported by ATLAS [10] ($10,530 \pm 5$ (stat) ± 17 (syst) MeV/ c^2) and D0 [11] ($10,551 \pm 14$ (syst) ± 17 (stat))

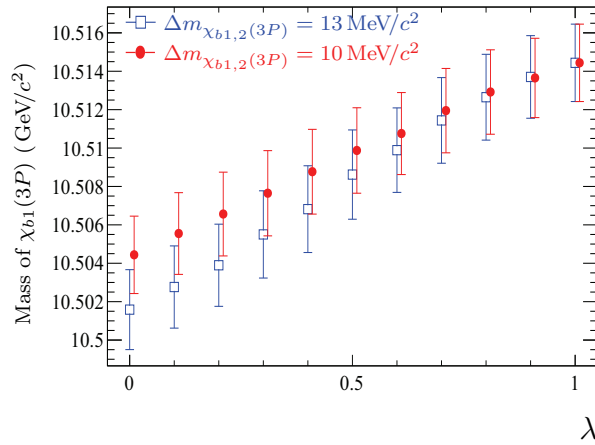


Figure 5.15: Distribution of the $\chi_{b1}(3P)$ mass in $\chi_b(3P) \rightarrow \Upsilon(3S)\gamma$ decay. The mass is measured with different ratios (λ) and mass difference ($\Delta m_{\chi_{b1,2}(3P)}$) between $\chi_{b1}(3P)$ and $\chi_{b2}(3P)$ states. The measurement is performed on the combined 2011 and 2012 datasets.

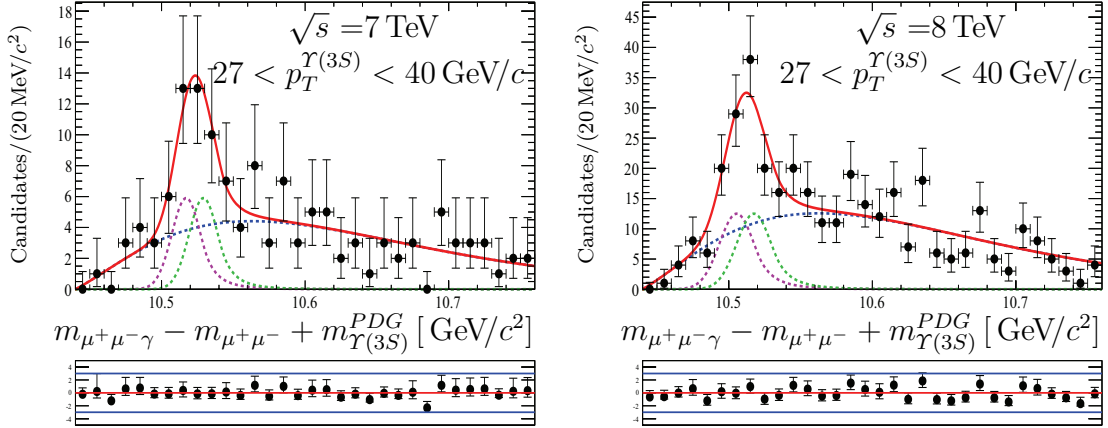


Figure 5.16: Distribution of the mass difference $m(\mu^+\mu^-\gamma) - m(\mu^+\mu^-)$ for selected χ_b (3P) candidates (black points) together with the result of the fit (solid red curve), including the background (dotted blue curve) and the signal (dashed green and magenta curves) contributions. Green dashed curve corresponds to χ_{b1} signal and magenta dashed curve to χ_{b2} signal. The bottom insert shows the pull distribution of the fit. The pull is defined as the difference between the data and fit value divided by the data error.

5.5 χ_{b1} and χ_{b2} yields ratio

The ratio between χ_{b2} and χ_{b1} candidates is one of the parameters in our fit model (Section 5.4.2). This ratio has been estimated in theoretical works [22]. Recent preliminary results were obtained at LHCb and CMS. The same unpublished LHCb study quoted in Section 5.4.5 obtains a good agreement with theory within errors, while CMS [44] gets a value of this ratio of 0.9, flat as function of p_T .

Chapter 2 shows that the theory predicts [22] the ratio χ_{c2}/χ_{c1} as a function of p_T , which is in agreement with experimental results (Figure 2.7). Since the result for the bottomonium ratio could be obtained by rescaling the charmonium curve, the χ_{b1} and χ_{b2} ratio can be measured by the following formula in specified transverse momentum intervals of Υ :

$$\frac{N_{\chi_{b2}}^{data}}{N_{\chi_{b1}}^{data}} = \frac{\sigma(\chi_{b2}) Br(\chi_{b2} \rightarrow \Upsilon\gamma) \varepsilon_{\chi_{b2}}^\gamma}{\sigma(\chi_{b1}) Br(\chi_{b1} \rightarrow \Upsilon\gamma) \varepsilon_{\chi_{b1}}^\gamma} \quad (5.8)$$

where $\sigma(\chi_{b2})/\sigma(\chi_{b1})$ is a ratio from [22], the branching fractions $Br(\chi_{b1,2} \rightarrow \Upsilon\gamma)$ are known experimentally (Table 5.11) and reconstruction efficiencies $\varepsilon_{\chi_{b1,2}}^\gamma$ are obtained in

this study (Tables E.1 to E.6).

Table 5.11: The branching fractions of radiative $\chi_b(1P)$ and $\chi_b(2P)$ mesons decays are known experimentally [45]

$$\begin{aligned} Br(\chi_{b1}(1P) \rightarrow \Upsilon(1S)\gamma) &= 33.9\% \pm 2.2\% \\ Br(\chi_{b2}(1P) \rightarrow \Upsilon(1S)\gamma) &= 19.1\% \pm 1.2\% \\ Br(\chi_{b1}(2P) \rightarrow \Upsilon(1S)\gamma) &= 9.2\% \pm 0.8\% \\ Br(\chi_{b2}(2P) \rightarrow \Upsilon(1S)\gamma) &= 7.0\% \pm 0.7\% \\ Br(\chi_{b1}(2P) \rightarrow \Upsilon(2S)\gamma) &= 19.9\% \pm 1.9\% \\ Br(\chi_{b2}(2P) \rightarrow \Upsilon(2S)\gamma) &= 10.6\% \pm 2.6\% \end{aligned}$$

The $N_{\chi_{b1}}^{data}/(N_{\chi_{b1}}^{data} + N_{\chi_{b2}}^{data})$ ratio is estimated by Equation (5.8) to be in the range between 0.4 and 0.7 for $\chi_b(1P)$ and $\chi_b(2P)$ decays. The ratio for $\chi_b(3P)$ decays could not be calculated because the branching fraction of these decays are unknown. In this study this ratio is fixed to 0.5 and systematic uncertainty is assigned to this decision.

5.6 Simulation

5.6.1 Data - simulation comparison

A comparison of the distribution of the relevant observables used in this analysis was performed on real and simulated data, in order to assess the reliability of Monte Carlo in computing efficiencies. It should be stressed that, since a relative branching fraction is measured, systematic effects cancel at first order. As expected, there are no much differences observed between the simulation distributions, since the generated $\chi_b(1P)$, $\chi_b(2P)$ and $\chi_b(3P)$ differ only by χ_b mass value.

Combinatorial background has been subtracted in real data by using the *sPlot* technique [46]. The resulting signal weights are used to obtain the signal distribution for each relevant variable.

In Figures 5.17 and 5.18 these distributions are shown for signals in $\chi_b \rightarrow \Upsilon(1S)\gamma$ decays compared with the corresponding simulated distributions.

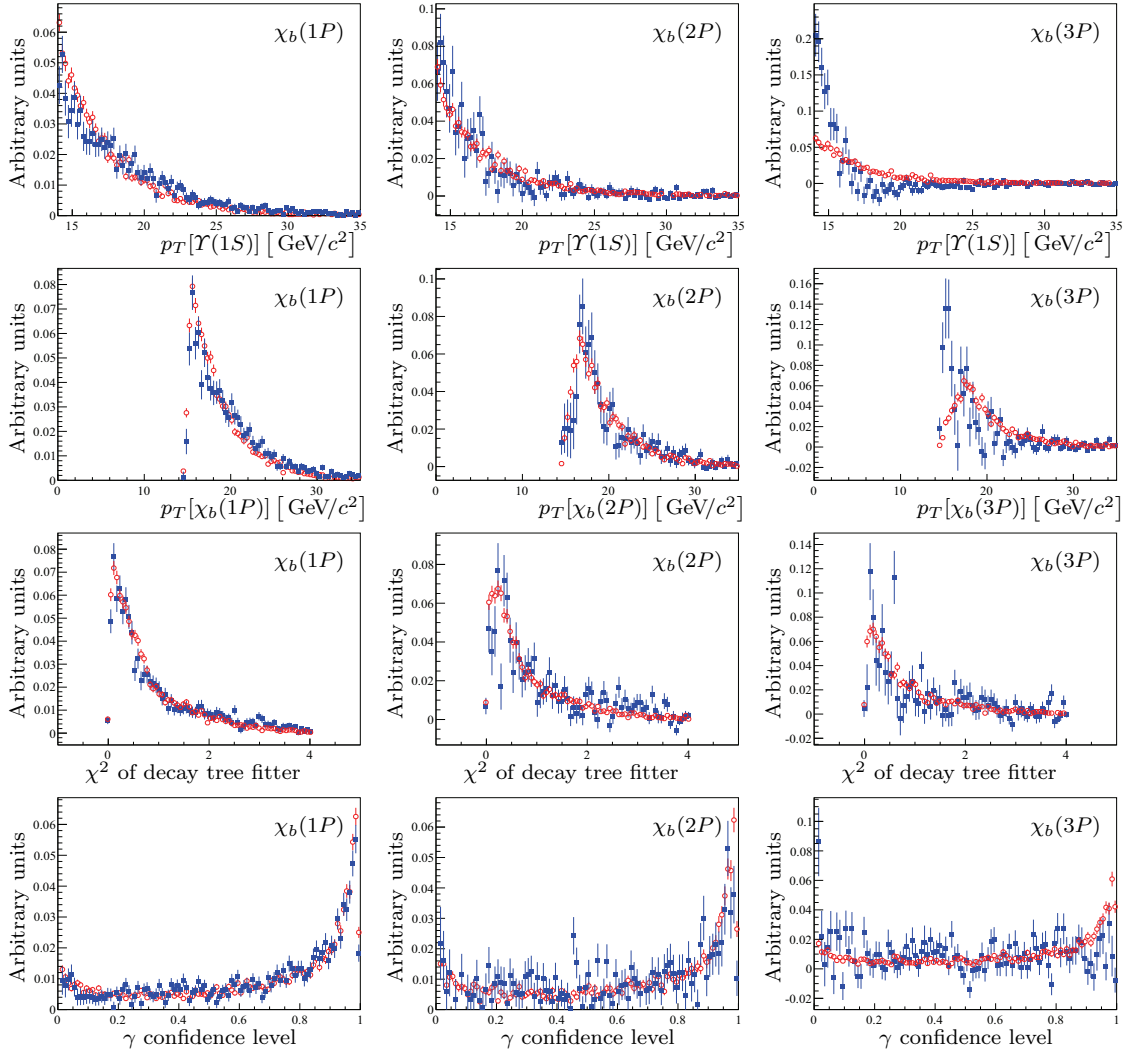


Figure 5.17: Data ($\sqrt{s} = 8$ TeV) — Monte Carlo values comparison. Square (blue) points with errors bars corresponds data values, open circle (red) points with errors bars corresponds to simulation values.

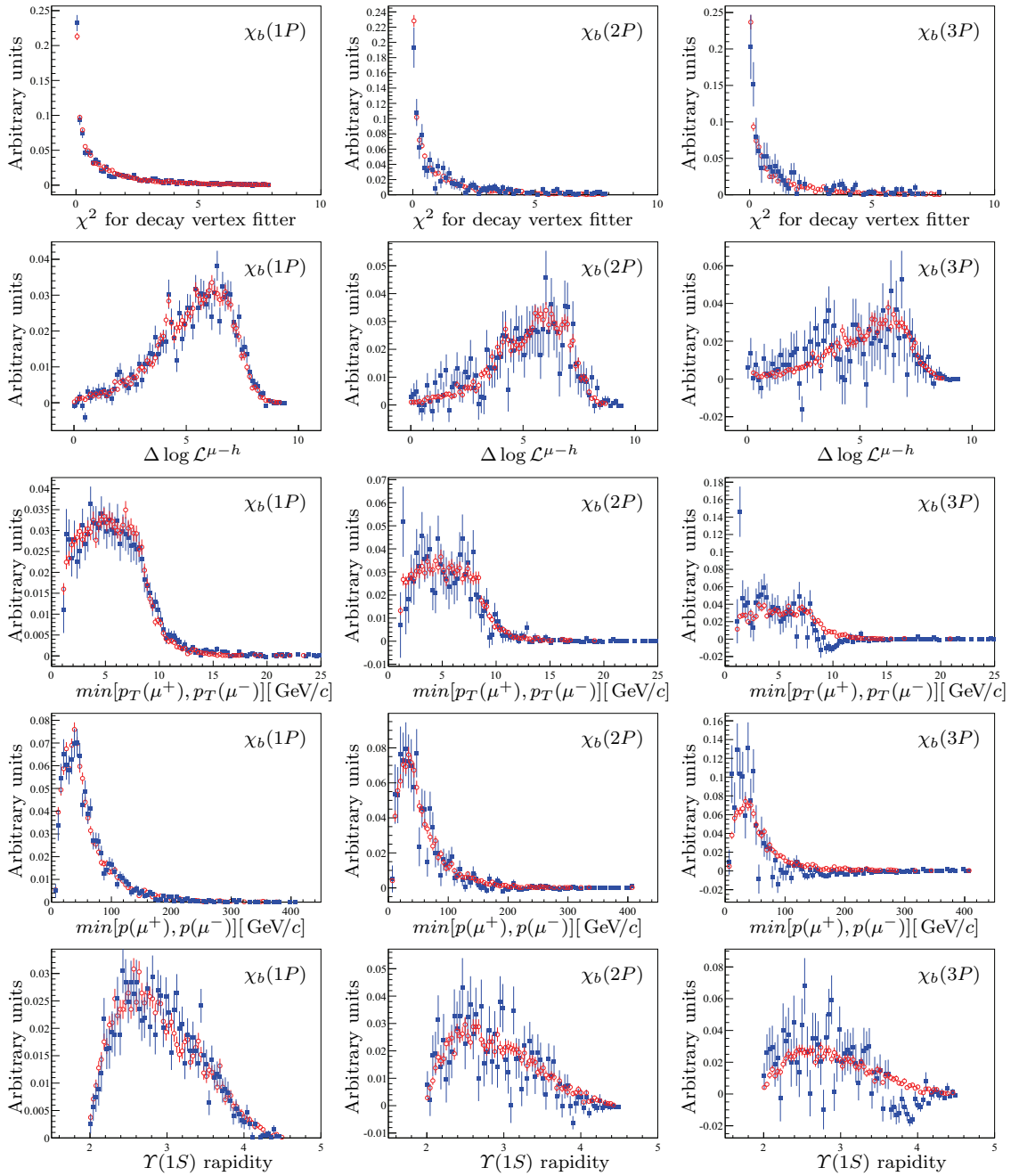


Figure 5.18: Data ($\sqrt{s} = 8$ TeV) — Monte Carlo values comparison. Square (blue) points with errors bars corresponds data values, open circle (red) points with errors bars corresponds to simulation values.

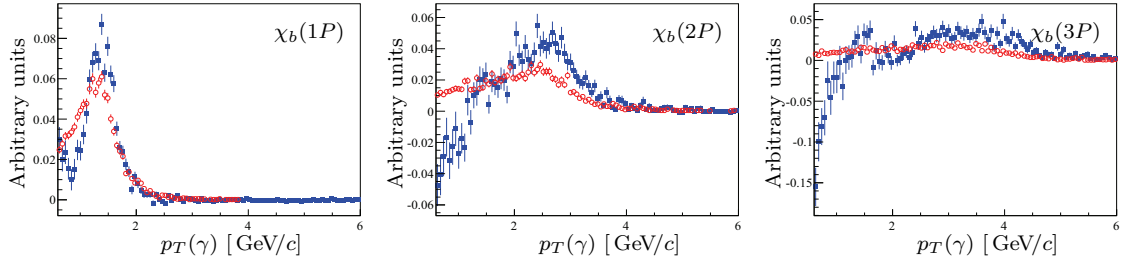


Figure 5.19: Data ($\sqrt{s} = 8 \text{ TeV}$) - Monte Carlo values comparison. Square (blue) points with errors bars corresponds data values, open circle (red) points with errors bars corresponds to simulation values.

The agreement is generally very good except for the distribution of photon transverse momentum (Figure 5.19). This is due to the *sPlot* technique, when applied on variables that affect the background shape. In our study the background in the fit of the invariant mass distribution depends on the photon transverse momentum, hence a mismatch between data and simulation is expected. Other discrepancies observed in the distributions for $\chi_b(3P)$ decays are possibly due a poor signal to background ratio, which translates into large systematic uncertainties in the *sWeights*.

5.6.2 Selection efficiencies

The distributions of the invariant mass difference of truth-matched MC events in the χ_b simulation are shown in Figure 5.20. The flat left tails are due to photons which, although being correctly associated to the χ_b decay, are poorly reconstructed in the calorimeter (due to e.g. cracks, spillover, cross-talk, etc.). In principle, these tails could be modeled in our fit to signal, but in practice they will not be distinguishable from background. Therefore, the number of χ_b events for efficiency calculations is not determined by simple event counting but from a fit where the tails are considered as background. In this fit the signal is described by a CrystalBall function and the background is a product of first order polynomial and exponential functions. The number of Υ events is obtained by counting all matched MC-true Υ events.

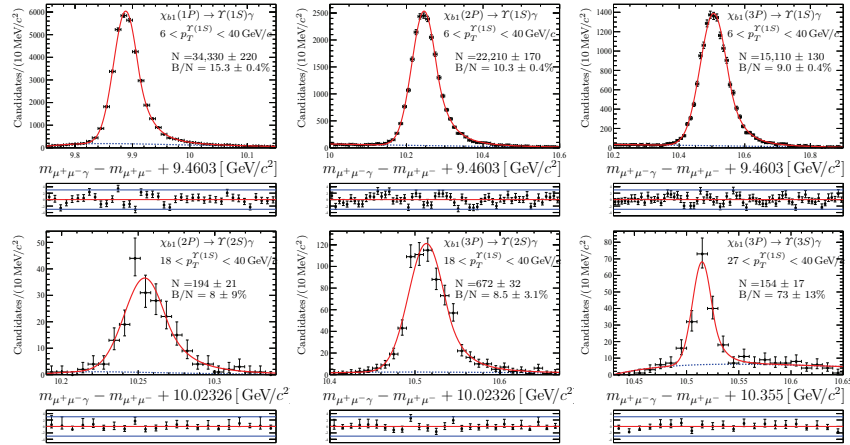
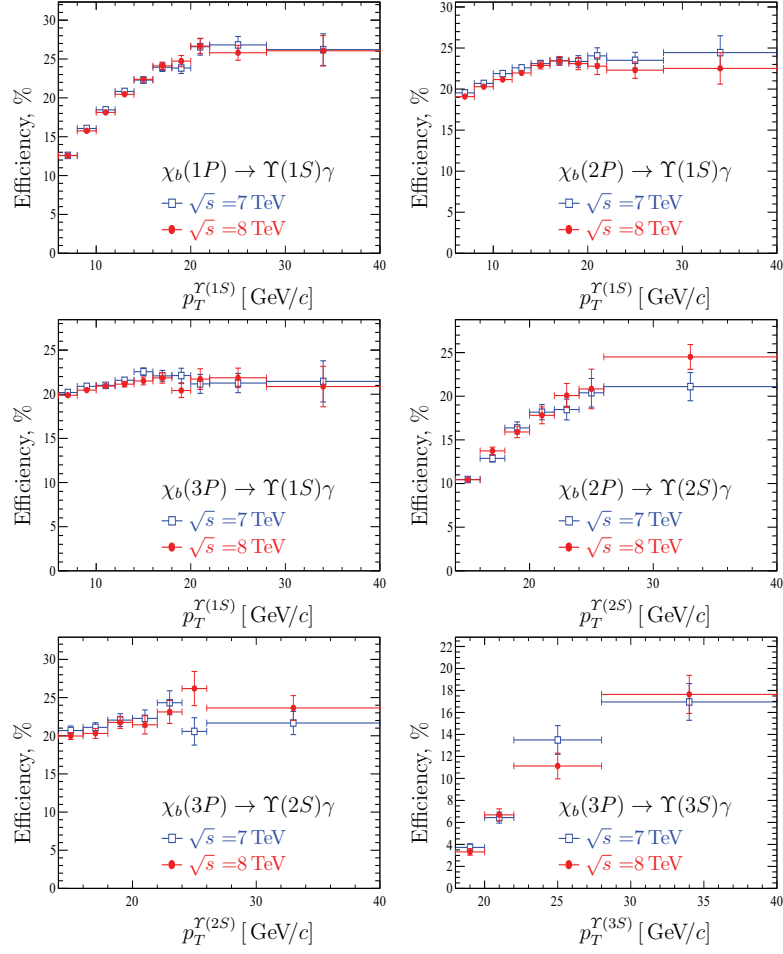


Figure 5.20: Distribution of the mass difference $\mu^+\mu^-\gamma - \mu^+\mu^-$ for matched $\chi_{b1}(1, 2, 3P)$ candidates in $\chi_b \rightarrow \Upsilon\gamma$ decays (black points) together with the result of the fit (solid red curve), including background (dotted blue curve) contribution. The pull is defined as the difference between the data and fit value divided by the data error.

Figure 5.21 shows the measured efficiency of χ_b reconstruction. More details on these measurements are shown in Tables E.1 to E.6 in Appendix.

Figure 5.21: Photon reconstruction efficiency in χ_b decays as function of p_T^Υ

5.7 Υ fractions in $\chi_b \rightarrow \Upsilon\gamma$ decays

Figure 5.22 shows the measured fractions of Υ originating from χ_b decays for different p_T^Υ bins, assuming the production of unpolarized Υ and χ_b mesons. The uncertainties are statistical only. The obtained $\Upsilon(1S)$ fractions are consistent with the previous LHCb result [13]. In $\chi_b \rightarrow \Upsilon(1S)\gamma$ decays, a smoothly increasing trend is visible as a function of the Υ transverse momentum. The limited statistics for the other decay does not allow to draw a similar conclusion for them. Roughly speaking, about 40% of Υ mesons produced

at the LHCb in the LHCb acceptance originate from χ_b decays.

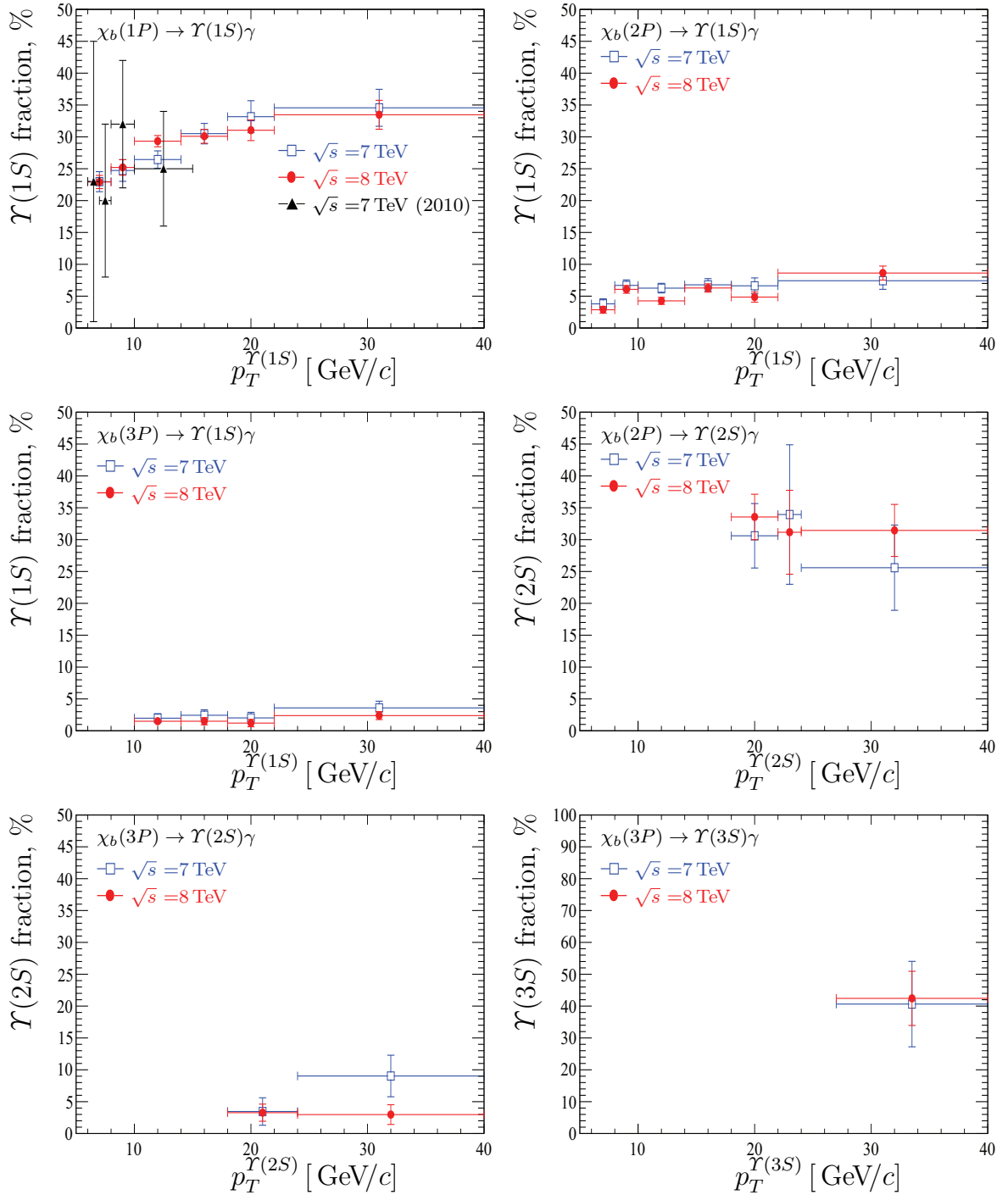


Figure 5.22: Fraction of Υ mesons originated from χ_b decays (statistical errors only)

Tables 5.12 to 5.14 provide the summary of obtained yields, efficiency and fractions.

Table 5.12: Summary of $\Upsilon(1S)$ fraction determination originating from χ_b decay

(a) $6 < p_T^{\Upsilon(1S)} < 14 \text{ GeV}/c$

	$\Upsilon(1S)$ transverse momentum intervals, GeV/c					
	6 – 8		8 – 10		10 – 14	
	$\sqrt{s} = 7 \text{ TeV}$	$\sqrt{s} = 8 \text{ TeV}$	$\sqrt{s} = 7 \text{ TeV}$	$\sqrt{s} = 8 \text{ TeV}$	$\sqrt{s} = 7 \text{ TeV}$	$\sqrt{s} = 8 \text{ TeV}$
$N_{\chi_b(1P)}$	3590 ± 240	8100 ± 400	2800 ± 190	6520 ± 310	3140 ± 160	7970 ± 230
$N_{\chi_b(2P)}$	920 ± 190	1540 ± 290	980 ± 130	2020 ± 200	840 ± 100	1310 ± 170
$N_{\chi_b(3P)}$	—	—	—	—	250 ± 90	450 ± 150
$N_{\Upsilon(1S)}$	$124,100 \pm 400$	$282,600 \pm 600$	$70,480 \pm 290$	$164,300 \pm 500$	$60,780 \pm 270$	$143,700 \pm 400$
$\epsilon_{\chi_b(1P) \rightarrow \Upsilon(1S)\gamma}^\gamma, \%$	12.60 ± 0.07	12.57 ± 0.07	16.06 ± 0.11	15.75 ± 0.10	19.51 ± 0.13	18.92 ± 0.13
$\epsilon_{\chi_b(2P) \rightarrow \Upsilon(1S)\gamma}^\gamma, \%$	19.54 ± 0.09	19.08 ± 0.10	20.69 ± 0.12	20.29 ± 0.13	22.13 ± 0.14	21.40 ± 0.16
$\epsilon_{\chi_b(3P) \rightarrow \Upsilon(1S)\gamma}^\gamma, \%$	20.19 ± 0.11	19.88 ± 0.12	20.89 ± 0.14	20.46 ± 0.15	21.18 ± 0.17	21.02 ± 0.18
Fraction $\chi_b(1P), \%$	23.0 ± 1.6	22.9 ± 1.0	24.7 ± 1.7	25.2 ± 1.2	26.4 ± 1.4	29.3 ± 0.9
Fraction $\chi_b(2P), \%$	3.8 ± 0.8	2.9 ± 0.5	6.7 ± 0.9	6.1 ± 0.6	6.3 ± 0.8	4.3 ± 0.6
Fraction $\chi_b(3P), \%$	—	—	—	—	2.0 ± 0.7	1.5 ± 0.5

(b) $14 < p_T^{\Upsilon(1S)} < 40 \text{ GeV}/c$

	$\Upsilon(1S)$ transverse momentum intervals, GeV/c					
	14 – 18		18 – 22		22 – 40	
	$\sqrt{s} = 7 \text{ TeV}$	$\sqrt{s} = 8 \text{ TeV}$	$\sqrt{s} = 7 \text{ TeV}$	$\sqrt{s} = 8 \text{ TeV}$	$\sqrt{s} = 7 \text{ TeV}$	$\sqrt{s} = 8 \text{ TeV}$
$N_{\chi_b(1P)}$	1280 ± 60	3120 ± 110	489 ± 34	1220 ± 60	341 ± 25	800 ± 50
$N_{\chi_b(2P)}$	290 ± 40	650 ± 70	93 ± 17	174 ± 28	65 ± 12	179 ± 21
$N_{\chi_b(3P)}$	101 ± 35	150 ± 60	26 ± 11	39 ± 19	28 ± 8	48 ± 12
$N_{\Upsilon(1S)}$	$18,520 \pm 150$	$45,160 \pm 230$	5960 ± 90	$15,600 \pm 140$	3690 ± 70	9270 ± 110
$\epsilon_{\chi_b(1P) \rightarrow \Upsilon(1S)\gamma}^\gamma, \%$	22.70 ± 0.31	22.99 ± 0.28	24.7 ± 0.6	25.2 ± 0.6	26.7 ± 1.0	25.9 ± 0.9
$\epsilon_{\chi_b(2P) \rightarrow \Upsilon(1S)\gamma}^\gamma, \%$	23.26 ± 0.29	23.04 ± 0.32	23.6 ± 0.6	23.0 ± 0.6	23.9 ± 0.9	22.3 ± 0.9
$\epsilon_{\chi_b(3P) \rightarrow \Upsilon(1S)\gamma}^\gamma, \%$	22.4 ± 0.4	21.6 ± 0.4	21.8 ± 0.7	20.8 ± 0.7	21.2 ± 1.0	21.6 ± 1.0
Fraction $\chi_b(1P), \%$	30.5 ± 1.6	30.1 ± 1.1	33.2 ± 2.5	31.0 ± 1.6	34.6 ± 2.9	33.5 ± 2.3
Fraction $\chi_b(2P), \%$	6.8 ± 1.0	6.3 ± 0.7	6.6 ± 1.2	4.9 ± 0.8	7.4 ± 1.3	8.6 ± 1.1
Fraction $\chi_b(3P), \%$	2.4 ± 0.9	1.5 ± 0.6	2.0 ± 0.9	1.2 ± 0.6	3.6 ± 1.1	2.4 ± 0.6

Table 5.13: Summary of $\Upsilon(2S)$ fraction determination originating from χ_b decay

	$\Upsilon(2S)$ transverse momentum intervals, GeV/c							
	18 – 22		18 – 24		22 – 24		24 – 40	
	$\sqrt{s} = 7 \text{ TeV}$	$\sqrt{s} = 8 \text{ TeV}$	$\sqrt{s} = 7 \text{ TeV}$	$\sqrt{s} = 8 \text{ TeV}$	$\sqrt{s} = 7 \text{ TeV}$	$\sqrt{s} = 8 \text{ TeV}$	$\sqrt{s} = 7 \text{ TeV}$	$\sqrt{s} = 8 \text{ TeV}$
$N_{\chi_b(2P)}$	137 ± 22	370 ± 40	169 ± 27	450 ± 40	37 ± 12	93 ± 18	57 ± 14	208 ± 25
$N_{\chi_b(3P)}$	12 ± 14	35 ± 24	25 ± 16	58 ± 24	12 ± 6	19 ± 12	21 ± 7	21 ± 11
$N_{\Upsilon(2S)}$	2670 ± 60	6620 ± 100	3260 ± 70	8110 ± 110	591 ± 29	1480 ± 50	1090 ± 40	2860 ± 70
$\epsilon_{\chi_b(2P) \rightarrow \Upsilon(2S)\gamma}^\gamma, \%$	16.8 ± 0.5	16.6 ± 0.5	17.1 ± 0.5	17.1 ± 0.5	18.5 ± 1.2	20.1 ± 1.4	20.6 ± 1.2	23.2 ± 1.1
$\epsilon_{\chi_b(3P) \rightarrow \Upsilon(2S)\gamma}^\gamma, \%$	22.1 ± 0.6	21.7 ± 0.6	22.5 ± 0.6	21.9 ± 0.6	24.3 ± 1.6	23.1 ± 1.5	21.2 ± 1.2	24.5 ± 1.3
Fraction $\chi_b(2P), \%$	31 ± 5	34 ± 4	30 ± 5	32.4 ± 3.0	34 ± 11	31 ± 7	26 ± 7	31 ± 4
Fraction $\chi_b(3P), \%$	2.0 ± 2.4	2.5 ± 1.6	3.5 ± 2.2	3.3 ± 1.3	8 ± 5	5.6 ± 3.4	9.0 ± 3.3	3.0 ± 1.6

Table 5.14: Summary of $\Upsilon(3S)$ fraction determination originating from χ_b decay

	$\Upsilon(3S)$ transverse momentum intervals, GeV/ c 27 – 40	
	$\sqrt{s} = 7$ TeV	$\sqrt{s} = 8$ TeV
$N_{\chi_b(3P)}$	27 ± 8	84 ± 15
$N_{\Upsilon(3S)}$	396 ± 26	1180 ± 50
$\varepsilon_{\chi_b(3P) \rightarrow \Upsilon(3S)\gamma}^\gamma, \%$	16.8 ± 1.4	16.8 ± 1.5
Fraction $\chi_b(3P), \%$	41 ± 13	42 ± 9

5.8 Systematic Uncertainties

Since this analysis measures the fraction of $\Upsilon(nS)$ particles originating from χ_b decays, most systematic uncertainties cancel in the ratio and only residual effects need to be taken into account. Systematic uncertainties can be grouped according to their contribution to the terms of Equation (5.1). Systematic uncertainties on the event yields are mostly due to models used to fit the Υ and χ_b invariant masses, while the ones on the efficiency are due to the photon reconstruction and the unknown initial polarization of χ_b and Υ particles. The systematic uncertainties due to polarization of inclusive Υ mesons are considered to be small [41, 47].

5.8.1 Uncertainties related to the fit model

The uncertainty related to the modeling of the Υ invariant mass distribution has been estimated by following previous studies [41]. An uncertainty of 0.7% has been assigned to the yields of $\Upsilon(nS)$ mesons.

In the fit model of the χ_b invariant masses, several sources need to be taken into account. Firstly, the relative proportion of spin-1 and spin-2 states, which is kept fixed in the fit to values close to 0.5, predicted by theory, is varied from 0.3 to 0.7 as it was discussed in Section 5.5.

Tables 5.16, 5.19 and 5.22 report the relative variation in percent of the χ_b yields as function of λ , the relative proportion of the two χ_b states, for all examined decays, in each bin of transverse momentum for χ_b decays into $\Upsilon(1S)$, $\Upsilon(2S)$ and $\Upsilon(3S)$, respectively. We take as systematic error in each p_T bin the maximum deviation of the χ_b yields with respect to the nominal fit.

Another source of systematic uncertainty is due to the variation of the χ_b masses as function of $p_T(\Upsilon)$, observed in Section 5.4. We repeat the fits by taking the minimum and maximum values of the χ_b masses and take the maximum difference in the yields as systematic uncertainty. The resulting uncertainties are reported in Tables 5.17, 5.20 and 5.23 for χ_b decays into $\Upsilon(1S)$, $\Upsilon(2S)$ and $\Upsilon(3S)$, respectively.

Systematic uncertainties due to parameters taken from PDG (e.g. mass differences) are negligible.

Uncertainties related to Data-MonteCarlo differences in invariant mass resolution

In the χ_b fits, the resolution of the CrystalBall functions, determined from simulation, has been scaled by a factor 1.17 in order to account for data — MonteCarlo differences. This factor was obtained by fitting a histogram, that stores the ratio between data and MonteCarlo resolution, by a constant function. The result of fit is shown in Figure 5.23.

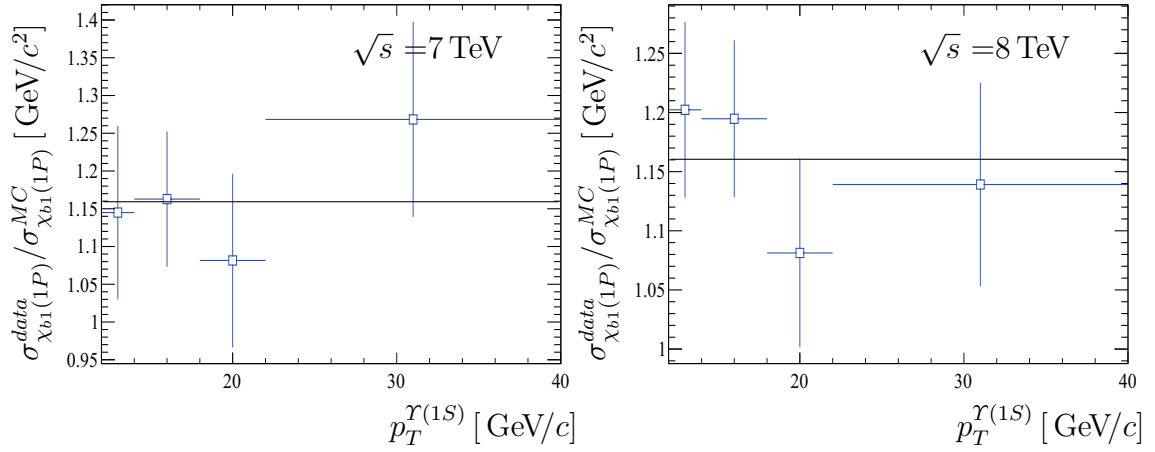


Figure 5.23: Ratio between $\chi_{b1}(1P)$ yield resolution in data and $\chi_{b1}(1P)$ yield resolution in MonteCarlo in $\chi_{b1}(1P) \rightarrow \Upsilon(1S)\gamma$ decay. The black line on the plot shows the result of the histogram fit by the constant function.

We estimate the systematic uncertainty due to this assumption by repeating the fits by changing the σ parameter within the maximum and minimum values of the scaling factor obtained from the fit in Figure 5.23. Results are shown in Table 5.15.

Table 5.15: χ_b yields systematic uncertainties (%) related to the Data-MonteCarlo resolution difference in the fit model for $\chi_b(1, 2, 3P) \rightarrow \Upsilon(1S)\gamma$ decays

(a) $6 < p_T^{\Upsilon(1S)} < 10 \text{ GeV}/c$

		$\Upsilon(1S)$ transverse momentum intervals, GeV/c											
		6 – 8						8 – 10					
		$\sqrt{s} = 7 \text{ TeV}$			$\sqrt{s} = 8 \text{ TeV}$			$\sqrt{s} = 7 \text{ TeV}$			$\sqrt{s} = 8 \text{ TeV}$		
		$N_{\chi_b(1P)}$	$N_{\chi_b(2P)}$	$N_{\chi_b(3P)}$	$N_{\chi_b(1P)}$	$N_{\chi_b(2P)}$	$N_{\chi_b(3P)}$	$N_{\chi_b(1P)}$	$N_{\chi_b(2P)}$	$N_{\chi_b(3P)}$	$N_{\chi_b(1P)}$	$N_{\chi_b(2P)}$	$N_{\chi_b(3P)}$
$\frac{\sigma_{\chi_b(1P)}^{data}}{\sigma_{\chi_b(1P)}^{MC}} = 1.13$	2.7	1.2	—	2.6	0.5	—	2.4	1.3	—	2.5	1.5	—	
$\frac{\sigma_{\chi_b(1P)}^{data}}{\sigma_{\chi_b(1P)}^{MC}} = 1.20$	-3.8	-0.6	—	-3.7	1.3	—	-3.3	-1.5	—	-3.3	-1.8	—	

(b) $10 < p_T^{\Upsilon(1S)} < 18 \text{ GeV}/c$

		$\Upsilon(1S)$ transverse momentum intervals, GeV/c											
		10 – 14						14 – 18					
		$\sqrt{s} = 7 \text{ TeV}$			$\sqrt{s} = 8 \text{ TeV}$			$\sqrt{s} = 7 \text{ TeV}$			$\sqrt{s} = 8 \text{ TeV}$		
		$N_{\chi_b(1P)}$	$N_{\chi_b(2P)}$	$N_{\chi_b(3P)}$	$N_{\chi_b(1P)}$	$N_{\chi_b(2P)}$	$N_{\chi_b(3P)}$	$N_{\chi_b(1P)}$	$N_{\chi_b(2P)}$	$N_{\chi_b(3P)}$	$N_{\chi_b(1P)}$	$N_{\chi_b(2P)}$	$N_{\chi_b(3P)}$
$\frac{\sigma_{\chi_b(1P)}^{data}}{\sigma_{\chi_b(1P)}^{MC}} = 1.13$	2.2	1.8	4.3	2.2	1.5	6.0	1.4	2.6	1.8	1.5	2.0	2.9	
$\frac{\sigma_{\chi_b(1P)}^{data}}{\sigma_{\chi_b(1P)}^{MC}} = 1.20$	-2.9	-2.4	-5.7	-3.1	-1.2	-11.1	-1.8	-3.3	-2.3	-1.9	-2.7	-3.7	

(c) $18 < p_T^{\Upsilon(1S)} < 40 \text{ GeV}/c$

		$\Upsilon(1S)$ transverse momentum intervals, GeV/c											
		18 – 22						22 – 40					
		$\sqrt{s} = 7 \text{ TeV}$			$\sqrt{s} = 8 \text{ TeV}$			$\sqrt{s} = 7 \text{ TeV}$			$\sqrt{s} = 8 \text{ TeV}$		
		$N_{\chi_b(1P)}$	$N_{\chi_b(2P)}$	$N_{\chi_b(3P)}$	$N_{\chi_b(1P)}$	$N_{\chi_b(2P)}$	$N_{\chi_b(3P)}$	$N_{\chi_b(1P)}$	$N_{\chi_b(2P)}$	$N_{\chi_b(3P)}$	$N_{\chi_b(1P)}$	$N_{\chi_b(2P)}$	$N_{\chi_b(3P)}$
$\frac{\sigma_{\chi_b(1P)}^{data}}{\sigma_{\chi_b(1P)}^{MC}} = 1.13$	1.2	1.6	1.7	1.2	1.7	3.0	0.9	3.7	5.6	1.3	1.1	2.3	
$\frac{\sigma_{\chi_b(1P)}^{data}}{\sigma_{\chi_b(1P)}^{MC}} = 1.20$	-1.6	-2.1	-2.3	-1.6	-2.3	-3.4	-1.7	-1.4	-0.7	-1.8	-1.5	-3.2	

Table 5.16: χ_b yields systematic uncertainties (%) related to λ values in the fit model for $\chi_b(1, 2, 3P) \rightarrow \Upsilon(1S)\gamma$ decays

(a) $6 < p_T^{\Upsilon(1S)} < 10 \text{ GeV}/c$

	$\Upsilon(1S)$ transverse momentum intervals, GeV/c											
	6 – 8						8 – 10					
	$\sqrt{s} = 7 \text{ TeV}$			$\sqrt{s} = 8 \text{ TeV}$			$\sqrt{s} = 7 \text{ TeV}$			$\sqrt{s} = 8 \text{ TeV}$		
	$N_{\chi_b(1P)}$	$N_{\chi_b(2P)}$	$N_{\chi_b(3P)}$	$N_{\chi_b(1P)}$	$N_{\chi_b(2P)}$	$N_{\chi_b(3P)}$	$N_{\chi_b(1P)}$	$N_{\chi_b(2P)}$	$N_{\chi_b(3P)}$	$N_{\chi_b(1P)}$	$N_{\chi_b(2P)}$	$N_{\chi_b(3P)}$
$\lambda = 0.0$	13.3	-8.3	—	10.1	-12.9	—	19.3	-8.7	—	15.9	-7.3	—
$\lambda = 0.1$	9.0	-6.7	—	6.1	-8.9	—	13.9	-7.0	—	11.1	-5.9	—
$\lambda = 0.2$	5.4	-5.2	—	2.9	-5.4	—	9.1	-5.2	—	6.9	-4.2	—
$\lambda = 0.3$	2.5	-3.4	—	0.8	-3.9	—	4.9	-3.2	—	3.6	-2.6	—
$\lambda = 0.4$	0.7	-1.6	—	-0.3	-1.5	—	1.9	-1.5	—	1.2	-1.1	—
$\lambda = 0.5$	0.0	0.0	—	0.0	0.0	—	0.0	0.0	—	0.0	0.0	—
$\lambda = 0.6$	0.8	1.5	—	1.3	0.7	—	-0.7	1.2	—	0.1	0.8	—
$\lambda = 0.7$	2.7	1.6	—	4.1	-2.2	—	-0.1	1.9	—	1.4	1.0	—
$\lambda = 0.8$	6.1	0.8	—	7.1	-8.3	—	1.6	2.2	—	3.7	0.9	—
$\lambda = 0.9$	9.4	-1.3	—	10.9	-17.2	—	4.3	2.0	—	7.1	0.5	—
$\lambda = 1.0$	13.9	-5.8	—	14.7	-24.4	—	7.9	1.7	—	11.2	-0.4	—

(b) $10 < p_T^{\Upsilon(1S)} < 18 \text{ GeV}/c$

	$\Upsilon(1S)$ transverse momentum intervals, GeV/c											
	10 – 14						14 – 18					
	$\sqrt{s} = 7 \text{ TeV}$			$\sqrt{s} = 8 \text{ TeV}$			$\sqrt{s} = 7 \text{ TeV}$			$\sqrt{s} = 8 \text{ TeV}$		
	$N_{\chi_b(1P)}$	$N_{\chi_b(2P)}$	$N_{\chi_b(3P)}$	$N_{\chi_b(1P)}$	$N_{\chi_b(2P)}$	$N_{\chi_b(3P)}$	$N_{\chi_b(1P)}$	$N_{\chi_b(2P)}$	$N_{\chi_b(3P)}$	$N_{\chi_b(1P)}$	$N_{\chi_b(2P)}$	$N_{\chi_b(3P)}$
$\lambda = 0.0$	15.8	-3.1	36.1	13.7	-13.6	36.2	6.8	-0.9	5.3	7.3	-2.0	-9.5
$\lambda = 0.1$	10.7	-2.6	25.9	5.5	-7.0	-0.6	4.2	-1.0	5.5	4.7	-1.9	-5.7
$\lambda = 0.2$	6.3	-1.7	16.6	5.2	-6.3	16.8	2.2	-1.0	5.1	2.5	-1.6	-3.1
$\lambda = 0.3$	3.0	-0.9	9.0	2.6	-3.4	9.3	0.9	-0.9	3.9	1.1	-1.2	-1.2
$\lambda = 0.4$	0.9	-0.2	3.6	0.2	-0.9	0.9	0.1	-0.5	2.1	0.2	-0.6	-0.0
$\lambda = 0.5$	0.0	0.0	0.0	0.0	0.0	0.0	0.0	0.0	0.0	0.0	0.0	0.0
$\lambda = 0.6$	0.4	-0.2	-2.1	0.6	0.6	-1.5	0.7	0.3	-6.2	0.5	0.9	-0.7
$\lambda = 0.7$	1.9	-1.0	-2.9	2.5	0.3	1.4	1.6	2.2	-4.8	1.6	2.0	-1.8
$\lambda = 0.8$	4.4	-2.0	-3.0	4.1	-0.2	-4.8	3.1	4.4	-3.5	3.2	3.4	-3.4
$\lambda = 0.9$	7.8	-3.3	-1.8	9.0	-1.6	7.5	5.4	5.7	-9.6	5.5	5.2	-4.7
$\lambda = 1.0$	12.0	-4.8	0.4	13.3	-3.1	9.4	8.1	8.1	-11.4	8.3	7.3	-5.9

(c) $18 < p_T^{\Upsilon(1S)} < 40 \text{ GeV}/c$

	$\Upsilon(1S)$ transverse momentum intervals, GeV/c											
	18 – 22						22 – 40					
	$\sqrt{s} = 7 \text{ TeV}$			$\sqrt{s} = 8 \text{ TeV}$			$\sqrt{s} = 7 \text{ TeV}$			$\sqrt{s} = 8 \text{ TeV}$		
	$N_{\chi_b(1P)}$	$N_{\chi_b(2P)}$	$N_{\chi_b(3P)}$	$N_{\chi_b(1P)}$	$N_{\chi_b(2P)}$	$N_{\chi_b(3P)}$	$N_{\chi_b(1P)}$	$N_{\chi_b(2P)}$	$N_{\chi_b(3P)}$	$N_{\chi_b(1P)}$	$N_{\chi_b(2P)}$	$N_{\chi_b(3P)}$
$\lambda = 0.0$	6.9	-0.6	-12.9	5.4	-3.3	-1.9	3.9	-0.1	0.1	3.2	-4.9	-8.4
$\lambda = 0.1$	4.2	-0.9	-9.7	3.0	-3.0	0.0	1.8	-0.3	0.9	0.9	-3.5	-6.0
$\lambda = 0.2$	2.2	-1.0	-6.9	1.2	-2.5	1.1	0.4	-0.2	1.6	-0.6	-2.2	-4.0
$\lambda = 0.3$	0.8	-0.9	-4.3	0.1	-1.8	1.5	-0.4	0.2	2.1	-1.3	-1.1	-2.4
$\lambda = 0.4$	0.0	-0.5	-2.1	-0.3	-1.0	1.2	-0.6	0.8	2.6	-1.1	-0.4	-1.0
$\lambda = 0.5$	0.0	0.0	0.0	0.0	0.0	0.0	0.0	0.0	0.0	0.0	0.0	0.0
$\lambda = 0.6$	0.6	0.8	2.2	0.9	1.3	-1.3	0.6	2.6	3.3	1.9	0.1	0.5
$\lambda = 0.7$	1.8	1.8	3.9	2.4	3.0	-2.7	1.9	4.0	3.8	4.3	0.2	0.6
$\lambda = 0.8$	3.8	3.1	5.8	4.5	5.4	-3.5	3.8	5.8	4.3	7.2	0.8	0.4
$\lambda = 0.9$	6.3	4.9	8.5	7.2	8.0	-4.5	6.3	7.9	5.1	10.5	1.9	0.6
$\lambda = 1.0$	9.5	6.5	9.5	10.5	11.0	-5.3	9.4	10.4	6.1	14.3	3.8	1.3

Table 5.17: χ_b yields systematic uncertainties (%) related to $\chi_{b1}(1P)$ mass uncertainty in the fit model for $\chi_b(1, 2, 3P) \rightarrow \Upsilon(1S)\gamma$ decays

(a) $6 < p_T^{\Upsilon(1S)} < 10 \text{ GeV}/c$												
$\Upsilon(1S)$ transverse momentum intervals, GeV/c												
6 - 8						8 - 10						
$\sqrt{s} = 7 \text{ TeV}$			$\sqrt{s} = 8 \text{ TeV}$			$\sqrt{s} = 7 \text{ TeV}$			$\sqrt{s} = 8 \text{ TeV}$			
$N_{\chi_b(1P)}$	$N_{\chi_b(2P)}$	$N_{\chi_b(3P)}$	$N_{\chi_b(1P)}$	$N_{\chi_b(2P)}$	$N_{\chi_b(3P)}$	$N_{\chi_b(1P)}$	$N_{\chi_b(2P)}$	$N_{\chi_b(3P)}$	$N_{\chi_b(1P)}$	$N_{\chi_b(2P)}$	$N_{\chi_b(3P)}$	
Maximum uncertainty	-0.1	1.7	—	0.4	-0.4	—	-2.7	3.3	—	-1.0	1.3	—
(b) $10 < p_T^{\Upsilon(1S)} < 18 \text{ GeV}/c$												
$\Upsilon(1S)$ transverse momentum intervals, GeV/c												
10 - 14						14 - 18						
$\sqrt{s} = 7 \text{ TeV}$			$\sqrt{s} = 8 \text{ TeV}$			$\sqrt{s} = 7 \text{ TeV}$			$\sqrt{s} = 8 \text{ TeV}$			
$N_{\chi_b(1P)}$	$N_{\chi_b(2P)}$	$N_{\chi_b(3P)}$	$N_{\chi_b(1P)}$	$N_{\chi_b(2P)}$	$N_{\chi_b(3P)}$	$N_{\chi_b(1P)}$	$N_{\chi_b(2P)}$	$N_{\chi_b(3P)}$	$N_{\chi_b(1P)}$	$N_{\chi_b(2P)}$	$N_{\chi_b(3P)}$	
Maximum uncertainty	-0.4	-0.6	-3.7	0.1	-0.3	0.5	0.5	-0.7	3.4	0.5	-0.8	-1.2
(c) $18 < p_T^{\Upsilon(1S)} < 40 \text{ GeV}/c$												
$\Upsilon(1S)$ transverse momentum intervals, GeV/c												
18 - 22						22 - 40						
$\sqrt{s} = 7 \text{ TeV}$			$\sqrt{s} = 8 \text{ TeV}$			$\sqrt{s} = 7 \text{ TeV}$			$\sqrt{s} = 8 \text{ TeV}$			
$N_{\chi_b(1P)}$	$N_{\chi_b(2P)}$	$N_{\chi_b(3P)}$	$N_{\chi_b(1P)}$	$N_{\chi_b(2P)}$	$N_{\chi_b(3P)}$	$N_{\chi_b(1P)}$	$N_{\chi_b(2P)}$	$N_{\chi_b(3P)}$	$N_{\chi_b(1P)}$	$N_{\chi_b(2P)}$	$N_{\chi_b(3P)}$	
Maximum uncertainty	0.9	-0.5	-7.0	0.4	-2.3	2.3	0.6	-1.9	-2.2	-0.5	-4.1	-10.8

Table 5.18: χ_b yields systematic uncertainties (%) related to $\chi_{b1}(3P)$ mass uncertainty in the fit model for $\chi_b(1, 2, 3P) \rightarrow \Upsilon(1S)\gamma$ decays

(a) $6 < p_T^{\Upsilon(1S)} < 10 \text{ GeV}/c$												
$\Upsilon(1S)$ transverse momentum intervals, GeV/c												
6 – 8						8 – 10						
$\sqrt{s} = 7 \text{ TeV}$			$\sqrt{s} = 8 \text{ TeV}$			$\sqrt{s} = 7 \text{ TeV}$			$\sqrt{s} = 8 \text{ TeV}$			
$N_{\chi_b(1P)}$	$N_{\chi_b(2P)}$	$N_{\chi_b(3P)}$	$N_{\chi_b(1P)}$	$N_{\chi_b(2P)}$	$N_{\chi_b(3P)}$	$N_{\chi_b(1P)}$	$N_{\chi_b(2P)}$	$N_{\chi_b(3P)}$	$N_{\chi_b(1P)}$	$N_{\chi_b(2P)}$	$N_{\chi_b(3P)}$	
$m_{\chi_{b1}(3P)} = 10,502 \text{ MeV}/c^2$	0.0	-0.2	—	-0.0	-0.2	—	0.0	0.0	—	0.0	0.0	—
$m_{\chi_{b1}(3P)} = 10,518 \text{ MeV}/c^2$	0.0	-0.2	—	-0.0	-0.2	—	0.0	0.0	—	0.0	0.0	—

(b) $10 < p_T^{\Upsilon(1S)} < 18 \text{ GeV}/c$												
$\Upsilon(1S)$ transverse momentum intervals, GeV/c												
10 – 14						14 – 18						
$\sqrt{s} = 7 \text{ TeV}$			$\sqrt{s} = 8 \text{ TeV}$			$\sqrt{s} = 7 \text{ TeV}$			$\sqrt{s} = 8 \text{ TeV}$			
$N_{\chi_b(1P)}$	$N_{\chi_b(2P)}$	$N_{\chi_b(3P)}$	$N_{\chi_b(1P)}$	$N_{\chi_b(2P)}$	$N_{\chi_b(3P)}$	$N_{\chi_b(1P)}$	$N_{\chi_b(2P)}$	$N_{\chi_b(3P)}$	$N_{\chi_b(1P)}$	$N_{\chi_b(2P)}$	$N_{\chi_b(3P)}$	
$m_{\chi_{b1}(3P)} = 10,502 \text{ MeV}/c^2$	0.2	-0.8	-4.1	-0.2	-0.6	-2.5	0.1	-0.9	-5.8	-0.1	0.3	4.6
$m_{\chi_{b1}(3P)} = 10,518 \text{ MeV}/c^2$	-0.1	1.7	12.7	-0.4	1.8	0.9	-0.3	2.5	15.0	0.1	-0.3	-5.4

(c) $18 < p_T^{\Upsilon(1S)} < 40 \text{ GeV}/c$												
$\Upsilon(1S)$ transverse momentum intervals, GeV/c												
18 – 22						22 – 40						
$\sqrt{s} = 7 \text{ TeV}$			$\sqrt{s} = 8 \text{ TeV}$			$\sqrt{s} = 7 \text{ TeV}$			$\sqrt{s} = 8 \text{ TeV}$			
$N_{\chi_b(1P)}$	$N_{\chi_b(2P)}$	$N_{\chi_b(3P)}$	$N_{\chi_b(1P)}$	$N_{\chi_b(2P)}$	$N_{\chi_b(3P)}$	$N_{\chi_b(1P)}$	$N_{\chi_b(2P)}$	$N_{\chi_b(3P)}$	$N_{\chi_b(1P)}$	$N_{\chi_b(2P)}$	$N_{\chi_b(3P)}$	
$m_{\chi_{b1}(3P)} = 10,502 \text{ MeV}/c^2$	-0.2	1.4	13.3	0.0	-0.5	-3.5	-0.1	0.2	2.9	-0.1	0.8	7.5
$m_{\chi_{b1}(3P)} = 10,518 \text{ MeV}/c^2$	0.3	-1.9	-17.6	-0.1	0.8	7.7	-0.1	1.2	-0.4	-0.0	-0.7	-10.0

Table 5.19: χ_b yields systematic uncertainties (%) related to λ values in the fit model for $\chi_b(2, 3P) \rightarrow \Upsilon(2S)\gamma$ decays

(a) $18 < p_T^{\Upsilon(2S)} < 24 \text{ GeV}/c$

	$\Upsilon(2S)$ transverse momentum intervals, GeV/c											
	18 - 22				18 - 24				22 - 24			
	$\sqrt{s} = 7 \text{ TeV}$		$\sqrt{s} = 8 \text{ TeV}$		$\sqrt{s} = 7 \text{ TeV}$		$\sqrt{s} = 8 \text{ TeV}$		$\sqrt{s} = 7 \text{ TeV}$		$\sqrt{s} = 8 \text{ TeV}$	
	$N_{\chi_b(2P)}$	$N_{\chi_b(3P)}$	$N_{\chi_b(2P)}$	$N_{\chi_b(3P)}$	$N_{\chi_b(2P)}$	$N_{\chi_b(3P)}$	$N_{\chi_b(2P)}$	$N_{\chi_b(3P)}$	$N_{\chi_b(2P)}$	$N_{\chi_b(3P)}$	$N_{\chi_b(2P)}$	$N_{\chi_b(3P)}$
$\lambda = 0.0$	22.1	—	13.6	—	—	18.8	—	12.6	5.6	—	3.8	—
$\lambda = 0.1$	15.8	—	9.3	—	—	14.0	—	8.8	2.3	—	1.1	—
$\lambda = 0.2$	10.1	—	5.8	—	—	9.2	—	5.6	-0.1	—	-0.7	—
$\lambda = 0.3$	5.6	—	3.2	—	—	5.4	—	3.0	-1.3	—	-1.6	—
$\lambda = 0.4$	2.1	—	1.1	—	—	2.2	—	1.0	-1.3	—	-1.3	—
$\lambda = 0.5$	0.0	—	0.0	—	—	0.0	—	0.0	0.0	—	0.0	—
$\lambda = 0.6$	-1.0	—	-0.0	—	—	-1.1	—	1.3	2.8	—	2.1	—
$\lambda = 0.7$	-0.8	—	0.9	—	—	-1.3	—	3.5	6.4	—	5.6	—
$\lambda = 0.8$	0.5	—	2.9	—	—	-0.2	—	5.4	11.5	—	10.0	—
$\lambda = 0.9$	2.8	—	5.8	—	—	1.6	—	7.2	17.5	—	15.3	—
$\lambda = 1.0$	6.2	—	9.1	—	—	4.1	—	10.5	24.3	—	21.3	—

(b) $24 < p_T^{\Upsilon(2S)} < 40 \text{ GeV}/c$

	$\Upsilon(2S)$ transverse momentum intervals, GeV/c			
	24 - 40			
	$\sqrt{s} = 7 \text{ TeV}$		$\sqrt{s} = 8 \text{ TeV}$	
	$N_{\chi_b(2P)}$	$N_{\chi_b(3P)}$	$N_{\chi_b(2P)}$	$N_{\chi_b(3P)}$
$\lambda = 0.0$	12.5	3.7	13.8	-9.6
$\lambda = 0.1$	8.1	2.1	9.5	-9.6
$\lambda = 0.2$	4.6	1.0	5.9	-8.5
$\lambda = 0.3$	2.0	0.4	3.1	-6.6
$\lambda = 0.4$	0.5	-0.1	1.1	-3.9
$\lambda = 0.5$	0.0	0.0	0.0	0.0
$\lambda = 0.6$	0.9	0.0	-0.3	4.3
$\lambda = 0.7$	2.8	0.5	0.3	8.9
$\lambda = 0.8$	5.7	1.1	1.7	14.3
$\lambda = 0.9$	9.6	2.3	3.9	20.1
$\lambda = 1.0$	14.4	3.9	6.8	25.8

Table 5.20: χ_b yields systematic uncertainties (%) related to $\chi_{b1}(2P)$ mass uncertainty in the fit model for $\chi_b(2, 3P) \rightarrow \Upsilon(2S)\gamma$ decays

(a) $18 < p_T^{\Upsilon(2S)} < 24 \text{ GeV}/c$

	$\Upsilon(2S)$ transverse momentum intervals, GeV/c											
	18 - 22				18 - 24				22 - 24			
	$\sqrt{s} = 7 \text{ TeV}$		$\sqrt{s} = 8 \text{ TeV}$		$\sqrt{s} = 7 \text{ TeV}$		$\sqrt{s} = 8 \text{ TeV}$		$\sqrt{s} = 7 \text{ TeV}$		$\sqrt{s} = 8 \text{ TeV}$	
	$N_{\chi_b(2P)}$	$N_{\chi_b(3P)}$	$N_{\chi_b(2P)}$	$N_{\chi_b(3P)}$	$N_{\chi_b(2P)}$	$N_{\chi_b(3P)}$	$N_{\chi_b(2P)}$	$N_{\chi_b(3P)}$	$N_{\chi_b(2P)}$	$N_{\chi_b(3P)}$	$N_{\chi_b(2P)}$	$N_{\chi_b(3P)}$
Maximum uncertainty	-1.1	—	-0.4	—	—	-2.6	—	1.7	-1.4	—	-0.2	—

(b) $24 < p_T^{\Upsilon(2S)} < 40 \text{ GeV}/c$

	$\Upsilon(2S)$ transverse momentum intervals, GeV/c			
	24 - 40			
	$\sqrt{s} = 7 \text{ TeV}$		$\sqrt{s} = 8 \text{ TeV}$	
	$N_{\chi_b(2P)}$	$N_{\chi_b(3P)}$	$N_{\chi_b(2P)}$	$N_{\chi_b(3P)}$
Maximum uncertainty	2.8	1.3	-0.5	10.5

Table 5.21: χ_b yields systematic uncertainties (%) related to $\chi_{b1}(3P)$ mass uncertainty in the fit model for $\chi_b(2, 3P) \rightarrow \Upsilon(2S)\gamma$ decays

(a) $18 < p_T^{\Upsilon(2S)} < 24 \text{ GeV}/c$

	$\Upsilon(2S)$ transverse momentum intervals, GeV/c											
	18 - 22				18 - 24				22 - 24			
	$\sqrt{s} = 7 \text{ TeV}$		$\sqrt{s} = 8 \text{ TeV}$		$\sqrt{s} = 7 \text{ TeV}$		$\sqrt{s} = 8 \text{ TeV}$		$\sqrt{s} = 7 \text{ TeV}$		$\sqrt{s} = 8 \text{ TeV}$	
	$N_{\chi_b(2P)}$	$N_{\chi_b(3P)}$	$N_{\chi_b(2P)}$	$N_{\chi_b(3P)}$	$N_{\chi_b(2P)}$	$N_{\chi_b(3P)}$	$N_{\chi_b(2P)}$	$N_{\chi_b(3P)}$	$N_{\chi_b(2P)}$	$N_{\chi_b(3P)}$	$N_{\chi_b(2P)}$	$N_{\chi_b(3P)}$
$m_{\chi_{b1}(3P)} = 10, 502 \text{ MeV}/c^2$	-0.0	—	-0.1	—	—	-4.5	—	0.3	-0.3	—	-0.1	—
$m_{\chi_{b1}(3P)} = 10, 518 \text{ MeV}/c^2$	-0.0	—	0.1	—	—	12.0	—	6.4	1.0	—	-0.2	—

(b) $24 < p_T^{\Upsilon(2S)} < 40 \text{ GeV}/c$

	$\Upsilon(2S)$ transverse momentum intervals, GeV/c			
	24 - 40			
	$\sqrt{s} = 7 \text{ TeV}$		$\sqrt{s} = 8 \text{ TeV}$	
	$N_{\chi_b(2P)}$	$N_{\chi_b(3P)}$	$N_{\chi_b(2P)}$	$N_{\chi_b(3P)}$
$m_{\chi_{b1}(3P)} = 10, 502 \text{ MeV}/c^2$	0.1	-0.0	0.1	13.7
$m_{\chi_{b1}(3P)} = 10, 518 \text{ MeV}/c^2$	0.6	10.0	-0.1	-18.1

Table 5.22: χ_b yields systematic uncertainties (%) related to λ values in the fit model for $\chi_b(3P) \rightarrow \Upsilon(3S)\gamma$ decays

	$\Upsilon(3S)$ transverse momentum intervals, GeV/c	
	27 - 40	
	$\sqrt{s} = 7$ TeV	$\sqrt{s} = 8$ TeV
	$N_{\chi_b(3P)}$	$N_{\chi_b(3P)}$
$\lambda = 0.0$	-5.8	10.9
$\lambda = 0.1$	-6.8	6.8
$\lambda = 0.2$	-6.6	3.8
$\lambda = 0.3$	-5.3	1.7
$\lambda = 0.4$	-3.2	0.5
$\lambda = 0.5$	0.0	0.0
$\lambda = 0.6$	4.1	0.2
$\lambda = 0.7$	9.3	1.0
$\lambda = 0.8$	15.5	2.3
$\lambda = 0.9$	22.8	4.3
$\lambda = 1.0$	31.2	6.7

Table 5.23: χ_b yields systematic uncertainties (%) related to $\chi_{b1}(3P)$ mass uncertainty in the fit model for $\chi_b(3P) \rightarrow \Upsilon(3S)\gamma$ decays

	$\Upsilon(3S)$ transverse momentum intervals, GeV/c	
	27 - 40	
	$\sqrt{s} = 7$ TeV	$\sqrt{s} = 8$ TeV
	$N_{\chi_b(3P)}$	$N_{\chi_b(3P)}$
$m_{\chi_{b1}(3P)} = 10,502$ MeV/c ²	25.7	0.6
$m_{\chi_{b1}(3P)} = 10,518$ MeV/c ²	-20.0	20.5

5.8.2 Photon reconstruction efficiency

The photon reconstruction efficiency, taken from simulation, needs not to be the same as in real data. The detailed comparison between MonteCarlo and data, presented in Section 5.6.1, shows that the differences are small. We assign a systematic uncertainty based on previous studies of photon reconstruction efficiencies. These studies compare the $B^+ \rightarrow J/\psi K^{*+}$ and $B^+ \rightarrow J/\psi K^+$ yields in data and MonteCarlo in order to determine the neutral pion, hence the photon reconstruction efficiency. A systematic uncertainty of 3% is assigned to this effect.

5.8.3 χ_b polarization

The prompt χ_b polarization is unknown. The simulated χ_b mesons are unpolarized and all the efficiencies given in the previous sections are therefore determined under the assumption that the χ_{b1} and the χ_{b2} mesons are produced unpolarized. The photon and Υ momentum distributions depend on the polarization of the χ_b state and the same is true for the efficiencies. The correction factors for the efficiencies under other polarization scenarios are derived in this section.

The angular distribution of the $\chi_b \rightarrow \Upsilon\gamma$ decay is described by the angles θ_Υ , θ_{χ_b} and ϕ where:

- θ_Υ is the angle between the directions of the positive muon in the Υ rest frame and the Υ in the χ_b rest frame;
- θ_{χ_b} is the angle between the directions of the Υ in the χ_b rest frame and the χ_b in the laboratory frame;
- ϕ is the angle between the Υ decay plane in the χ_b rest frame and the plane formed by the χ_b direction in the laboratory frame and the direction of the Υ in the χ_b rest frame.

The angular distributions of the χ_b states depend on $m_{\chi_{bJ}} \in \{-J, J\}$, the azimuthal angular momentum of the χ_{bJ} state. For each simulated event in the unpolarized sample, a weight is calculated from the values of the above angles in the various polarization hypotheses and the efficiency is deduced for each $m_{\chi_{b1}}$, $m_{\chi_{b2}}$ polarization.

As an example, Figures 5.24 and 5.25 show the angular distributions in the $\chi_{b1,2}(1P) \rightarrow \Upsilon(1S)\gamma$ decay for unpolarized and various polarization scenarios for the χ_b mesons. The resulting ratio of the unpolarized and polarized efficiencies as a function of p_T are shown in Figure 5.26. The statistical errors are estimated by the jackknife method [48, 49]. The corresponding ratios for $\chi_{b1,2}(2P) \rightarrow \Upsilon(1S)\gamma$ decays are given in Figure 5.27.

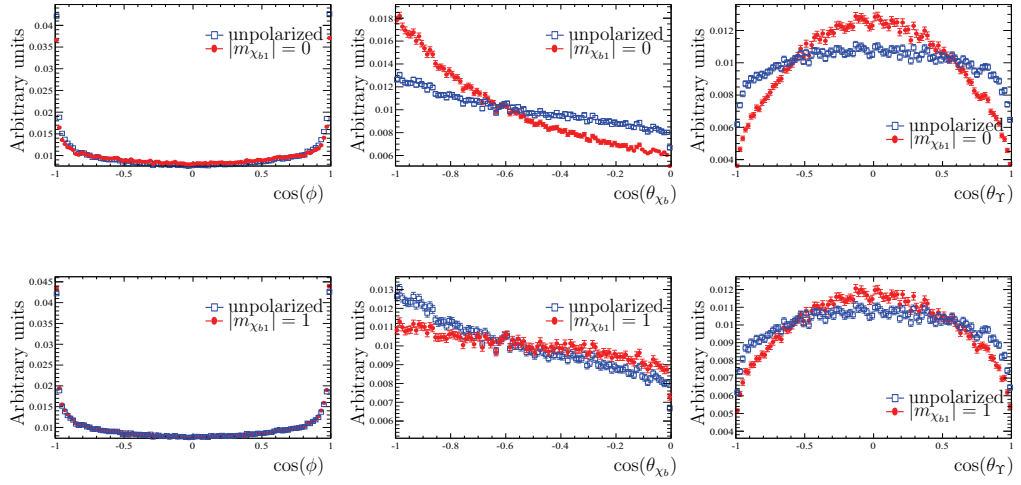


Figure 5.24: Angular distributions of simulated events in $\chi_{b1}(1P) \rightarrow \Upsilon(1S)\gamma$ decay. The blue curves corresponds to unpolarized events distribution and the red curves corresponds to specified polarized events distribution. All histograms are normalized by the corresponding integral.

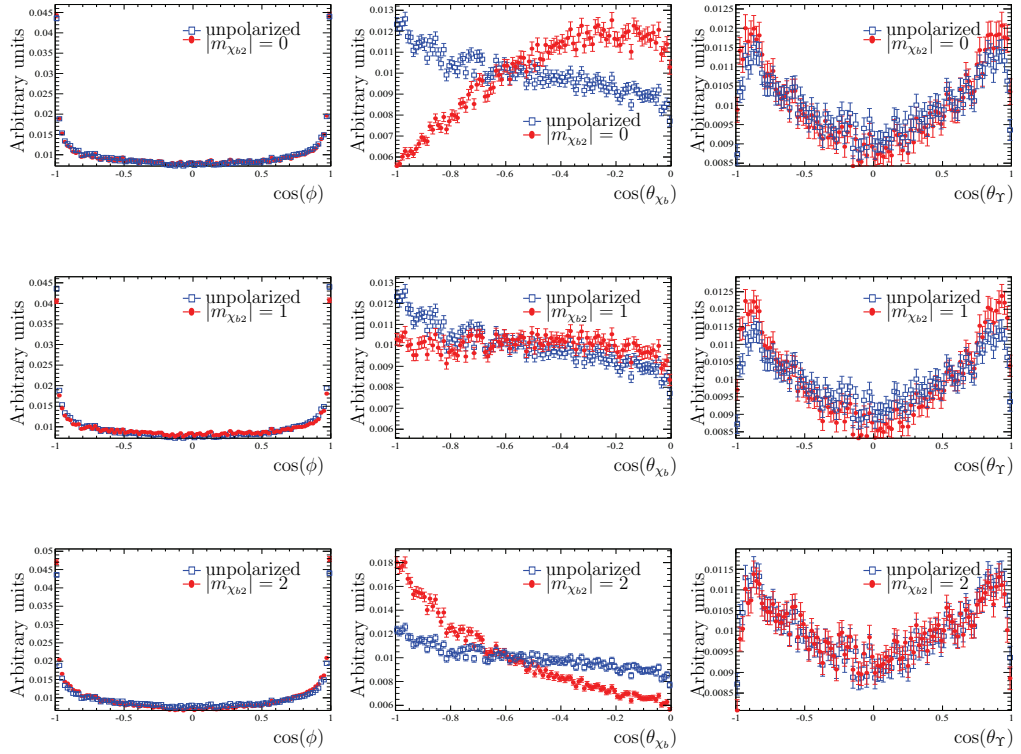


Figure 5.25: Angular distributions of simulated events in $\chi_{b2}(1P) \rightarrow \Upsilon(1S)\gamma$ decay. The blue curves corresponds to unpolarized events distribution and the red curves corresponds to specified polarized events distribution. All histograms are normalized by the corresponding integral.

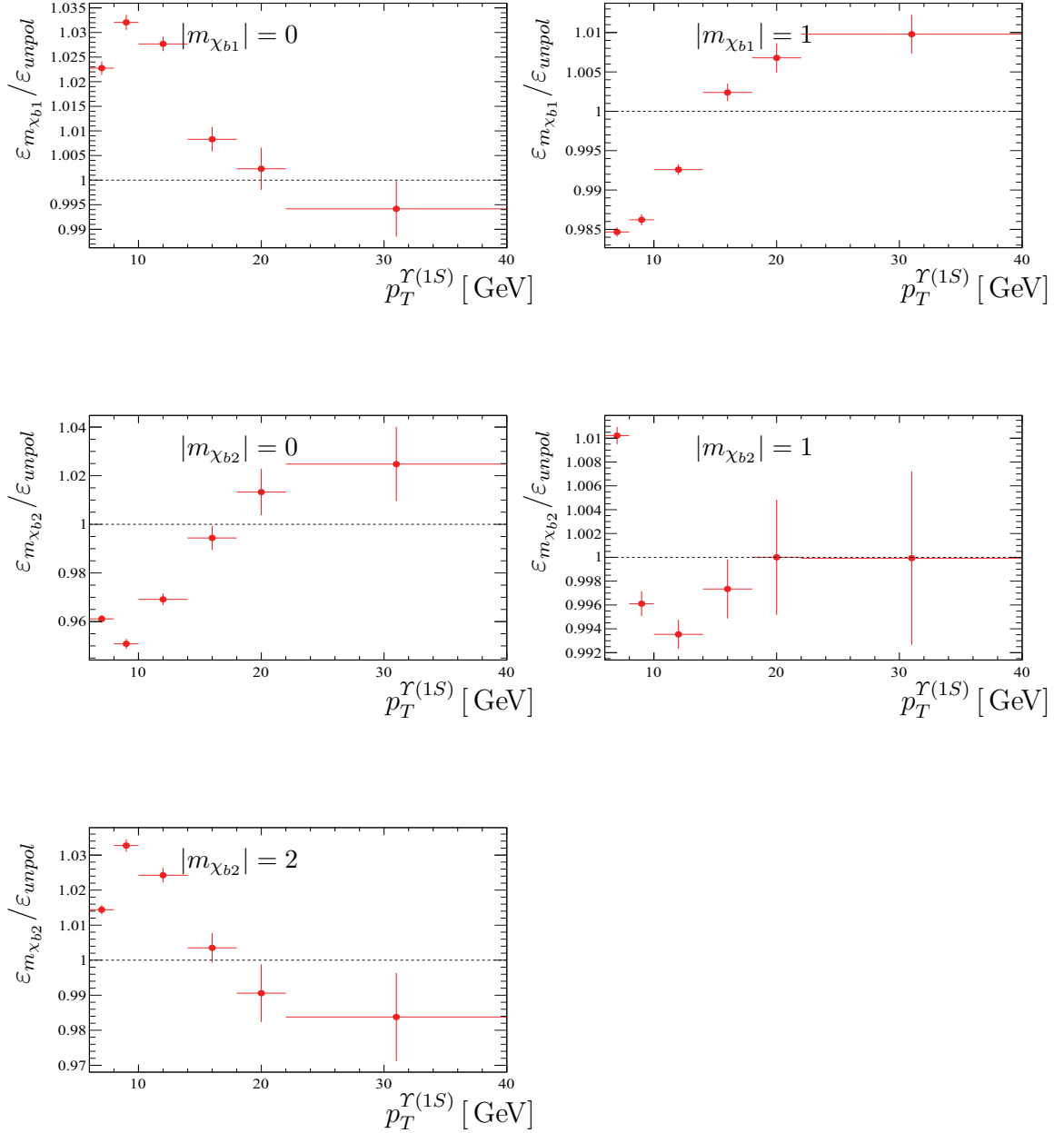


Figure 5.26: Ratio between efficiency for polarized events and the corresponding efficiency for unpolarized events in $\chi_b(1P) \rightarrow \Upsilon(1S)\gamma$ decays. The results are shown in specified intervals of $\Upsilon(1S)$ transverse momentum.

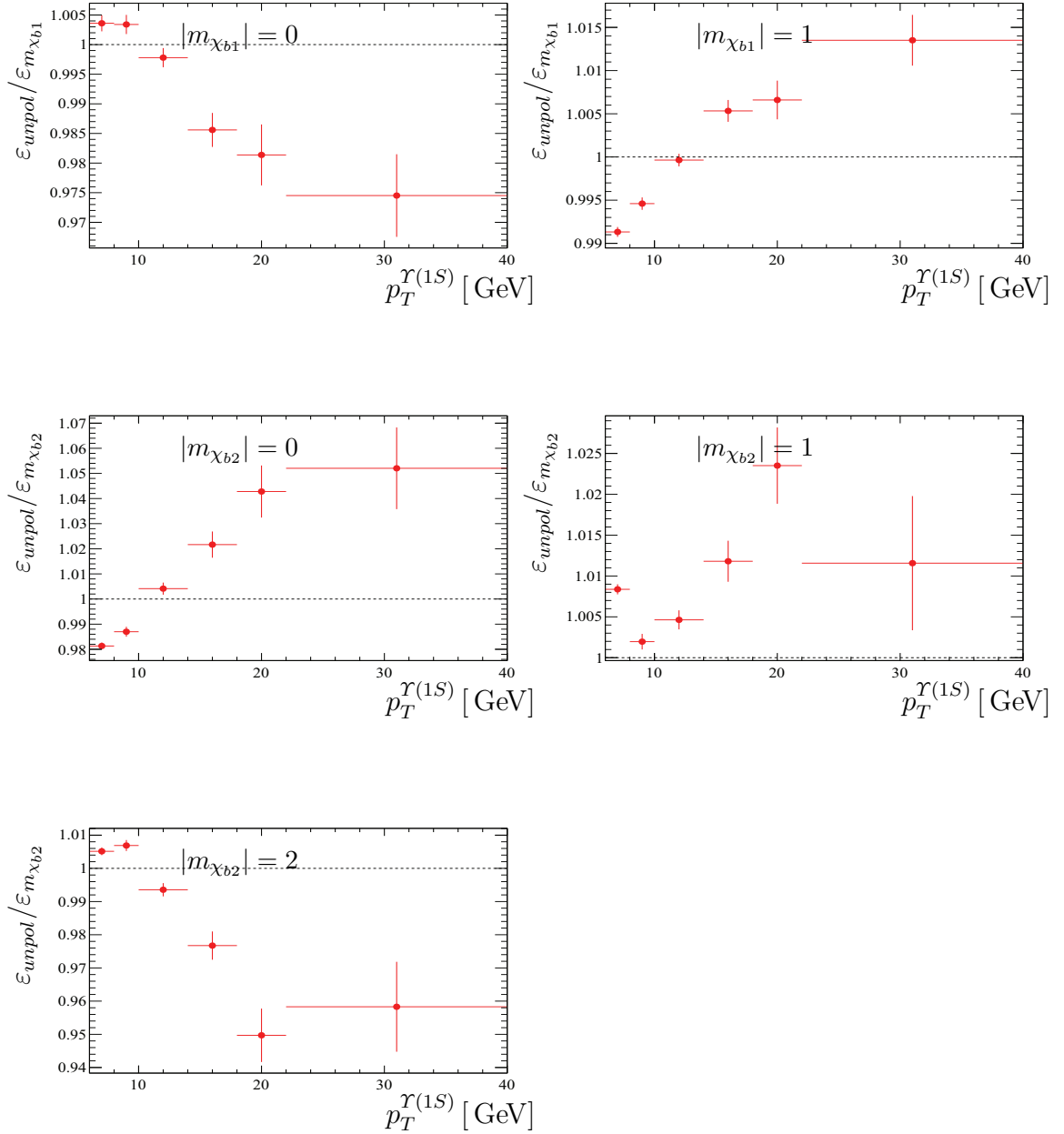


Figure 5.27: Ratio between efficiency for polarized events and the corresponding efficiency for unpolarized events in $\chi_b(2P) \rightarrow \Upsilon(1S)\gamma$ decays. The results are shown in specified intervals of $\Upsilon(1S)$ transverse momentum.

The systematic uncertainty for different polarization scenarios is estimated as the maximum deviation of the ratio between efficiency measured for unpolarized particles and

all possible polarization scenarios. The results are shown in Tables 5.24 to 5.26.

Table 5.24: Maximum deviation (%) of ratio between efficiency measured for unpolarized particles and all possible polarization scenarios in $\chi_b \rightarrow \Upsilon(1S)\gamma$ decays

	$\Upsilon(1S)$ transverse momentum intervals, GeV/ c					
	6 – 8	8 – 10	10 – 14	14 – 18	18 – 22	22 – 40
$\chi_b(1P) \rightarrow \Upsilon(1S)\gamma$	+2.4 -4.0	+3.5 -5.1	+2.9 -3.3	+1.1 -1.1	+2.3 -1.8	+4.0 -2.9
$\chi_b(2P) \rightarrow \Upsilon(1S)\gamma$	+0.9 -2.0	+0.9 -1.5	+0.7 -0.8	+2.7 -2.8	+5.3 -5.8	+6.8 -5.5
$\chi_b(3P) \rightarrow \Upsilon(1S)\gamma$	—	—	+2.2 -2.4	+5.2 -5.3	+6.7 -6.9	+5.9 -6.3

Table 5.25: Maximum deviation (%) of ratio between efficiency measured for unpolarized particles and all possible polarization scenarios in $\chi_b \rightarrow \Upsilon(2S)\gamma$ decays

	$\Upsilon(2S)$ transverse momentum intervals, GeV/ c			
	18 – 22	18 – 24	22 – 24	24 – 40
$\chi_b(2P) \rightarrow \Upsilon(2S)\gamma$	+7.8 -8.7	—	+6.1 -3.6	+4.6 -4.3
$\chi_b(3P) \rightarrow \Upsilon(2S)\gamma$	—	+2.7 -2.6	—	+4.2 -4.5

Table 5.26: Maximum deviation (%) of ratio between efficiency measured for unpolarized particles and all possible polarization scenarios in $\chi_b \rightarrow \Upsilon(3S)\gamma$ decays

	$\Upsilon(3S)$ transverse momentum intervals, GeV/ c	
	27 – 40	
$\chi_b(3P) \rightarrow \Upsilon(3S)\gamma$	+7.5 -6.4	

5.8.4 Summary of systematic uncertainties on the Υ production fractions

The systematic uncertainties determined in the previous subsections on the various term of Equation (5.1) give corresponding uncertainties on the Υ fraction measured in this study. These uncertainties are summarized for each systematic source in Tables 5.27 and 5.28.

For simplicity, Table 5.28 shows only the maximum systematic uncertainties observed in all bins and energies for the corresponding decays.

Table 5.27: Υ fraction uncertainties common to all χ_b decays (%)

Υ fit model	± 0.7
γ reconstruction	± 3

Table 5.28: Summary of Υ fraction systematic uncertainties (%)

	χ_b fit model	χ_b polarization
$\chi_b(1P) \rightarrow \Upsilon(1S)\gamma$	+4.3 -5.8	+5.1 -4.0
$\chi_b(2P) \rightarrow \Upsilon(1S)\gamma$	+4.8 -6.2	+5.8 -6.8
$\chi_b(3P) \rightarrow \Upsilon(1S)\gamma$	+19.6 -16.6	+6.9 -6.7
$\chi_b(2P) \rightarrow \Upsilon(2S)\gamma$	+2.3 -7.0	+8.7 -7.8
$\chi_b(3P) \rightarrow \Upsilon(2S)\gamma$	+19.7 -19.9	+4.5 -4.2
$\chi_b(3P) \rightarrow \Upsilon(3S)\gamma$	+20.9 -27.6	+6.4 -7.5

5.9 Results

In summary, the fractions of $\Upsilon(1, 2, 3S)$ mesons originating from $\chi_b(1, 2, 3P)$ radiative decays has been measured on the full data sample collected by LHCb in 2011 and 2012 at center of mass energies of 7 and 8 TeV respectively, as a function of the Υ transverse momentum. Results are shown in Figure 5.28 and Tables 5.29 to 5.31. Figure 5.29 shows previous LHCb results which are consistent with the current ones.

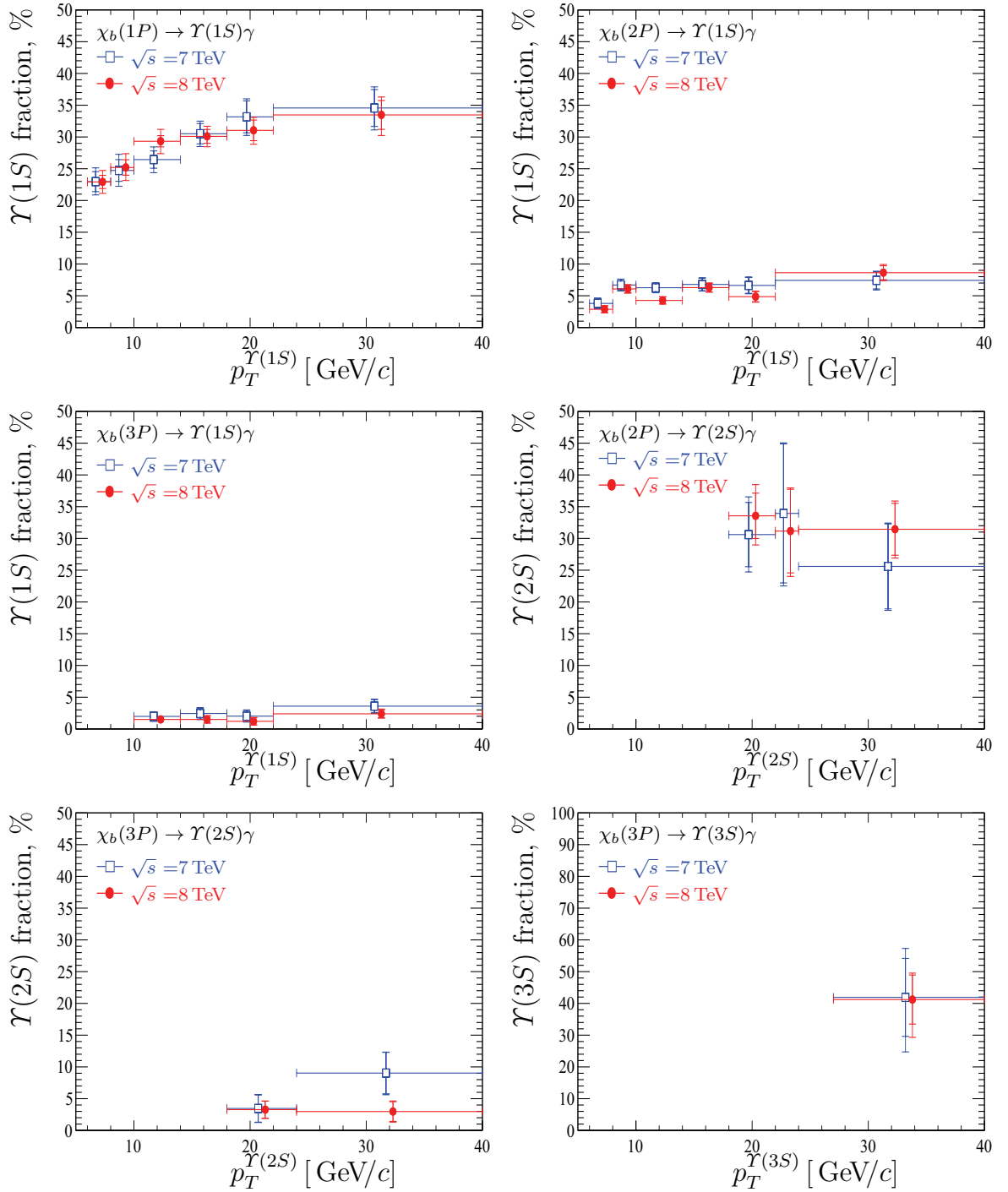


Figure 5.28: Fraction of Υ originated from χ_b decays in the specified p_T^{Υ} ranges. Outer error bars show statistical and systematic errors, inner error bars — only statistical errors.

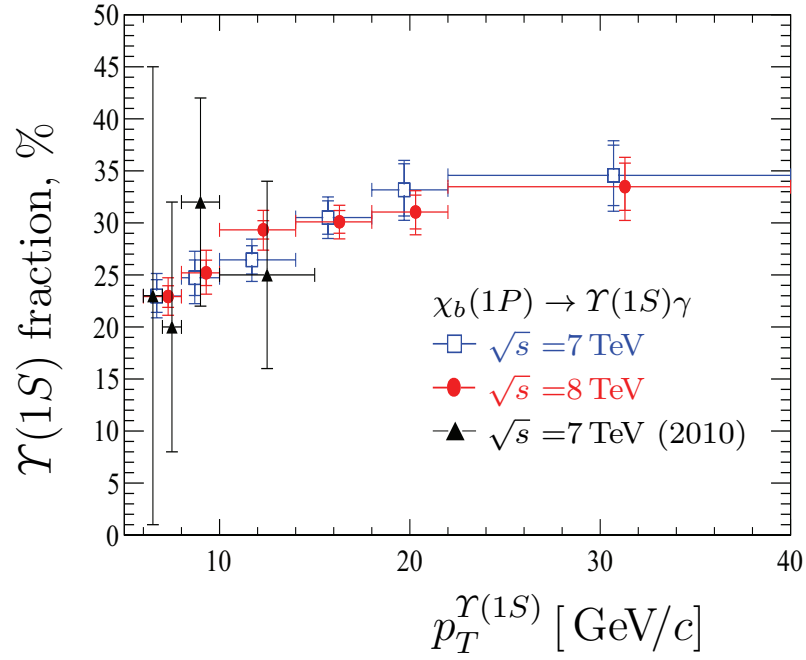


Figure 5.29: Fraction of $\Upsilon(1S)$ originated from $\chi_b(1P)$ decays in the specified $p_T^{\Upsilon(1S)}$ ranges compared to the previous results. Outer error bars show statistical and systematic errors, inner error bars — only statistical errors.

Table 5.29: $\Upsilon(1S)$ fraction originating from χ_b decay

(a) $6 < p_T^{\Upsilon(1S)} < 8 \text{ GeV}/c$		
$\Upsilon(1S)$ transverse momentum intervals, GeV/c		
6 – 8		
	$\sqrt{s} = 7 \text{ TeV}$	$\sqrt{s} = 8 \text{ TeV}$
$\chi_b(1P) \rightarrow \Upsilon(1S)\gamma$	23.0 ± 1.6 (stat) $^{+1.1}_{-1.3}$ (syst) $^{+0.9}_{-0.6}$ (syst.pol)%	22.9 ± 1.0 (stat) $^{+1.1}_{-1.4}$ (syst) $^{+0.9}_{-0.6}$ (syst.pol)%
$\chi_b(2P) \rightarrow \Upsilon(1S)\gamma$	3.8 ± 0.8 (stat) $^{+0.2}_{-0.2}$ (syst) $^{+0.1}_{-0.0}$ (syst.pol)%	2.9 ± 0.5 (stat) $^{+0.2}_{-0.1}$ (syst) $^{+0.1}_{-0.0}$ (syst.pol)%
$\chi_b(3P) \rightarrow \Upsilon(1S)\gamma$	—	—
(b) $8 < p_T^{\Upsilon(1S)} < 10 \text{ GeV}/c$		
$\Upsilon(1S)$ transverse momentum intervals, GeV/c		
8 – 10		
	$\sqrt{s} = 7 \text{ TeV}$	$\sqrt{s} = 8 \text{ TeV}$
$\chi_b(1P) \rightarrow \Upsilon(1S)\gamma$	24.7 ± 1.7 (stat) $^{+1.3}_{-1.6}$ (syst) $^{+1.3}_{-0.9}$ (syst.pol)%	25.2 ± 1.2 (stat) $^{+1.2}_{-1.4}$ (syst) $^{+1.3}_{-0.9}$ (syst.pol)%
$\chi_b(2P) \rightarrow \Upsilon(1S)\gamma$	6.7 ± 0.9 (stat) $^{+0.3}_{-0.3}$ (syst) $^{+0.1}_{-0.1}$ (syst.pol)%	6.1 ± 0.6 (stat) $^{+0.3}_{-0.2}$ (syst) $^{+0.1}_{-0.1}$ (syst.pol)%
$\chi_b(3P) \rightarrow \Upsilon(1S)\gamma$	—	—
(c) $10 < p_T^{\Upsilon(1S)} < 14 \text{ GeV}/c$		
$\Upsilon(1S)$ transverse momentum intervals, GeV/c		
10 – 14		
	$\sqrt{s} = 7 \text{ TeV}$	$\sqrt{s} = 8 \text{ TeV}$
$\chi_b(1P) \rightarrow \Upsilon(1S)\gamma$	26.4 ± 1.4 (stat) $^{+1.1}_{-1.4}$ (syst) $^{+0.9}_{-0.8}$ (syst.pol)%	29.3 ± 0.9 (stat) $^{+1.3}_{-1.5}$ (syst) $^{+1.0}_{-0.9}$ (syst.pol)%
$\chi_b(2P) \rightarrow \Upsilon(1S)\gamma$	6.3 ± 0.8 (stat) $^{+0.3}_{-0.4}$ (syst) $^{+0.1}_{-0.2}$ (syst.pol)%	4.3 ± 0.6 (stat) $^{+0.2}_{-0.3}$ (syst) $^{+0.0}_{-0.2}$ (syst.pol)%
$\chi_b(3P) \rightarrow \Upsilon(1S)\gamma$	2.0 ± 0.7 (stat) $^{+0.2}_{-0.3}$ (syst) $^{+0.0}_{-0.0}$ (syst.pol)%	1.5 ± 0.5 (stat) $^{+0.2}_{-0.2}$ (syst) $^{+0.0}_{-0.0}$ (syst.pol)%
(d) $14 < p_T^{\Upsilon(1S)} < 18 \text{ GeV}/c$		
$\Upsilon(1S)$ transverse momentum intervals, GeV/c		
14 – 18		
	$\sqrt{s} = 7 \text{ TeV}$	$\sqrt{s} = 8 \text{ TeV}$
$\chi_b(1P) \rightarrow \Upsilon(1S)\gamma$	30.5 ± 1.6 (stat) $^{+1.1}_{-1.2}$ (syst) $^{+0.3}_{-0.3}$ (syst.pol)%	30.1 ± 1.1 (stat) $^{+1.1}_{-1.2}$ (syst) $^{+0.3}_{-0.3}$ (syst.pol)%
$\chi_b(2P) \rightarrow \Upsilon(1S)\gamma$	6.8 ± 1.0 (stat) $^{+0.3}_{-0.4}$ (syst) $^{+0.2}_{-0.2}$ (syst.pol)%	6.3 ± 0.7 (stat) $^{+0.3}_{-0.3}$ (syst) $^{+0.2}_{-0.2}$ (syst.pol)%
$\chi_b(3P) \rightarrow \Upsilon(1S)\gamma$	2.4 ± 0.9 (stat) $^{+0.3}_{-0.4}$ (syst) $^{+0.1}_{-0.1}$ (syst.pol)%	1.5 ± 0.6 (stat) $^{+0.1}_{-0.1}$ (syst) $^{+0.1}_{-0.1}$ (syst.pol)%
(e) $18 < p_T^{\Upsilon(1S)} < 22 \text{ GeV}/c$		
$\Upsilon(1S)$ transverse momentum intervals, GeV/c		
18 – 22		
	$\sqrt{s} = 7 \text{ TeV}$	$\sqrt{s} = 8 \text{ TeV}$
$\chi_b(1P) \rightarrow \Upsilon(1S)\gamma$	33.2 ± 2.5 (stat) $^{+1.1}_{-1.3}$ (syst) $^{+0.6}_{-0.8}$ (syst.pol)%	31.0 ± 1.6 (stat) $^{+1.1}_{-1.3}$ (syst) $^{+0.5}_{-0.7}$ (syst.pol)%
$\chi_b(2P) \rightarrow \Upsilon(1S)\gamma$	6.6 ± 1.2 (stat) $^{+0.3}_{-0.3}$ (syst) $^{+0.4}_{-0.4}$ (syst.pol)%	4.9 ± 0.8 (stat) $^{+0.2}_{-0.2}$ (syst) $^{+0.3}_{-0.3}$ (syst.pol)%
$\chi_b(3P) \rightarrow \Upsilon(1S)\gamma$	2.0 ± 0.9 (stat) $^{+0.4}_{-0.3}$ (syst) $^{+0.1}_{-0.1}$ (syst.pol)%	1.2 ± 0.6 (stat) $^{+0.1}_{-0.1}$ (syst) $^{+0.1}_{-0.1}$ (syst.pol)%
(f) $22 < p_T^{\Upsilon(1S)} < 40 \text{ GeV}/c$		
$\Upsilon(1S)$ transverse momentum intervals, GeV/c		
22 – 40		
	$\sqrt{s} = 7 \text{ TeV}$	$\sqrt{s} = 8 \text{ TeV}$
$\chi_b(1P) \rightarrow \Upsilon(1S)\gamma$	34.6 ± 2.9 (stat) $^{+1.2}_{-1.3}$ (syst) $^{+1.0}_{-1.4}$ (syst.pol)%	33.5 ± 2.3 (stat) $^{+1.3}_{-1.5}$ (syst) $^{+1.0}_{-1.3}$ (syst.pol)%
$\chi_b(2P) \rightarrow \Upsilon(1S)\gamma$	7.4 ± 1.3 (stat) $^{+0.3}_{-0.5}$ (syst) $^{+0.4}_{-0.5}$ (syst.pol)%	8.6 ± 1.1 (stat) $^{+0.5}_{-0.3}$ (syst) $^{+0.5}_{-0.6}$ (syst.pol)%
$\chi_b(3P) \rightarrow \Upsilon(1S)\gamma$	3.6 ± 1.1 (stat) $^{+0.1}_{-0.3}$ (syst) $^{+0.2}_{-0.2}$ (syst.pol)%	2.4 ± 0.6 (stat) $^{+0.4}_{-0.2}$ (syst) $^{+0.2}_{-0.1}$ (syst.pol)%

Table 5.30: $\Upsilon(2S)$ fraction originating from χ_b decay

(a) $18 < p_T^{\Upsilon(2S)} < 22 \text{ GeV}/c$		
$\Upsilon(2S)$ transverse momentum intervals, GeV/c		
18 – 22		
	$\sqrt{s} = 7 \text{ TeV}$	$\sqrt{s} = 8 \text{ TeV}$
$\chi_b(2P) \rightarrow \Upsilon(2S)\gamma$	$31 \pm 5 \text{ (stat)}^{+1.1}_{-2.0} \text{ (syst)}^{+2.7}_{-2.4} \text{ (syst.pol)}\%$	$34 \pm 4 \text{ (stat)}^{+1.0}_{-1.6} \text{ (syst)}^{+2.9}_{-2.6} \text{ (syst.pol)}\%$
$\chi_b(3P) \rightarrow \Upsilon(2S)\gamma$	—	—
(b) $18 < p_T^{\Upsilon(2S)} < 24 \text{ GeV}/c$		
$\Upsilon(2S)$ transverse momentum intervals, GeV/c		
18 – 24		
	$\sqrt{s} = 7 \text{ TeV}$	$\sqrt{s} = 8 \text{ TeV}$
$\chi_b(2P) \rightarrow \Upsilon(2S)\gamma$	—	—
$\chi_b(3P) \rightarrow \Upsilon(2S)\gamma$	$3.5 \pm 2.2 \text{ (stat)}^{+0.2}_{-0.5} \text{ (syst)}^{+0.1}_{-0.1} \text{ (syst.pol)}\%$	$3.3 \pm 1.3 \text{ (stat)}^{+0.1}_{-0.3} \text{ (syst)}^{+0.1}_{-0.1} \text{ (syst.pol)}\%$
(c) $22 < p_T^{\Upsilon(2S)} < 24 \text{ GeV}/c$		
$\Upsilon(2S)$ transverse momentum intervals, GeV/c		
22 – 24		
	$\sqrt{s} = 7 \text{ TeV}$	$\sqrt{s} = 8 \text{ TeV}$
$\chi_b(2P) \rightarrow \Upsilon(2S)\gamma$	$34 \pm 11 \text{ (stat)}^{+1.3}_{-2.6} \text{ (syst)}^{+1.2}_{-2.1} \text{ (syst.pol)}\%$	$31 \pm 7 \text{ (stat)}^{+1.2}_{-2.1} \text{ (syst)}^{+1.1}_{-1.9} \text{ (syst.pol)}\%$
$\chi_b(3P) \rightarrow \Upsilon(2S)\gamma$	—	—
(d) $24 < p_T^{\Upsilon(2S)} < 40 \text{ GeV}/c$		
$\Upsilon(2S)$ transverse momentum intervals, GeV/c		
24 – 40		
	$\sqrt{s} = 7 \text{ TeV}$	$\sqrt{s} = 8 \text{ TeV}$
$\chi_b(2P) \rightarrow \Upsilon(2S)\gamma$	$26 \pm 7 \text{ (stat)}^{+0.8}_{-1.4} \text{ (syst)}^{+1.1}_{-1.2} \text{ (syst.pol)}\%$	$31 \pm 4 \text{ (stat)}^{+1.0}_{-1.4} \text{ (syst)}^{+1.4}_{-1.4} \text{ (syst.pol)}\%$
$\chi_b(3P) \rightarrow \Upsilon(2S)\gamma$	$9.0 \pm 3.3 \text{ (stat)}^{+0.3}_{-1.0} \text{ (syst)}^{+0.4}_{-0.4} \text{ (syst.pol)}\%$	$3.0 \pm 1.6 \text{ (stat)}^{+0.6}_{-0.6} \text{ (syst)}^{+0.1}_{-0.1} \text{ (syst.pol)}\%$

Table 5.31: $\Upsilon(3S)$ fraction originating from χ_b decay

$\Upsilon(3S)$ transverse momentum intervals, GeV/c		
27 – 40		
	$\sqrt{s} = 7 \text{ TeV}$	$\sqrt{s} = 8 \text{ TeV}$
$\chi_b(3P) \rightarrow \Upsilon(3S)\gamma$	$42 \pm 12 \text{ (stat)}^{+8.9}_{-11.6} \text{ (syst)}^{+2.7}_{-3.1} \text{ (syst.pol)}\%$	$41 \pm 8 \text{ (stat)}^{+1.3}_{-3.6} \text{ (syst)}^{+2.6}_{-3.1} \text{ (syst.pol)}\%$

The results in this study extend previous LHCb measurements to considerably more decays, higher transverse momentum regions and increased statistical precision. The measurement of the $\Upsilon(3S)$ production fraction due to radiative $\chi_b(3P)$ decays is performed for the first time.

Also, in this study the $\chi_{b1}(3P)$ mass was measured to be $10,508 \pm 2 \text{ (stat)} \pm 8 \text{ (syst)} \text{ MeV}/c^2$, which is in good agreement with a recent unpublished LHCb measurement with converted photons.

Chapter 6

Conclusion

In this thesis the following topics were addressed:

1. A software profiling tool was developed. This profiling tool helps to analyze and improve the performance of the LHCb software, with particular emphasis on the optimization of the High Level Trigger software. This tool is currently used within LHCb.
2. Measurements of the fractions of Υ mesons originating from χ_b radiative decays in proton-proton collisions at LHCb were obtained as a function of Υ transverse momentum in the rapidity range $2.0 < y^\Upsilon < 4.5$. This study was performed on a data set, corresponding to an integrated luminosity of 3 fb^{-1} , collected at centre-of-mass energies $\sqrt{s} = 7$ and 8 TeV by the LHCb experiment. The χ_b ($1P$, $2P$, $3P$) mesons were reconstructed in radiative decays to $\Upsilon(1S)$, $\Upsilon(2S)$ and $\Upsilon(3S)$. The results in this study extend the statistical precision of previous LHCb measurements and add considerably more decays and higher transverse momentum regions. The measurement of $\Upsilon(3S)$ fraction in radiative $\chi_b(3P)$ decay was performed for the first time.
3. A measurement of the $\chi_{b1}(3P)$ mass was performed. The result is in good agreement with a recent LHCb unpublished study with converted photons.

The software profiling tool is the subject of a publication in a peer-reviewed journal. The analysis of χ_b radiative decays has been reviewed in LHCb and will be the subject of a publication.

Appendices

Appendix A

Data fits for $\Upsilon \rightarrow \mu^+ \mu^-$ decays

The fit model for obtaining Υ yields is described at Section 5.3.2. Floating fit parameters and fit quality are shown in Table A.1 and corresponding plots are presented in Figures A.1 and A.2

Table A.1: $\mu^+\mu^-$ invariant mass data fit parameters

(a) $6 < p_T^{\mu^+\mu^-} < 14 \text{ GeV}/c$

	$\mu^+\mu^-$ transverse momentum intervals, GeV/c					
	6 – 8		8 – 10		10 – 14	
	$\sqrt{s} = 7 \text{ TeV}$	$\sqrt{s} = 8 \text{ TeV}$	$\sqrt{s} = 7 \text{ TeV}$	$\sqrt{s} = 8 \text{ TeV}$	$\sqrt{s} = 7 \text{ TeV}$	$\sqrt{s} = 8 \text{ TeV}$
$N_{\Upsilon(1S)}$	$124,100 \pm 400$	$282,600 \pm 600$	$70,480 \pm 290$	$164,300 \pm 500$	$60,780 \pm 270$	$143,700 \pm 400$
$N_{\Upsilon(2S)}$	$34,090 \pm 230$	$77,900 \pm 400$	$21,480 \pm 180$	$49,390 \pm 270$	$20,540 \pm 180$	$48,140 \pm 250$
$N_{\Upsilon(3S)}$	$17,730 \pm 190$	$40,150 \pm 280$	$12,050 \pm 140$	$27,080 \pm 210$	$12,600 \pm 140$	$29,300 \pm 220$
Background	$148,700 \pm 500$	$361,900 \pm 700$	$71,970 \pm 330$	$175,600 \pm 500$	$51,480 \pm 290$	$124,600 \pm 400$
$\mu_{\Upsilon(1S)}, \text{ MeV}/c^2$	9456.68 ± 0.15	9455.43 ± 0.10	9456.91 ± 0.21	9455.49 ± 0.13	9457.44 ± 0.22	9455.49 ± 0.15
$\sigma_{\Upsilon(1S)}, \text{ MeV}/c^2$	41.31 ± 0.24	41.45 ± 0.10	42.76 ± 0.10	42.65 ± 0.13	43.88 ± 0.21	44.70 ± 0.14
$\mu_{\Upsilon(2S)}, \text{ MeV}/c^2$	$10,019.12 \pm 0.35$	$10,017.62 \pm 0.23$	$10,019.0 \pm 0.4$	$10,017.85 \pm 0.29$	$10,018.8 \pm 0.5$	$10,018.01 \pm 0.10$
$\sigma_{\Upsilon(2S)}, \text{ MeV}/c^2$	44.34 ± 0.34	44.43 ± 0.22	45.8 ± 0.4	46.04 ± 0.26	47.7 ± 0.5	47.44 ± 0.09
$\mu_{\Upsilon(3S)}, \text{ MeV}/c^2$	$10,351.5 \pm 0.6$	$10,349.3 \pm 0.4$	$10,349.85 \pm 0.16$	$10,348.73 \pm 0.23$	$10,351.1 \pm 0.7$	$10,349.8 \pm 0.4$
$\sigma_{\Upsilon(3S)}, \text{ MeV}/c^2$	46.0 ± 0.6	46.0 ± 0.4	48.37 ± 0.09	47.80 ± 0.04	48.7 ± 0.6	49.2 ± 0.4
τ	-0.4757 ± 0.0033	-0.4709 ± 0.0021	-0.370 ± 0.005	-0.3692 ± 0.0030	-0.273 ± 0.005	-0.2602 ± 0.0035
$\chi^2/n.d.f$	1.83	2.26	1.5	1.7	1.36	1.64

(b) $14 < p_T^{\mu^+\mu^-} < 40 \text{ GeV}/c$

	$\mu^+\mu^-$ transverse momentum intervals, GeV/c					
	14 – 18		18 – 22		22 – 40	
	$\sqrt{s} = 7 \text{ TeV}$	$\sqrt{s} = 8 \text{ TeV}$	$\sqrt{s} = 7 \text{ TeV}$	$\sqrt{s} = 8 \text{ TeV}$	$\sqrt{s} = 7 \text{ TeV}$	$\sqrt{s} = 8 \text{ TeV}$
$N_{\Upsilon(1S)}$	$18,520 \pm 150$	$45,160 \pm 230$	5960 ± 90	$15,600 \pm 140$	3690 ± 70	9270 ± 110
$N_{\Upsilon(2S)}$	7300 ± 100	$17,490 \pm 160$	2670 ± 60	6620 ± 100	1680 ± 50	4340 ± 80
$N_{\Upsilon(3S)}$	4950 ± 90	$11,570 \pm 130$	1940 ± 50	4490 ± 80	1250 ± 50	3240 ± 70
Background	$14,260 \pm 160$	$34,770 \pm 250$	4910 ± 90	$11,710 \pm 140$	4500 ± 90	$10,600 \pm 140$
$\mu_{\Upsilon(1S)}, \text{ MeV}/c^2$	9457.4 ± 0.4	9456.53 ± 0.27	9460.0 ± 0.8	9455.4 ± 0.5	9458.0 ± 0.8	9456.3 ± 0.7
$\sigma_{\Upsilon(1S)}, \text{ MeV}/c^2$	46.8 ± 0.4	46.51 ± 0.25	48.1 ± 0.7	48.8 ± 0.5	49.8 ± 0.7	51.7 ± 0.7
$\mu_{\Upsilon(2S)}, \text{ MeV}/c^2$	$10,019.4 \pm 0.7$	$10,019.3 \pm 0.5$	$10,019.4 \pm 1.5$	$10,018.8 \pm 0.9$	$10,018.1 \pm 1.9$	$10,020.8 \pm 1.2$
$\sigma_{\Upsilon(2S)}, \text{ MeV}/c^2$	49.5 ± 0.7	50.1 ± 0.5	55.4 ± 1.4	53.0 ± 0.9	53.8 ± 1.8	54.4 ± 1.1
$\mu_{\Upsilon(3S)}, \text{ MeV}/c^2$	$10,351.3 \pm 1.0$	$10,349.3 \pm 0.7$	$10,350.8 \pm 1.9$	$10,351.5 \pm 1.2$	$10,351.9 \pm 2.4$	$10,352.7 \pm 1.4$
$\sigma_{\Upsilon(3S)}, \text{ MeV}/c^2$	52.2 ± 1.0	53.0 ± 0.7	57.6 ± 1.9	54.9 ± 1.1	57.4 ± 2.4	56.8 ± 1.4
τ	-0.193 ± 0.010	-0.170 ± 0.007	-0.151 ± 0.018	-0.117 ± 0.011	-0.136 ± 0.018	-0.114 ± 0.012
$\chi^2/n.d.f$	0.94	1.23	0.82	0.96	0.82	1.09

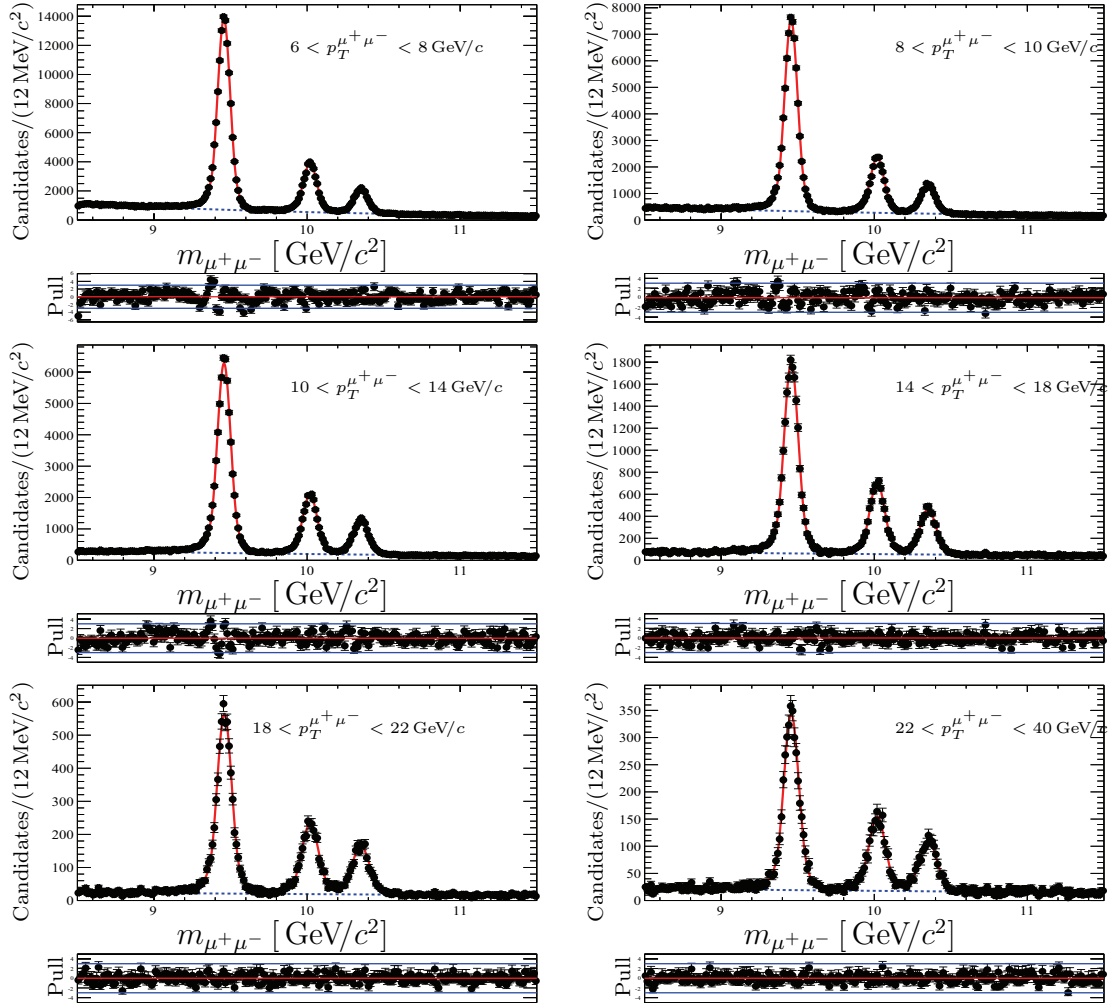


Figure A.1: $\sqrt{s} = 7 \text{ TeV}$. Distribution of the $\mu^+\mu^-$ invariant mass of the selected Υ candidates (black points) with background (dotted blue curve). Plots show the distribution in specified intervals of $\mu^+\mu^-$ transverse momentum. The bottom insert shows the pull distribution of the fit. The pull is defined as the difference between the data and fit value divided by the data error.

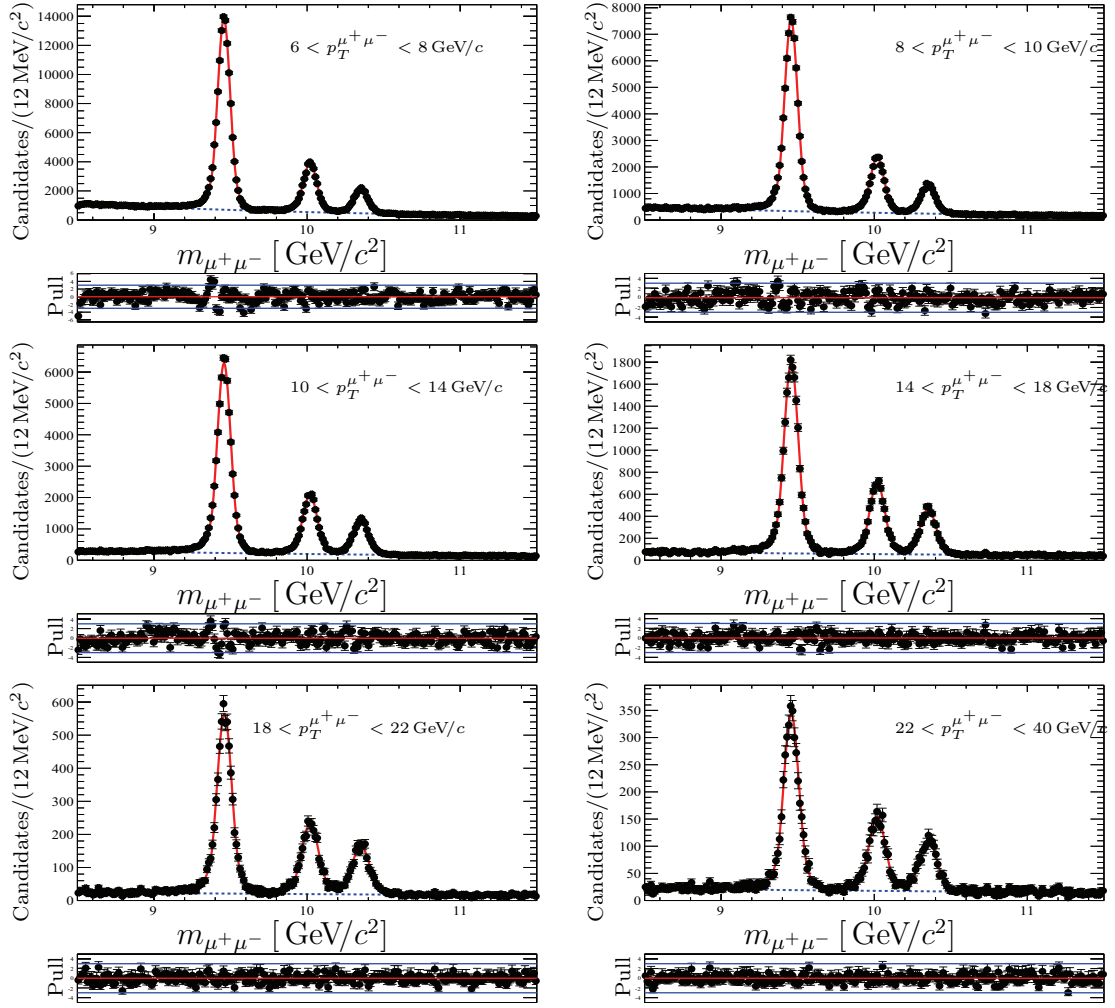


Figure A.2: $\sqrt{s} = 8$ TeV. Distribution of the $\mu^+\mu^-$ invariant mass of the selected Υ candidates (black points) with background (dotted blue curve). Plots show the distribution in specified intervals of $\mu^+\mu^-$ transverse momentum. The bottom insert shows the pull distribution of the fit. The pull is defined as the difference between the data and fit value divided by the data error.

Appendix B

Data fits for $\chi_b \rightarrow \Upsilon(1S)\gamma$ decays

 Table B.1: Data fit parameters for $\chi_{b1,2}(1, 2, 3P) \rightarrow \Upsilon(1S)\gamma$ decays

 (a) $6 < p_T^{\Upsilon(1S)} < 14 \text{ GeV}/c$

	$\Upsilon(1S)$ transverse momentum intervals, GeV/c					
	6 – 8		8 – 10		10 – 14	
	$\sqrt{s} = 7 \text{ TeV}$	$\sqrt{s} = 8 \text{ TeV}$	$\sqrt{s} = 7 \text{ TeV}$	$\sqrt{s} = 8 \text{ TeV}$	$\sqrt{s} = 7 \text{ TeV}$	$\sqrt{s} = 8 \text{ TeV}$
$N_{\chi_b(1P)}$	3590 ± 240	8100 ± 400	2800 ± 190	6520 ± 310	3140 ± 160	7970 ± 230
$N_{\chi_b(2P)}$	920 ± 190	1540 ± 290	980 ± 130	2020 ± 200	840 ± 100	1310 ± 170
$N_{\chi_b(3P)}$	—	—	—	—	250 ± 90	450 ± 150
Background	$116,200 \pm 400$	$305,500 \pm 700$	$53,580 \pm 300$	$142,000 \pm 500$	$34,810 \pm 270$	$92,300 \pm 400$
$\sigma_{\chi_{b1}(1P)}$, MeV/c^2	26.7	27.2	25.5	26.0	24.4	24.9
τ	-5.17 ± 0.13	-4.69 ± 0.08	-3.8 ± 0.4	-4.07 ± 0.27	-3.6 ± 0.8	-1.8 ± 1.0
c_0	0.3865 ± 0.0030	0.3798 ± 0.0024	0.283 ± 0.032	0.308 ± 0.018	0.21 ± 0.08	0.00 ± 0.15
c_1	0.281 ± 0.008	0.252 ± 0.005	0.21 ± 0.05	0.233 ± 0.030	0.18 ± 0.09	0.01 ± 0.12
c_2	0.524 ± 0.032	0.523 ± 0.016	0.335 ± 0.029	0.370 ± 0.017	0.28 ± 0.05	0.11 ± 0.09
c_3	0.255 ± 0.006	0.2240 ± 0.0033	0.30 ± 0.09	0.32 ± 0.06	0.26 ± 0.14	0.03 ± 0.10
c_4	0.59 ± 0.06	0.525 ± 0.026	—	—	—	—
$\chi^2/n.d.f$	0.75	1.31	1.16	1.27	1.32	1.1

 (b) $14 < p_T^{\Upsilon(1S)} < 40 \text{ GeV}/c$

	$\Upsilon(1S)$ transverse momentum intervals, GeV/c					
	14 – 18		18 – 22		22 – 40	
	$\sqrt{s} = 7 \text{ TeV}$	$\sqrt{s} = 8 \text{ TeV}$	$\sqrt{s} = 7 \text{ TeV}$	$\sqrt{s} = 8 \text{ TeV}$	$\sqrt{s} = 7 \text{ TeV}$	$\sqrt{s} = 8 \text{ TeV}$
$N_{\chi_b(1P)}$	1280 ± 60	3120 ± 110	489 ± 34	1220 ± 60	341 ± 25	800 ± 50
$N_{\chi_b(2P)}$	290 ± 40	650 ± 70	93 ± 17	174 ± 28	65 ± 12	179 ± 21
$N_{\chi_b(3P)}$	101 ± 35	150 ± 60	26 ± 11	39 ± 19	28 ± 8	48 ± 12
Background	6790 ± 110	$18,410 \pm 180$	1480 ± 50	3940 ± 80	528 ± 31	1470 ± 50
$\sigma_{\chi_{b1}(1P)}$, MeV/c^2	23.2	23.7	20.9	21.4	20.9	21.4
τ	-2.2 ± 0.7	-2.9 ± 0.4	-3.2 ± 0.9	-3.9 ± 1.5	-2.8 ± 0.6	-6.0 ± 1.0
c_0	-0.10 ± 0.17	0.05 ± 0.08	-0.17 ± 0.23	0.06 ± 0.28	-1.59 ± 0.16	0.23 ± 0.13
c_1	0.17 ± 0.06	0.24 ± 0.06	0.34 ± 0.19	1.42 ± 0.22	0.8 ± 0.4	-2.14 ± 0.19
c_2	—	—	—	—	—	—
c_3	—	—	—	—	—	—
c_4	—	—	—	—	—	—
$\chi^2/n.d.f$	1.31	0.86	0.99	1.37	1.17	1.8

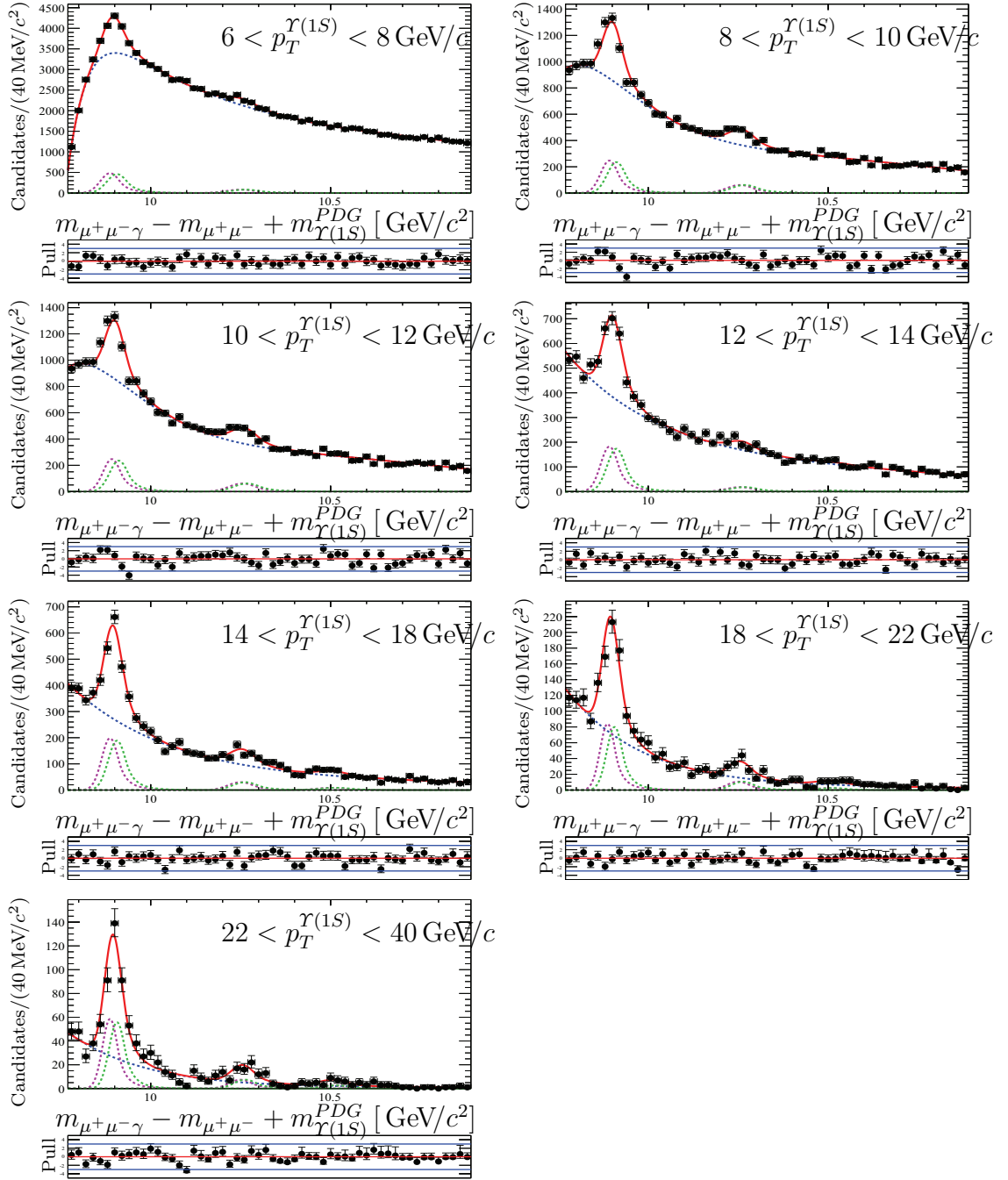


Figure B.1: $\sqrt{s} = 7$ TeV. Distribution of the mass difference $m(\mu^+\mu^-\gamma) - m(\mu^+\mu^-)$ for selected χ_b candidates (black points) together with the result of the fit (solid red curve), including the background (dotted blue curve) and the signal (dashed green and magenta curves) contributions. Green dashed curve corresponds to χ_{b1} signal and magenta dashed curve to χ_{b2} signal. Plots show the distribution in specified intervals of $\Upsilon(1S)$ transverse momentum. The bottom insert shows the pull distribution of the fit. The pull is defined as the difference between the data and fit value divided by the data error.

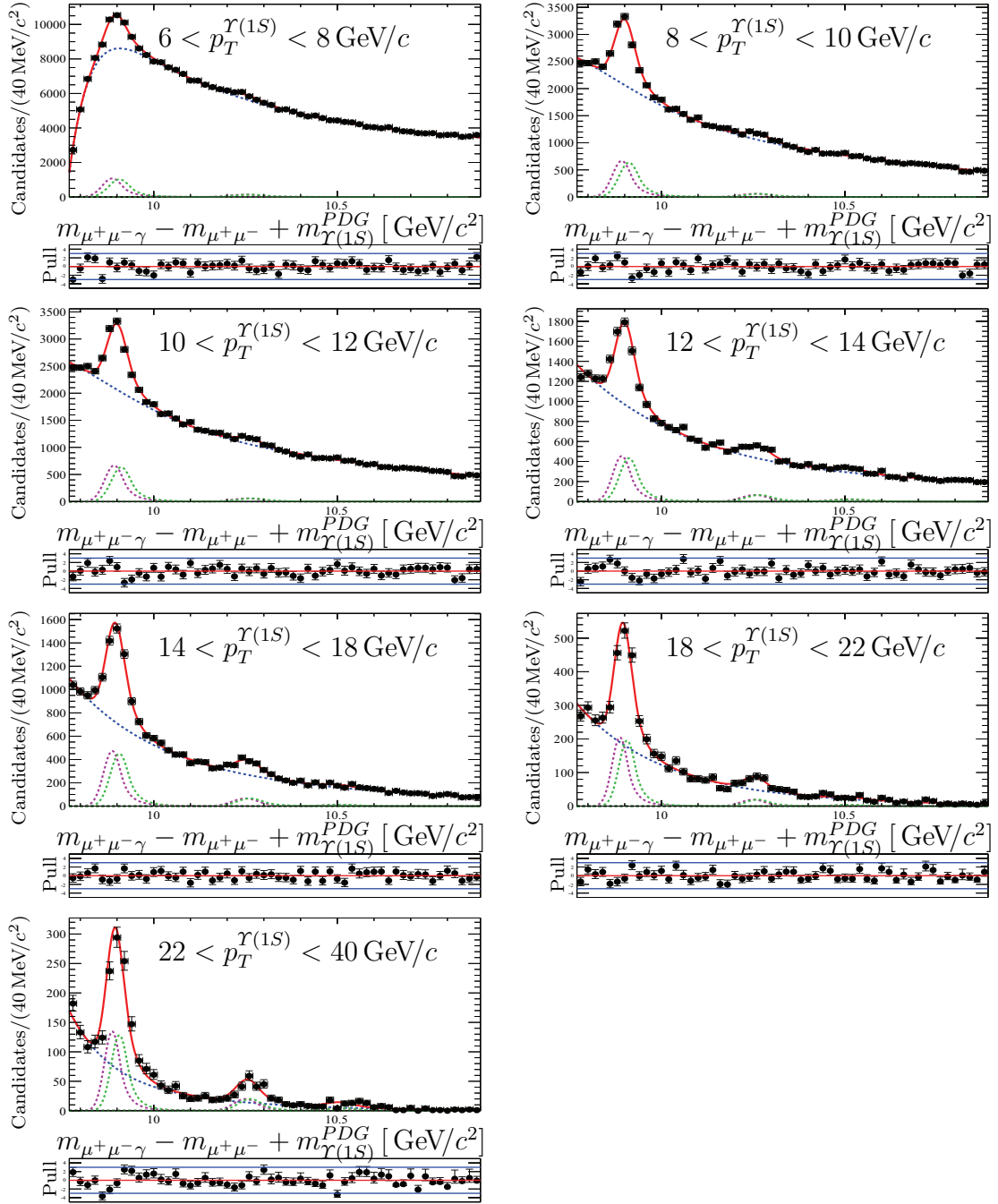


Figure B.2: $\sqrt{s} = 8$ TeV. Distribution of the mass difference $m(\mu^+\mu^-\gamma) - m(\mu^+\mu^-)$ for selected χ_b candidates (black points) together with the result of the fit (solid red curve), including the background (dotted blue curve) and the signal (dashed green and magenta curves) contributions. Green dashed curve corresponds to χ_{b1} signal and magenta dashed curve to χ_{b2} signal. Plots show the distribution in specified intervals of $\Upsilon(1S)$ transverse momentum. The bottom insert shows the pull distribution of the fit. The pull is defined as the difference between the data and fit value divided by the data error.

Appendix C

Data fits for $\chi_b \rightarrow \Upsilon(2S)\gamma$ decays

Table C.1: Data fit parameters for $\chi_{b1,2}(2,3P) \rightarrow \Upsilon(2S)\gamma$ decays

	$\Upsilon(2S)$ transverse momentum intervals, GeV/c							
	18 – 22		18 – 24		22 – 24		24 – 40	
	$\sqrt{s} = 7$ TeV	$\sqrt{s} = 8$ TeV	$\sqrt{s} = 7$ TeV	$\sqrt{s} = 8$ TeV	$\sqrt{s} = 7$ TeV	$\sqrt{s} = 8$ TeV	$\sqrt{s} = 7$ TeV	$\sqrt{s} = 8$ TeV
$N_{\chi_b(2P)}$	137 ± 22	370 ± 40	169 ± 27	450 ± 40	37 ± 12	93 ± 18	57 ± 14	208 ± 25
$N_{\chi_b(3P)}$	12 ± 14	35 ± 24	25 ± 16	58 ± 24	12 ± 6	19 ± 12	21 ± 7	21 ± 11
Background	1180 ± 40	3010 ± 70	1440 ± 50	3600 ± 70	259 ± 20	586 ± 30	399 ± 24	990 ± 40
$\sigma_{\chi_{b1}(2P)}, \text{ MeV}/c^2$	12.0	13.3	12.0	13.3	12.0	13.3	12.0	13.3
$\sigma_{\chi_{b1}(3P)}/\sigma_{\chi_{b1}(2P)}$	1.65	1.65	1.65	1.65	1.65	1.65	1.65	1.65
τ	-7.1 ± 0.9	-7.2 ± 0.5	-7.6 ± 1.2	-7.7 ± 0.5	-8.3 ± 1.7	-10.4 ± 1.1	-7.6 ± 2.1	-6.7 ± 1.6
c_0	0.524 ± 0.024	0.524 ± 0.020	0.54 ± 0.04	0.491 ± 0.011	0.45 ± 0.05	0.469 ± 0.020	0.25 ± 0.18	0.19 ± 0.15
c_1	-2.08 ± 0.12	0.20 ± 0.06	-2.10 ± 0.13	-2.14 ± 0.05	0.18 ± 0.19	-2.29 ± 0.07	-1.95 ± 0.26	-1.92 ± 0.18
c_2	0.98 ± 0.19	0.67 ± 0.18	0.78 ± 0.23	1 ± 5	-2.4 ± 0.5	-2.4 ± 3.3	-2.4 ± 0.5	0.79 ± 0.28
$\chi^2/n.d.f$	1.1	1.08	0.98	1.01	0.74	0.94	0.59	1.12

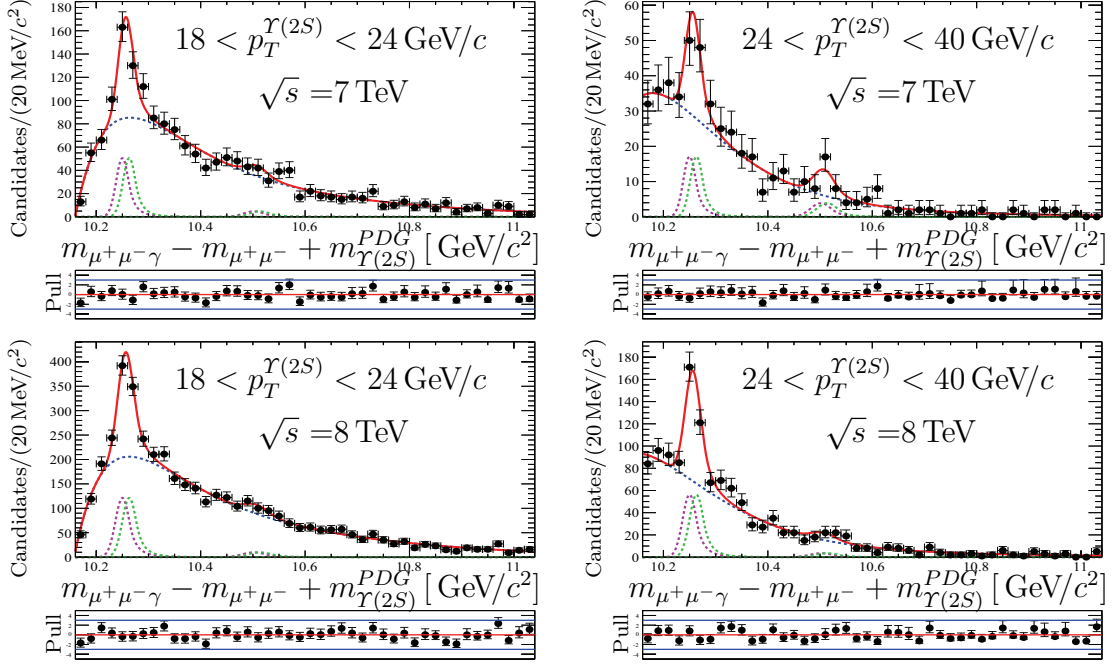


Figure C.1: Distribution of the mass difference $m(\mu^+\mu^-\gamma) - m(\mu^+\mu^-)$ for selected χ_b (2,3P) candidates (black points) together with the result of the fit (solid red curve), including the background (dotted blue curve) and the signal (dashed green and magenta curves) contributions. Green dashed curve corresponds to χ_{b1} signal and magenta dashed curve to χ_{b2} signal. Plots show the distribution in specified intervals of $\Upsilon(2S)$ transverse momentum. The bottom insert shows the pull distribution of the fit. The pull is defined as the difference between the data and fit value divided by the data error.

Appendix D

Data fits for $\chi_b \rightarrow \Upsilon(3S)\gamma$ decays

Table D.1: Data fit parameters for $\chi_{b1,2}(3P) \rightarrow \Upsilon(3S)\gamma$ decays

	$\Upsilon(3S)$ transverse momentum intervals, GeV/ c 27 – 40	
	$\sqrt{s} = 7$ TeV	$\sqrt{s} = 8$ TeV
$N_{\chi_b(3P)}$	28 ± 8	81 ± 13
Background	100 ± 11	274 ± 19
$\mu_{\chi_{b1}(3P)}$, MeV/ c^2	10,508.0	10,508.0
$\sigma_{\chi_{b1}(3P)}$, MeV/ c^2	10.0	12.0
τ	-14.39	-14.39
c_0	0.6155	0.6155
c_1	0.561	0.561
$\chi^2/n.d.f$	0.46	0.98

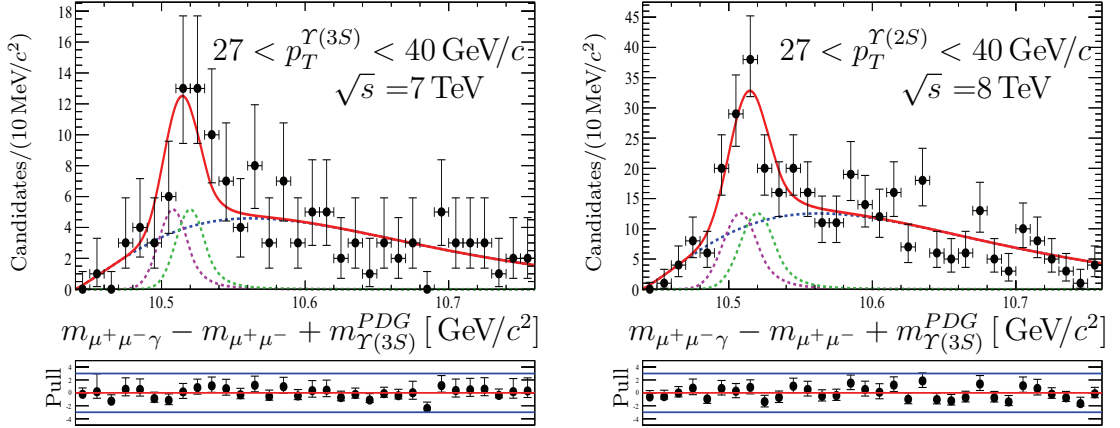


Figure D.1: Distribution of the mass difference $m(\mu^+\mu^-\gamma) - m(\mu^+\mu^-)$ for selected χ_b (3P) candidates (black points) together with the result of the fit (solid red curve), including the background (dotted blue curve) and the signal (dashed green and magenta curves) contributions. Green dashed curve corresponds to χ_{b1} signal and magenta dashed curve to χ_{b2} signal. Plots show the distribution in specified intervals of $\Upsilon(3S)$ transverse momentum. The bottom insert shows the pull distribution of the fit. The pull is defined as the difference between the data and fit value divided by the data error.

Appendix E

Simulation

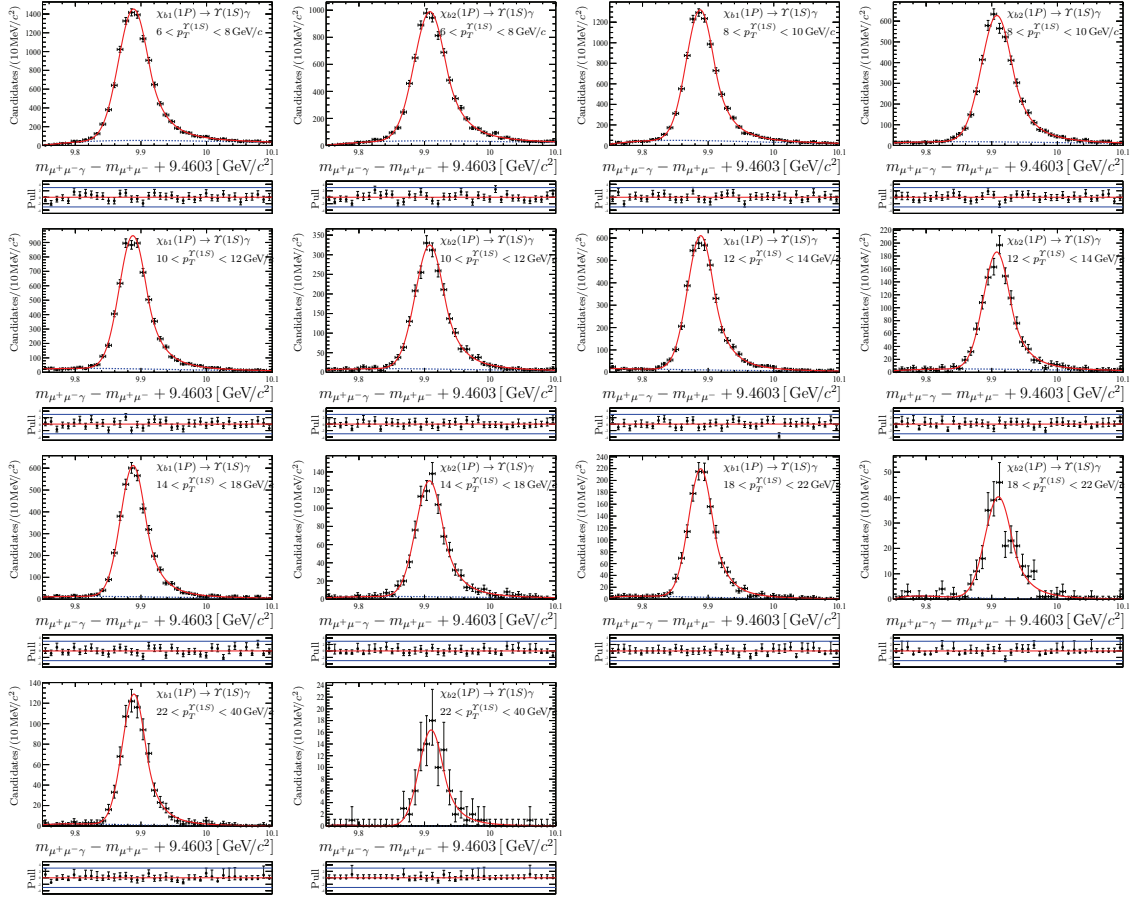


Figure E.1: Distribution of the mass difference $m(\mu^+\mu^- \gamma) - m(\mu^+\mu^-)$ for matched $\chi_{b1,2}(1P)$ candidates in $\chi_b(1P) \rightarrow \Upsilon(1S)\gamma$ decays (black points) together with the result of the fit (solid red curve), including background (dotted blue curve) contribution. Plots show the distribution in specified intervals of $\Upsilon(1S)$ transverse momentum. The bottom insert shows the pull distribution of the fit. The pull is defined as the difference between the data and fit value divided by the data error.

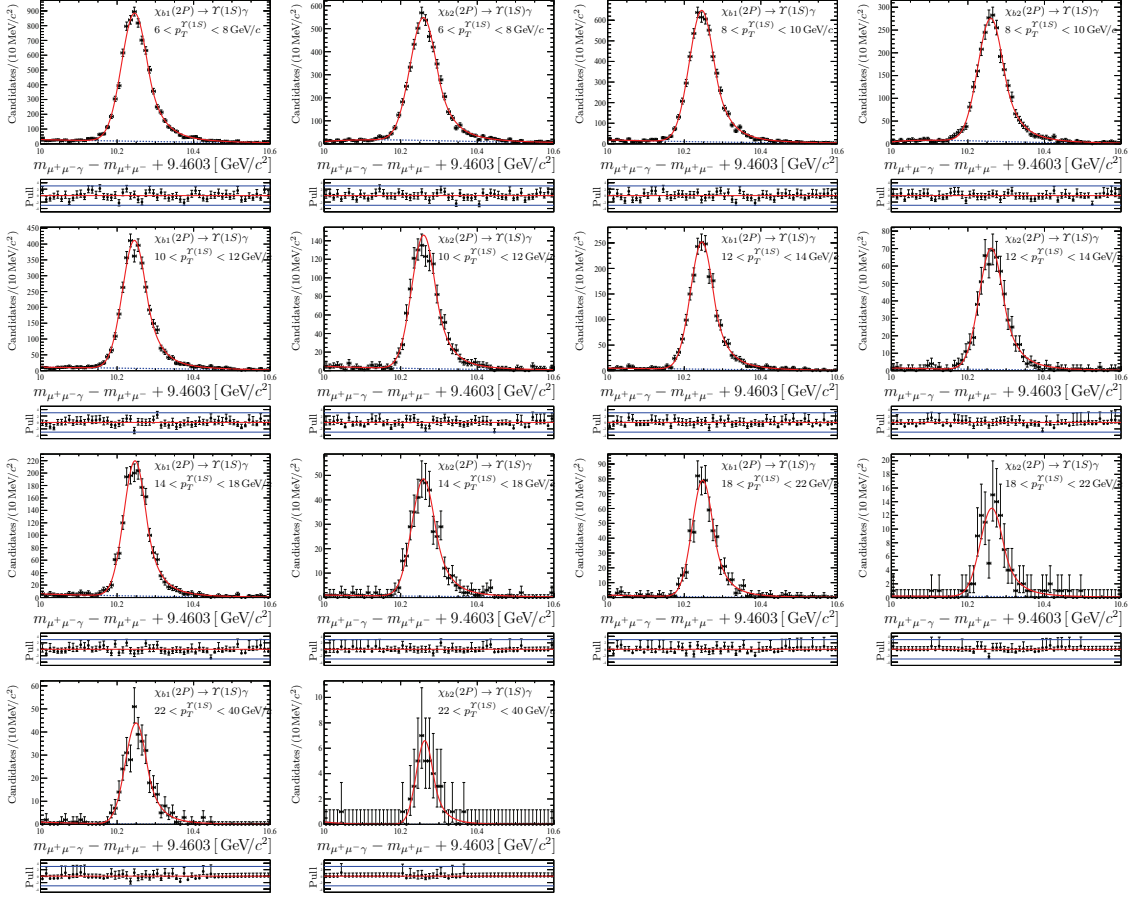


Figure E.2: Distribution of the mass difference $\mu^+\mu^-\gamma - \mu^+\mu^-$ for matched $\chi_{b1,2}(2P)$ candidates in $\chi_b(2P) \rightarrow \Upsilon(1S)\gamma$ decays (black points) together with the result of the fit (solid red curve), including background (dotted blue curve) contribution. Plots show the distribution in specified intervals of $\Upsilon(1S)$ transverse momentum. The bottom insert shows the pull distribution of the fit. The pull is defined as the difference between the data and fit value divided by the data error.

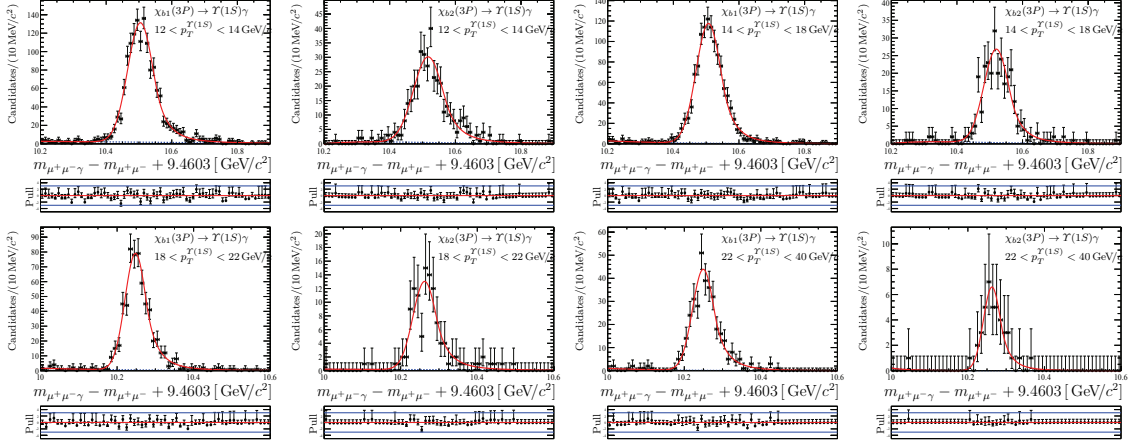


Figure E.3: Distribution of the mass difference $m_{\mu^+\mu^-\gamma} - m_{\mu^+\mu^-}$ for matched $\chi_{b1,2}(3P)$ candidates in $\chi_b(3P) \rightarrow \Upsilon(1S)\gamma$ decays (black points) together with the result of the fit (solid red curve), including background (dotted blue curve) contribution. Plots show the distribution in specified intervals of $\Upsilon(1S)$ transverse momentum. The bottom insert shows the pull distribution of the fit. The pull is defined as the difference between the data and fit value divided by the data error.

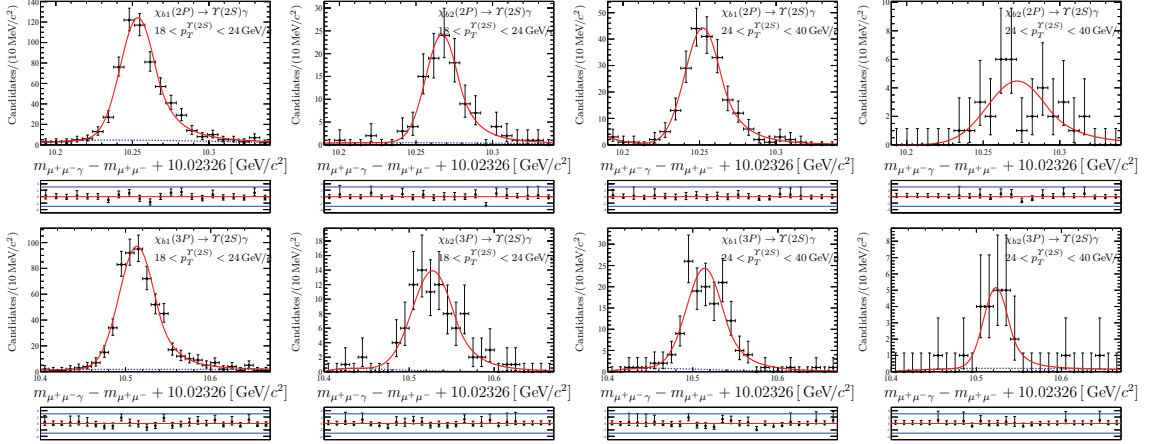


Figure E.4: Distribution of the mass difference $m_{\mu^+\mu^-\gamma} - m_{\mu^+\mu^-}$ for matched $\chi_{b1,2}(2, 3P)$ candidates in $\chi_b(2, 3P) \rightarrow \Upsilon(2S)\gamma$ decays (black points) together with the result of the fit (solid red curve), including background (dotted blue curve) contribution. Plots show the distribution in specified intervals of $\Upsilon(2S)$ transverse momentum. The bottom insert shows the pull distribution of the fit. The pull is defined as the difference between the data and fit value divided by the data error.

Table E.1: Photon reconstruction efficiency in $\chi_b(1P) \rightarrow \Upsilon(1S)\gamma$ decay

 (a) $6 < p_T^{\Upsilon(1S)} < 14 \text{ GeV}/c$

	$\Upsilon(1S)$ transverse momentum intervals, GeV/c							
	6 – 8		8 – 10		10 – 12		12 – 14	
	$\sqrt{s} = 7 \text{ TeV}$	$\sqrt{s} = 8 \text{ TeV}$	$\sqrt{s} = 7 \text{ TeV}$	$\sqrt{s} = 8 \text{ TeV}$	$\sqrt{s} = 7 \text{ TeV}$	$\sqrt{s} = 8 \text{ TeV}$	$\sqrt{s} = 7 \text{ TeV}$	$\sqrt{s} = 8 \text{ TeV}$
$N_{\chi_{b1}(1P)}^{MC}$	30,300 \pm 210	34,770 \pm 230	25,430 \pm 200	29,490 \pm 220	17,710 \pm 160	20,410 \pm 180	11,250 \pm 130	13,240 \pm 140
$N_{\Upsilon(1S)}^{MC}$ from $\chi_{b1}(1P)$	238,500 \pm 500	272,200 \pm 500	159,600 \pm 400	185,500 \pm 400	94,590 \pm 310	111,300 \pm 330	53,420 \pm 230	63,440 \pm 250
$\epsilon_{\chi_{b1}(1P)}^{\Upsilon(1S)\gamma}$, %	12.70 \pm 0.09	12.77 \pm 0.09	15.94 \pm 0.13	15.90 \pm 0.12	18.72 \pm 0.18	18.33 \pm 0.17	21.06 \pm 0.25	20.87 \pm 0.23
$N_{\chi_{b2}(1P)}^{MC}$	21,160 \pm 170	24,640 \pm 190	13,020 \pm 140	15,010 \pm 150	6580 \pm 90	7950 \pm 110	3340 \pm 70	4000 \pm 70
$N_{\Upsilon(1S)}^{MC}$ from $\chi_{b2}(1P)$	169,400 \pm 400	199,300 \pm 400	80,470 \pm 280	96,210 \pm 310	36,170 \pm 190	44,340 \pm 210	16,200 \pm 130	19,950 \pm 140
$\epsilon_{\chi_{b2}(1P)}^{\Upsilon(1S)\gamma}$, %	12.49 \pm 0.10	12.37 \pm 0.10	16.18 \pm 0.18	15.60 \pm 0.16	18.19 \pm 0.28	17.92 \pm 0.25	20.6 \pm 0.4	20.0 \pm 0.4
$\epsilon_{\chi_{b1,2}(1P)}^{\Upsilon(1S)\gamma}$, %	12.60 \pm 0.07	12.57 \pm 0.07	16.06 \pm 0.11	15.75 \pm 0.10	18.46 \pm 0.17	18.13 \pm 0.15	20.83 \pm 0.25	20.46 \pm 0.23

 (b) $14 < p_T^{\Upsilon(1S)} < 22 \text{ GeV}/c$

	$\Upsilon(1S)$ transverse momentum intervals, GeV/c							
	14 – 16		16 – 18		18 – 20		20 – 22	
	$\sqrt{s} = 7 \text{ TeV}$	$\sqrt{s} = 8 \text{ TeV}$	$\sqrt{s} = 7 \text{ TeV}$	$\sqrt{s} = 8 \text{ TeV}$	$\sqrt{s} = 7 \text{ TeV}$	$\sqrt{s} = 8 \text{ TeV}$	$\sqrt{s} = 7 \text{ TeV}$	$\sqrt{s} = 8 \text{ TeV}$
$N_{\chi_{b1}(1P)}^{MC}$	6640 \pm 90	8120 \pm 100	4030 \pm 70	4900 \pm 80	2350 \pm 50	2680 \pm 50	1370 \pm 40	1690 \pm 40
$N_{\Upsilon(1S)}^{MC}$ from $\chi_{b1}(1P)$	29,400 \pm 170	35,450 \pm 190	16,600 \pm 130	19,820 \pm 140	9160 \pm 100	11,130 \pm 110	5200 \pm 70	6390 \pm 80
$\epsilon_{\chi_{b1}(1P)}^{\Upsilon(1S)\gamma}$, %	22.61 \pm 0.34	22.90 \pm 0.32	24.3 \pm 0.5	24.7 \pm 0.4	25.7 \pm 0.6	24.1 \pm 0.5	26.4 \pm 0.8	26.4 \pm 0.8
$N_{\chi_{b2}(1P)}^{MC}$	1610 \pm 50	2040 \pm 50	813 \pm 31	1052 \pm 35	403 \pm 21	541 \pm 26	245 \pm 16	312 \pm 18
$N_{\Upsilon(1S)}^{MC}$ from $\chi_{b2}(1P)$	7350 \pm 90	9340 \pm 100	3440 \pm 60	4480 \pm 70	1830 \pm 40	2130 \pm 50	915 \pm 30	1162 \pm 34
$\epsilon_{\chi_{b2}(1P)}^{\Upsilon(1S)\gamma}$, %	22.0 \pm 0.7	21.9 \pm 0.6	23.6 \pm 1.0	23.5 \pm 0.9	22.0 \pm 1.3	25.4 \pm 1.3	26.7 \pm 2.0	26.9 \pm 1.8
$\epsilon_{\chi_{b1,2}(1P)}^{\Upsilon(1S)\gamma}$, %	22.3 \pm 0.4	22.38 \pm 0.33	23.9 \pm 0.5	24.1 \pm 0.5	23.8 \pm 0.7	24.7 \pm 0.7	26.6 \pm 1.1	26.7 \pm 1.0

 (c) $22 < p_T^{\Upsilon(1S)} < 40 \text{ GeV}/c$

	$\Upsilon(1S)$ transverse momentum intervals, GeV/c			
	22 – 28		28 – 40	
	$\sqrt{s} = 7 \text{ TeV}$	$\sqrt{s} = 8 \text{ TeV}$	$\sqrt{s} = 7 \text{ TeV}$	$\sqrt{s} = 8 \text{ TeV}$
$N_{\chi_{b1}(1P)}^{MC}$	1620 \pm 40	1960 \pm 50	440 \pm 21	555 \pm 24
$N_{\Upsilon(1S)}^{MC}$ from $\chi_{b1}(1P)$	6070 \pm 80	7390 \pm 90	1730 \pm 40	2120 \pm 50
$\epsilon_{\chi_{b1}(1P)}^{\Upsilon(1S)\gamma}$, %	26.6 \pm 0.8	26.5 \pm 0.7	25.4 \pm 1.4	26.2 \pm 1.3
$N_{\chi_{b2}(1P)}^{MC}$	237 \pm 16	280 \pm 18	63 \pm 8	74 \pm 10
$N_{\Upsilon(1S)}^{MC}$ from $\chi_{b2}(1P)$	877 \pm 30	1113 \pm 33	233 \pm 15	286 \pm 17
$\epsilon_{\chi_{b2}(1P)}^{\Upsilon(1S)\gamma}$, %	27.0 \pm 2.0	25.1 \pm 1.8	27 \pm 4	26 \pm 4
$\epsilon_{\chi_{b1,2}(1P)}^{\Upsilon(1S)\gamma}$, %	26.8 \pm 1.1	25.8 \pm 1.0	26.2 \pm 2.0	26.1 \pm 2.0

Table E.2: Photon reconstruction efficiency in $\chi_b(2P) \rightarrow \Upsilon(1S)\gamma$ decay

 (a) $6 < p_T^{\Upsilon(1S)} < 14 \text{ GeV}/c$

	$\Upsilon(1S)$ transverse momentum intervals, GeV/c							
	6 – 8		8 – 10		10 – 12		12 – 14	
	$\sqrt{s} = 7 \text{ TeV}$	$\sqrt{s} = 8 \text{ TeV}$	$\sqrt{s} = 7 \text{ TeV}$	$\sqrt{s} = 8 \text{ TeV}$	$\sqrt{s} = 7 \text{ TeV}$	$\sqrt{s} = 8 \text{ TeV}$	$\sqrt{s} = 7 \text{ TeV}$	$\sqrt{s} = 8 \text{ TeV}$
$N_{\chi_{b1}(2P)}^{MC}$	39,390 ± 230	34,350 ± 230	27,970 ± 190	24,580 ± 170	17,190 ± 140	15,460 ± 140	10,150 ± 110	9030 ± 110
$N_{\Upsilon(1S)}^{MC}$ from $\chi_{b1}(2P)$	192,700 ± 400	171,900 ± 400	128,800 ± 400	115,550 ± 340	76,370 ± 280	69,830 ± 260	43,290 ± 210	39,640 ± 200
$\epsilon_{\chi_{b1}(2P)}^{\Upsilon(1S)\gamma}, \%$	20.44 ± 0.13	19.98 ± 0.14	21.71 ± 0.16	21.27 ± 0.16	22.51 ± 0.20	22.14 ± 0.22	23.44 ± 0.28	22.79 ± 0.29
$N_{\chi_{b2}(2P)}^{MC}$	35,400 ± 210	29,330 ± 210	17,340 ± 140	14,710 ± 150	8430 ± 100	6990 ± 100	3880 ± 70	3330 ± 70
$N_{\Upsilon(1S)}^{MC}$ from $\chi_{b2}(2P)$	190,000 ± 400	161,400 ± 400	88,190 ± 300	76,220 ± 280	39,680 ± 200	34,670 ± 190	17,840 ± 130	15,770 ± 130
$\epsilon_{\chi_{b2}(2P)}^{\Upsilon(1S)\gamma}, \%$	18.63 ± 0.12	18.17 ± 0.14	19.66 ± 0.18	19.30 ± 0.21	21.25 ± 0.28	20.17 ± 0.31	21.7 ± 0.4	21.1 ± 0.5
$\epsilon_{\chi_{b1,2}(2P)}^{\Upsilon(1S)\gamma}, \%$	19.54 ± 0.09	19.08 ± 0.10	20.69 ± 0.12	20.29 ± 0.13	21.88 ± 0.17	21.16 ± 0.19	22.58 ± 0.25	21.96 ± 0.27

 (b) $14 < p_T^{\Upsilon(1S)} < 22 \text{ GeV}/c$

	$\Upsilon(1S)$ transverse momentum intervals, GeV/c							
	14 – 16		16 – 18		18 – 20		20 – 22	
	$\sqrt{s} = 7 \text{ TeV}$	$\sqrt{s} = 8 \text{ TeV}$	$\sqrt{s} = 7 \text{ TeV}$	$\sqrt{s} = 8 \text{ TeV}$	$\sqrt{s} = 7 \text{ TeV}$	$\sqrt{s} = 8 \text{ TeV}$	$\sqrt{s} = 7 \text{ TeV}$	$\sqrt{s} = 8 \text{ TeV}$
$N_{\chi_{b1}(2P)}^{MC}$	5590 ± 90	5260 ± 80	3190 ± 60	2900 ± 60	1760 ± 50	1670 ± 40	1057 ± 35	971 ± 32
$N_{\Upsilon(1S)}^{MC}$ from $\chi_{b1}(2P)$	23,920 ± 150	22,030 ± 150	13,150 ± 110	12,200 ± 110	7560 ± 90	7000 ± 80	4240 ± 70	4060 ± 60
$\epsilon_{\chi_{b1}(2P)}^{\Upsilon(1S)\gamma}, \%$	23.4 ± 0.4	23.9 ± 0.4	24.3 ± 0.5	23.8 ± 0.5	23.3 ± 0.7	23.9 ± 0.7	24.9 ± 0.9	23.9 ± 0.9
$N_{\chi_{b2}(2P)}^{MC}$	1830 ± 40	1570 ± 50	854 ± 31	794 ± 30	456 ± 22	378 ± 20	225 ± 15	191 ± 15
$N_{\Upsilon(1S)}^{MC}$ from $\chi_{b2}(2P)$	8020 ± 90	7170 ± 80	3780 ± 60	3440 ± 60	1950 ± 40	1690 ± 40	972 ± 31	881 ± 30
$\epsilon_{\chi_{b2}(2P)}^{\Upsilon(1S)\gamma}, \%$	22.8 ± 0.6	21.9 ± 0.8	22.6 ± 0.9	23.1 ± 0.9	23.4 ± 1.3	22.3 ± 1.3	23.2 ± 1.7	21.7 ± 1.8
$\epsilon_{\chi_{b1,2}(2P)}^{\Upsilon(1S)\gamma}, \%$	23.1 ± 0.4	22.9 ± 0.4	23.5 ± 0.5	23.4 ± 0.5	23.4 ± 0.7	23.1 ± 0.7	24.0 ± 1.0	22.8 ± 1.0

 (c) $22 < p_T^{\Upsilon(1S)} < 40 \text{ GeV}/c$

	$\Upsilon(1S)$ transverse momentum intervals, GeV/c			
	22 – 28		28 – 40	
	$\sqrt{s} = 7 \text{ TeV}$	$\sqrt{s} = 8 \text{ TeV}$	$\sqrt{s} = 7 \text{ TeV}$	$\sqrt{s} = 8 \text{ TeV}$
$N_{\chi_{b1}(2P)}^{MC}$	1156 ± 35	1044 ± 34	363 ± 19	301 ± 18
$N_{\Upsilon(1S)}^{MC}$ from $\chi_{b1}(2P)$	4780 ± 70	4560 ± 70	1480 ± 40	1310 ± 40
$\epsilon_{\chi_{b1}(2P)}^{\Upsilon(1S)\gamma}, \%$	24.2 ± 0.8	22.9 ± 0.8	24.6 ± 1.4	22.9 ± 1.5
$N_{\chi_{b2}(2P)}^{MC}$	212 ± 15	184 ± 14	53 ± 8	48 ± 7
$N_{\Upsilon(1S)}^{MC}$ from $\chi_{b2}(2P)$	929 ± 30	846 ± 29	219 ± 15	217 ± 15
$\epsilon_{\chi_{b2}(2P)}^{\Upsilon(1S)\gamma}, \%$	22.8 ± 1.8	21.7 ± 1.8	24 ± 4	22.1 ± 3.5
$\epsilon_{\chi_{b1,2}(2P)}^{\Upsilon(1S)\gamma}, \%$	23.5 ± 1.0	22.3 ± 1.0	24.4 ± 2.1	22.5 ± 1.9

Table E.3: Photon reconstruction efficiency in $\chi_b(3P) \rightarrow \Upsilon(1S)\gamma$ decay

 (a) $6 < p_T^{\Upsilon(1S)} < 14 \text{ GeV}/c$

	$\Upsilon(1S)$ transverse momentum intervals, GeV/c							
	6 – 8		8 – 10		10 – 12		12 – 14	
	$\sqrt{s}=7 \text{ TeV}$	$\sqrt{s}=8 \text{ TeV}$	$\sqrt{s}=7 \text{ TeV}$	$\sqrt{s}=8 \text{ TeV}$	$\sqrt{s}=7 \text{ TeV}$	$\sqrt{s}=8 \text{ TeV}$	$\sqrt{s}=7 \text{ TeV}$	$\sqrt{s}=8 \text{ TeV}$
$N_{\chi_{b1}(3P)}^{MC}$	27,600 ± 190	24,190 ± 180	18,840 ± 150	16,410 ± 140	11,230 ± 120	9960 ± 110	6340 ± 80	5800 ± 80
$N_{\Upsilon(1S)}^{MC}$ from $\chi_{b1}(3P)$	129,000 ± 400	113,810 ± 340	85,400 ± 290	75,680 ± 280	50,740 ± 230	45,560 ± 210	28,340 ± 170	25,960 ± 160
$\epsilon_{\chi_{b1}(3P)}^{\Upsilon(1S)\gamma}$, %	21.40 ± 0.16	21.26 ± 0.17	22.06 ± 0.19	21.68 ± 0.21	22.13 ± 0.26	21.87 ± 0.26	22.38 ± 0.32	22.32 ± 0.35
$N_{\chi_{b2}(3P)}^{MC}$	23,780 ± 180	21,120 ± 170	11,580 ± 120	10,410 ± 120	5100 ± 80	4790 ± 80	2390 ± 50	2190 ± 50
$N_{\Upsilon(1S)}^{MC}$ from $\chi_{b2}(3P)$	125,250 ± 350	114,160 ± 340	58,730 ± 240	54,100 ± 230	25,650 ± 160	23,960 ± 150	11,530 ± 110	10,970 ± 100
$\epsilon_{\chi_{b2}(3P)}^{\Upsilon(1S)\gamma}$, %	18.99 ± 0.15	18.50 ± 0.16	19.72 ± 0.22	19.25 ± 0.23	19.88 ± 0.33	19.98 ± 0.35	20.8 ± 0.5	20.0 ± 0.5
$\epsilon_{\chi_{b1,2}(3P)}^{\Upsilon(1S)\gamma}$, %	20.19 ± 0.11	19.88 ± 0.12	20.89 ± 0.14	20.46 ± 0.15	21.00 ± 0.21	20.92 ± 0.22	21.58 ± 0.30	21.14 ± 0.31

 (b) $14 < p_T^{\Upsilon(1S)} < 22 \text{ GeV}/c$

	$\Upsilon(1S)$ transverse momentum intervals, GeV/c							
	14 – 16		16 – 18		18 – 20		20 – 22	
	$\sqrt{s}=7 \text{ TeV}$	$\sqrt{s}=8 \text{ TeV}$	$\sqrt{s}=7 \text{ TeV}$	$\sqrt{s}=8 \text{ TeV}$	$\sqrt{s}=7 \text{ TeV}$	$\sqrt{s}=8 \text{ TeV}$	$\sqrt{s}=7 \text{ TeV}$	$\sqrt{s}=8 \text{ TeV}$
$N_{\chi_{b1}(3P)}^{MC}$	3690 ± 60	3260 ± 60	1970 ± 50	1860 ± 50	1063 ± 34	1005 ± 33	682 ± 26	596 ± 25
$N_{\Upsilon(1S)}^{MC}$ from $\chi_{b1}(3P)$	15,730 ± 130	14,750 ± 120	8640 ± 90	8170 ± 90	4740 ± 70	4530 ± 70	2880 ± 50	2640 ± 50
$\epsilon_{\chi_{b1}(3P)}^{\Upsilon(1S)\gamma}$, %	23.5 ± 0.5	22.1 ± 0.5	22.8 ± 0.6	22.8 ± 0.6	22.4 ± 0.8	22.2 ± 0.8	23.7 ± 1.0	22.5 ± 1.0
$N_{\chi_{b2}(3P)}^{MC}$	1140 ± 40	1043 ± 35	523 ± 24	506 ± 22	273 ± 17	233 ± 16	126 ± 12	125 ± 11
$N_{\Upsilon(1S)}^{MC}$ from $\chi_{b2}(3P)$	5250 ± 70	5000 ± 70	2450 ± 50	2420 ± 50	1251 ± 35	1250 ± 35	679 ± 26	600 ± 24
$\epsilon_{\chi_{b2}(3P)}^{\Upsilon(1S)\gamma}$, %	21.6 ± 0.8	20.9 ± 0.8	21.3 ± 1.1	20.9 ± 1.0	21.8 ± 1.5	18.6 ± 1.4	18.6 ± 1.9	20.9 ± 2.1
$\epsilon_{\chi_{b1,2}(3P)}^{\Upsilon(1S)\gamma}$, %	22.5 ± 0.4	21.5 ± 0.4	22.1 ± 0.6	21.8 ± 0.6	22.1 ± 0.8	20.4 ± 0.8	21.2 ± 1.1	21.7 ± 1.2

 (c) $22 < p_T^{\Upsilon(1S)} < 40 \text{ GeV}/c$

	$\Upsilon(1S)$ transverse momentum intervals, GeV/c			
	22 – 28		28 – 40	
	$\sqrt{s}=7 \text{ TeV}$	$\sqrt{s}=8 \text{ TeV}$	$\sqrt{s}=7 \text{ TeV}$	$\sqrt{s}=8 \text{ TeV}$
$N_{\chi_{b1}(3P)}^{MC}$	732 ± 27	706 ± 27	193 ± 14	170 ± 13
$N_{\Upsilon(1S)}^{MC}$ from $\chi_{b1}(3P)$	3190 ± 60	3120 ± 60	903 ± 30	851 ± 29
$\epsilon_{\chi_{b1}(3P)}^{\Upsilon(1S)\gamma}$, %	23.0 ± 0.9	22.7 ± 1.0	21.4 ± 1.7	20.0 ± 1.7
$N_{\chi_{b2}(3P)}^{MC}$	119 ± 11	139 ± 12	31 ± 6	32 ± 6
$N_{\Upsilon(1S)}^{MC}$ from $\chi_{b2}(3P)$	608 ± 25	659 ± 26	142 ± 12	147 ± 12
$\epsilon_{\chi_{b2}(3P)}^{\Upsilon(1S)\gamma}$, %	19.6 ± 2.0	21.1 ± 2.0	22 ± 4	22 ± 4
$\epsilon_{\chi_{b1,2}(3P)}^{\Upsilon(1S)\gamma}$, %	21.3 ± 1.1	21.9 ± 1.1	21.4 ± 2.3	20.9 ± 2.3

Table E.4: Photon reconstruction efficiency in $\chi_b(2P) \rightarrow \Upsilon(2S)\gamma$ decay

(a) $14 < p_T^{\Upsilon(2S)} < 22 \text{ GeV}/c$

	$\Upsilon(2S)$ transverse momentum intervals, GeV/c							
	14 – 16		16 – 18		18 – 20		20 – 22	
	$\sqrt{s}=7 \text{ TeV}$	$\sqrt{s}=8 \text{ TeV}$	$\sqrt{s}=7 \text{ TeV}$	$\sqrt{s}=8 \text{ TeV}$	$\sqrt{s}=7 \text{ TeV}$	$\sqrt{s}=8 \text{ TeV}$	$\sqrt{s}=7 \text{ TeV}$	$\sqrt{s}=8 \text{ TeV}$
$N_{\chi_{b1}(2P)}^{MC}$	2810 ± 60	2580 ± 60	2100 ± 60	2000 ± 60	1360 ± 50	1410 ± 50	900 ± 40	910 ± 40
$N_{\Upsilon(2S)}^{MC}$ from $\chi_{b1}(2P)$	28,130 ± 170	26,010 ± 160	16,320 ± 130	15,030 ± 120	9040 ± 100	8770 ± 90	5310 ± 70	4980 ± 70
$\epsilon_{\chi_{b1}(2P)}^\gamma, \%$	10.00 ± 0.23	9.93 ± 0.24	12.9 ± 0.4	13.3 ± 0.4	15.1 ± 0.6	16.1 ± 0.6	17.0 ± 0.8	18.3 ± 0.9
$N_{\chi_{b2}(2P)}^{MC}$	1130 ± 40	1010 ± 40	640 ± 40	636 ± 33	433 ± 30	341 ± 24	255 ± 19	200 ± 19
$N_{\Upsilon(2S)}^{MC}$ from $\chi_{b2}(2P)$	10,340 ± 100	9200 ± 100	5000 ± 70	4480 ± 70	2450 ± 50	2170 ± 50	1320 ± 40	1157 ± 34
$\epsilon_{\chi_{b2}(2P)}^\gamma, \%$	10.9 ± 0.4	10.9 ± 0.5	12.9 ± 0.7	14.2 ± 0.8	17.7 ± 1.3	15.7 ± 1.1	19.3 ± 1.5	17.3 ± 1.7
$\epsilon_{\chi_{b1,2}(2P)}^\gamma, \%$	10.46 ± 0.24	10.43 ± 0.26	12.9 ± 0.4	13.7 ± 0.4	16.4 ± 0.7	15.9 ± 0.7	18.2 ± 0.9	17.8 ± 1.0

(b) $22 < p_T^{\Upsilon(2S)} < 40 \text{ GeV}/c$

	$\Upsilon(2S)$ transverse momentum intervals, GeV/c					
	22 – 24		24 – 26		26 – 40	
	$\sqrt{s}=7 \text{ TeV}$	$\sqrt{s}=8 \text{ TeV}$	$\sqrt{s}=7 \text{ TeV}$	$\sqrt{s}=8 \text{ TeV}$	$\sqrt{s}=7 \text{ TeV}$	$\sqrt{s}=8 \text{ TeV}$
$N_{\chi_{b1}(2P)}^{MC}$	608 ± 35	589 ± 35	378 ± 23	373 ± 29	663 ± 28	653 ± 33
$N_{\Upsilon(2S)}^{MC}$ from $\chi_{b1}(2P)$	3240 ± 60	3100 ± 60	1810 ± 40	1810 ± 40	3040 ± 60	2900 ± 50
$\epsilon_{\chi_{b1}(2P)}^\gamma, \%$	18.8 ± 1.1	19.0 ± 1.2	20.9 ± 1.3	20.7 ± 1.7	21.8 ± 1.0	22.6 ± 1.2
$N_{\chi_{b2}(2P)}^{MC}$	121 ± 13	128 ± 14	76 ± 11	68 ± 13	108 ± 16	134 ± 12
$N_{\Upsilon(2S)}^{MC}$ from $\chi_{b2}(2P)$	665 ± 26	605 ± 25	384 ± 20	323 ± 18	532 ± 23	505 ± 22
$\epsilon_{\chi_{b2}(2P)}^\gamma, \%$	18.2 ± 2.1	21.2 ± 2.5	19.9 ± 3.0	21 ± 4	20.4 ± 3.1	26.4 ± 2.6
$\epsilon_{\chi_{b1,2}(2P)}^\gamma, \%$	18.5 ± 1.2	20.1 ± 1.4	20.4 ± 1.6	20.8 ± 2.3	21.1 ± 1.6	24.5 ± 1.4

 Table E.5: Photon reconstruction efficiency in $\chi_b(3P) \rightarrow \Upsilon(2S)\gamma$ decay

(a) $14 < p_T^{\Upsilon(2S)} < 22 \text{ GeV}/c$

	$\Upsilon(2S)$ transverse momentum intervals, GeV/c							
	14 – 16		16 – 18		18 – 20		20 – 22	
	$\sqrt{s}=7 \text{ TeV}$	$\sqrt{s}=8 \text{ TeV}$	$\sqrt{s}=7 \text{ TeV}$	$\sqrt{s}=8 \text{ TeV}$	$\sqrt{s}=7 \text{ TeV}$	$\sqrt{s}=8 \text{ TeV}$	$\sqrt{s}=7 \text{ TeV}$	$\sqrt{s}=8 \text{ TeV}$
$N_{\chi_{b1}(3P)}^{MC}$	3850 ± 110	3690 ± 80	2170 ± 60	2000 ± 60	1400 ± 50	1280 ± 50	820 ± 40	694 ± 33
$N_{\Upsilon(2S)}^{MC}$ from $\chi_{b1}(3P)$	18,500 ± 140	17,380 ± 130	10,400 ± 100	9720 ± 100	6090 ± 80	5600 ± 70	3550 ± 60	3300 ± 60
$\epsilon_{\chi_{b1}(3P)}^\gamma, \%$	20.8 ± 0.6	21.2 ± 0.5	20.9 ± 0.6	20.6 ± 0.7	23.0 ± 0.9	22.8 ± 0.9	23.1 ± 1.1	21.0 ± 1.1
$N_{\chi_{b2}(3P)}^{MC}$	1350 ± 60	1160 ± 40	675 ± 31	597 ± 32	336 ± 20	324 ± 18	185 ± 15	183 ± 17
$N_{\Upsilon(2S)}^{MC}$ from $\chi_{b2}(3P)$	6540 ± 80	6210 ± 80	3160 ± 60	2980 ± 50	1590 ± 40	1570 ± 40	862 ± 29	840 ± 29
$\epsilon_{\chi_{b2}(3P)}^\gamma, \%$	20.6 ± 1.0	18.7 ± 0.8	21.3 ± 1.1	20.1 ± 1.1	21.1 ± 1.4	20.7 ± 1.3	21.4 ± 1.9	21.8 ± 2.1
$\epsilon_{\chi_{b1,2}(3P)}^\gamma, \%$	20.7 ± 0.6	20.0 ± 0.5	21.1 ± 0.6	20.3 ± 0.7	22.0 ± 0.8	21.7 ± 0.8	22.3 ± 1.1	21.4 ± 1.2

(b) $22 < p_T^{\Upsilon(2S)} < 40 \text{ GeV}/c$

	$\Upsilon(2S)$ transverse momentum intervals, GeV/c					
	22 – 24		24 – 26		26 – 40	
	$\sqrt{s}=7 \text{ TeV}$	$\sqrt{s}=8 \text{ TeV}$	$\sqrt{s}=7 \text{ TeV}$	$\sqrt{s}=8 \text{ TeV}$	$\sqrt{s}=7 \text{ TeV}$	$\sqrt{s}=8 \text{ TeV}$
$N_{\chi_{b1}(3P)}^{MC}$	468 ± 26	436 ± 25	292 ± 19	270 ± 17	444 ± 23	455 ± 23
$N_{\Upsilon(2S)}^{MC}$ from $\chi_{b1}(3P)$	2090 ± 50	1910 ± 40	1230 ± 35	1102 ± 33	1910 ± 40	1890 ± 40
$\epsilon_{\chi_{b1}(3P)}^\gamma, \%$	22.4 ± 1.4	22.9 ± 1.4	23.8 ± 1.7	24.5 ± 1.7	23.2 ± 1.3	24.0 ± 1.3
$N_{\chi_{b2}(3P)}^{MC}$	117 ± 11	112 ± 12	44 ± 8	58 ± 8	73 ± 9	76 ± 9
$N_{\Upsilon(2S)}^{MC}$ from $\chi_{b2}(3P)$	447 ± 21	481 ± 22	253 ± 16	208 ± 14	361 ± 19	327 ± 18
$\epsilon_{\chi_{b2}(3P)}^\gamma, \%$	26.2 ± 2.8	23.4 ± 2.7	17.4 ± 3.2	28 ± 4	20.1 ± 2.7	23.2 ± 3.0
$\epsilon_{\chi_{b1,2}(3P)}^\gamma, \%$	24.3 ± 1.6	23.1 ± 1.5	20.6 ± 1.8	26.2 ± 2.2	21.7 ± 1.5	23.6 ± 1.6

Table E.6: Photon reconstruction efficiency in $\chi_b(3P) \rightarrow \Upsilon(3S)\gamma$ decay

	$\Upsilon(3S)$ transverse momentum intervals, GeV/c							
	18 - 20		20 - 22		22 - 28		28 - 40	
	$\sqrt{s} = 7$ TeV	$\sqrt{s} = 8$ TeV	$\sqrt{s} = 7$ TeV	$\sqrt{s} = 8$ TeV	$\sqrt{s} = 7$ TeV	$\sqrt{s} = 8$ TeV	$\sqrt{s} = 7$ TeV	$\sqrt{s} = 8$ TeV
$N_{\chi_{b1}(3P)}^{MC}$	180 ± 16	141 ± 14	261 ± 17	218 ± 16	210 ± 15	173 ± 14	237 ± 17	256 ± 17
$N_{\Upsilon(3S)}^{MC}$ from $\chi_{b1}(3P)$	6770 ± 80	6320 ± 80	4080 ± 60	3800 ± 60	1530 ± 40	1390 ± 40	1490 ± 40	1390 ± 40
$\varepsilon_{\chi_{b1}(3P)}^\gamma, \%$	2.65 ± 0.24	2.24 ± 0.22	6.4 ± 0.4	5.7 ± 0.4	13.8 ± 1.0	12.4 ± 1.1	15.9 ± 1.2	18.4 ± 1.3
$N_{\chi_{b2}(3P)}^{MC}$	85 ± 10	80 ± 10	63 ± 9	74 ± 9	43 ± 7	28 ± 6	44 ± 7	36 ± 6
$N_{\Upsilon(3S)}^{MC}$ from $\chi_{b2}(3P)$	1770 ± 40	1820 ± 40	970 ± 31	969 ± 31	322 ± 18	285 ± 17	243 ± 16	215 ± 15
$\varepsilon_{\chi_{b2}(3P)}^\gamma, \%$	4.8 ± 0.6	4.4 ± 0.5	6.5 ± 0.9	7.6 ± 1.0	13.2 ± 2.4	9.8 ± 2.1	18.0 ± 3.1	16.9 ± 3.2
$\varepsilon_{\chi_{b1,2}(3P)}^\gamma, \%$	3.73 ± 0.32	3.32 ± 0.29	6.4 ± 0.5	6.7 ± 0.5	13.5 ± 1.3	11.1 ± 1.2	17.0 ± 1.7	17.6 ± 1.7

Bibliography

- [1] S. Herb *et al.*, *Observation of a Dimuon Resonance at 9.5-GeV in 400-GeV Proton-Nucleus Collisions*, *Phys. Rev. Lett.* **39** (1977) 252.
- [2] M. Kobayashi and T. Maskawa, *CP Violation in the Renormalizable Theory of Weak Interaction*, *Prog. Theor. Phys.* **49** (1973) 652.
- [3] ARGUS Collaboration, H. Albrecht *et al.*, *Reconstruction of B Mesons*, *Phys. Lett.* **B185** (1987) 218.
- [4] CLEO Collaboration, C. Bebek *et al.*, *Exclusive Decays and Masses of the B Mesons*, *Phys. Rev.* **D36** (1987) 1289.
- [5] R. Dowdall, *B and bottomonium spectroscopy from lattice NRQCD with charm in the sea*, PoS **Lattice2011** (2011) 118, [arXiv:1111.0449](https://arxiv.org/abs/1111.0449).
- [6] R. Dowdall, C. Davies, T. Hammant, and R. Horgan, *Precise heavy-light meson masses and hyperfine splittings from lattice QCD including charm quarks in the sea*, *Phys. Rev.* **D86** (2012) 094510, [arXiv:1207.5149](https://arxiv.org/abs/1207.5149).
- [7] D. S. Kulshreshtha, *The fine and hyperfine structure and dipole transitions of charmonium and bottomonium in the two step potential model*, *Nuovo Cim.* **A87** (1985) 25.
- [8] A. Parmar, B. Patel, and P. C. Vinodkumar, *Two-Photon, Two-gluon and Radiative Decays of Heavy Flavoured Mesons*, *Nucl. Phys.* **A848** (2010) 299, [arXiv:1001.0848](https://arxiv.org/abs/1001.0848).

- [9] S. W. Herb *et al.*, *P-wave and d-wave masses of bottonium in a phenomenological confinement scheme*, Proceedings of the DAE Symp. on Nucl. Phys. **57:706** (2012).
- [10] ATLAS collaboration, G. Aad *et al.*, *Observation of a new χ_b state in radiative transitions to $\Upsilon(1S)$ and $\Upsilon(2S)$ at ATLAS*, *Phys. Rev. Lett.* **108** (2012) 152001, [arXiv:1112.5154](#).
- [11] D0 collaboration, V. M. Abazov *et al.*, *Observation of a narrow mass state decaying into $\Upsilon(1S) + \gamma$ in $p\bar{p}$ collisions at $\sqrt{s} = 1.96$ TeV*, *Phys. Rev.* **D86** (2012) 031103, [arXiv:1203.6034](#).
- [12] LHCb collaboration, *Observation of $\chi_b(3P)$ state at LHCb in pp collisions at $\sqrt{s} = 7$ TeV*, [LHCb-CONF-2012-020](#).
- [13] LHCb collaboration, R. Aaij *et al.*, *Measurement of the fraction of $\Upsilon(1S)$ originating from $\chi_b(1P)$ decays in pp collisions at $\sqrt{s} = 7$ TeV*, *JHEP* **11** (2012) 31, [arXiv:1209.0282](#).
- [14] A. Mazurov and B. Couturier, *Advanced modular software performance monitoring*, *Journal of Physics: Conference Series* **396** (2012), no. 5 052054.
- [15] M. Gell-Mann, *A Schematic Model of Baryons and Mesons*, *Phys. Lett.* **8** (1964) 214.
- [16] G. Zweig, *An $SU(3)$ model for strong interaction symmetry and its breaking.*, *Developments in the Quark Theory of Hadrons* (1964).
- [17] J. J. Aubert *et al.*, *Experimental Observation of a Heavy Particle J*, *Phys. Rev. Lett.* **33** (1974) 1404.
- [18] R. K. Ellis, W. J. Stirling, and B. R. Webber, *QCD and Collider Physics*, Cambridge monographs on particle physics, nuclear physics, and cosmology, Cambridge Univ. Press, Cambridge, 2003.
- [19] B. Humpert, *Narrow heavy resonance production by gluons*, *Phys. Lett. B* **184** (1986) 105.

- [20] E. Braaten and T. C. Yuan, *Gluon fragmentation into heavy quarkonium*, *Phys. Rev. Lett.* **71** (1993) 1673, [arXiv:hep-ph/9303205](https://arxiv.org/abs/hep-ph/9303205).
- [21] G. T. Bodwin, E. Braaten, and G. P. Lepage, *Rigorous QCD analysis of inclusive annihilation and production of heavy quarkonium*, *Phys. Rev.* **D51** (1995) 1125, [arXiv:hep-ph/9407339](https://arxiv.org/abs/hep-ph/9407339).
- [22] A. Likhoded, A. Luchinsky, and S. Poslavsky, *Production of χ_b -mesons at LHC*, *Phys. Rev.* **D86** (2012) 074027, [arXiv:1203.4893](https://arxiv.org/abs/1203.4893).
- [23] CDF collaboration, A. Abulencia *et al.*, *Measurement of $\sigma_{\chi_{c2}}\mathcal{B}(\chi_{c2} \rightarrow J/\psi\gamma)/\sigma_{\chi_{c1}}\mathcal{B}(\chi_{c1} \rightarrow J/\psi\gamma)$ in $p\bar{p}$ collisions at $\sqrt{s} = 1.96$ -TeV*, *Phys. Rev. Lett.* **98** (2007) 232001, [arXiv:hep-ex/0703028](https://arxiv.org/abs/hep-ex/0703028).
- [24] LHCb collaboration, R. Aaij *et al.*, *Measurement of the relative rate of prompt χ_{c1} , χ_{c2} and χ_{c0} production at $\sqrt{s} = 7$ TeV*, *JHEP* **10** (2013) 115, [arXiv:1307.4285](https://arxiv.org/abs/1307.4285).
- [25] CMS Collaboration, S. Chatrchyan *et al.*, *Measurement of the relative prompt production rate of $\chi(c2)$ and $\chi(c1)$ in pp collisions at $\sqrt{s} = 7$ TeV*, *Eur. Phys. J.* **C72** (2012) 2251, [arXiv:1210.0875](https://arxiv.org/abs/1210.0875).
- [26] LHCb collaboration, A. A. Alves Jr. *et al.*, *The LHCb detector at the LHC*, *JINST* **3** (2008) S08005.
- [27] D. F. Kruse and K. Kruszelecki, *Modular software performance monitoring*, *J. Phys. : Conf. Ser.* **331** (2011) .
- [28] G. Barrand *et al.*, *Gaudi - a software architecture and framework for building hep data processing applications*, *Comput. Phys. Commun.* **140** (2001) 45.
- [29] *Perfmon2: a standard performance monitoring interface for Linux*, <http://perfmon2.sourceforge.net/perfmon2-20080124.pdf>.
- [30] *Intel[®] VTune[™] Amplifier XE*, <http://software.intel.com/en-us/articles/intel-vtune-amplifier-xe/>.

- [31] *Gperftools performance analysis tools*, <http://code.google.com/p/gperftools/>.
- [32] *Valgrind framework for building dynamic analysis tools*, <http://valgrind.com>.
- [33] HERA-B collaboration, I. Abt *et al.*, *Production of the Charmonium States χ_{c1} and χ_{c2} in Proton Nucleus Interactions at $\sqrt{s} = 41.6\text{-GeV}$* , *Phys. Rev.* **D79** (2009) 012001, [arXiv:0807.2167](https://arxiv.org/abs/0807.2167).
- [34] LHCb collaboration, R. Aaij *et al.*, *Measurement of the cross-section ratio $\sigma(\chi_{c2})/\sigma(\chi_{c1})$ for prompt χ_c production at $\sqrt{s} = 7\text{ TeV}$* , *Phys. Lett.* **B714** (2012) 215, [arXiv:1202.1080](https://arxiv.org/abs/1202.1080).
- [35] CDF collaboration, T. Affolder *et al.*, *Production of $\Upsilon(1S)$ mesons from χ_b decays in $p\bar{p}$ collisions at $\sqrt{s} = 1.8\text{ TeV}$* , *Phys. Rev. Lett.* **84** (2000) 2094, [arXiv:hep-ex/9910025](https://arxiv.org/abs/hep-ex/9910025).
- [36] I. Belyaev *et al.*, *Handling of the generation of primary events in GAUSS, the LHCb simulation framework*, *Nuclear Science Symposium Conference Record (NSS/MIC) IEEE* (2010) 1155.
- [37] Geant4 collaboration, J. Allison *et al.*, *Geant4 developments and applications*, *IEEE Trans. Nucl. Sci.* **53** (2006) 270.
- [38] M. Needham, *Clone track identification using the kullback-liebler distance*, Tech. Rep. CERN-LHCb-2008-002, CERN, Geneva, Jan, 2008.
- [39] A. Powell, *Particle identification at LHCb*, 35th International Conference on High Energy Physics, Paris, France (22-28 Jul 2010) pp.020.
- [40] W. Verkerke and D. Kirkby, *The RooFit toolkit for data modeling*, ArXiv Physics e-prints (2003) [arXiv:physics/0306116](https://arxiv.org/abs/physics/0306116).
- [41] LHCb collaboration, R. Aaij *et al.*, *Production of J/ψ and Υ mesons in pp collisions at $\sqrt{s} = 8\text{ TeV}$* , *JHEP* **1306** (2013) 064, [arXiv:1304.6977](https://arxiv.org/abs/1304.6977).
- [42] G. M. Phillips, *Interpolation and Approximation by Polynomials*, Springer, 2003.

- [43] L. Motyka and K. Zalewski, *Mass spectra and leptonic decay widths of heavy quarkonia*, *Eur. Phys. J.* **C4** (1998) 107, [arXiv:hep-ph/9709254](#).
- [44] CMS Collaboration, *Measurement of the χ_{b2}/χ_{b1} production cross section ratio in pp collisions at $\sqrt{s}=8$ TeV*, Tech. Rep. CMS-PAS-BPH-13-005, CERN, Geneva, 2013.
- [45] Particle Data Group, J. Beringer *et al.*, *Review of particle physics*, *Phys. Rev.* **D86** (2012) 010001.
- [46] M. Pivk and F. R. Le Diberder, *sPlot: a statistical tool to unfold data distributions*, *Nucl. Instrum. Meth.* **A555** (2005) 356, [arXiv:physics/0402083](#).
- [47] LHCb collaboration, R. Aaij *et al.*, *Measurement of Upsilon production in pp collisions at $\sqrt{s}=2.76$ TeV*, [arXiv:1402.2539](#).
- [48] *Jackknife (statistics)*, [http://en.wikipedia.org/wiki/Jackknife_\(statistics\)](http://en.wikipedia.org/wiki/Jackknife_(statistics)).
- [49] W. Hulsbergen, *Private communication*, .

Acknowledgements

It would not have been possible to write this doctoral thesis without the help and support of the kind people around me. I had a chance to work at the large LHCb collaboration where one works together with many people, and, unfortunately, this means that the number of people that in some way have contributed to this work is too large to all personally thank here.

I would like to express my special appreciation and thanks to Vanya Belyaev, who was, as usual, full of nice ideas and useful comments. Your advice on research as well as on the life itself have been priceless and this was my fault, that sometimes I didn't follow them.

I would like to thank to my PhD advisors, Concezio Bozzi and Hans Dijkstra, the discussions and suggestions on multiple subjects concerning the analysis were always useful. Thank you for guidance, understanding and patience. Many thanks to smart people from ITEP LHCb group. Viktor Egorychev, Daria Savrina, Ivan Polyakov, your comments and advice help a lot. Many thanks to the authors of the previous χ_b study. Konstantin Belous and Mikhail Shapkin, your work helps a lot. Patric Robbe, thank you for the help with Monte-Carlo simulation.

Concerning the work on the profiler I would like to thank Ben Couturier and Marco Cattaneo for helping me with preparing the publication and given me an opportunity to present my work at CHEP conference in New-York. And Marco Clemencic, I could thank you for your help on software, in particular concerning GAUDI.

Concerning the time at LHCb Online Team I would like to thank to all team. Niko Neufeld, thank you for being my promoter and for taking risk of hiring me — it was the first step in my past 7 years career at CERN.

Thank you to my colleagues from University of Ferrara. Stefania Vecchi and Antonio Falavella, it was a pleasure to work with you.

There are still too many people to mention. All the other people within LHCb, who helped, worked, drank coffee, ran Relay Race with me: thank you for the good atmosphere.

I am really thankful to my parents, Evgenij and Evgenija Mazurovy, for all their love and support during this long path.

Finally, and most importantly, I would like to thank my wife Vika and daughter Ira for their love and constant support, for all the late nights and early mornings, and for keeping me sane over the past few months.